Studies in Magnon Spintronics



Calvin James Tock

St. Hugh's College

A thesis presented for the degree of Doctor of Philosophy

Department of Physics

University of Oxford

UK

Michaelmas term 2017

Studies in Magnon Spintronics

Submitted for the degree of Doctor of Philosophy

Calvin James Tock, St. Hugh's College, University of Oxford

Michaelmas term 2017

Abstract

This thesis is a thesis of two halves. The first investigates the Spintronic idea of generating charge-decoupled spin currents in metallic systems, whereas the second contains discussions on the topic of Magnon Computing.

Chapters 2 and 3 investigate the relevance of the 'old knowledge' of Magnetic Resonance to the modern-day research field of Spintronics. A model based on the Overhauser Effect is presented that explains microscopically how a pure spin current can be generated in a metallic bilayer system, and an experiment is proposed to explore this model, which is dubbed the 'Overhauser Spin Battery'.

Chapter 3 contains details of all three aspects of the Spin Battery experimental process - that of sample fabrication, sample experimentation, and a presentation of the results. The results support the model presented in Chapter 2, and suggest that the Overhauser Spin Battery can indeed be used to generate pure spin currents.

Chapter 4 looks at the problem of how information is encoded into magnonic streams. A simple device for converting between amplitude modulated (AM) and phase modulated (PM) signals is demonstrated. Potential novel applications of this device are also considered.

Chapter 5 investigates methods of separating magnonic signals of differing frequencies that have been transmitted down a single waveguide simultaneously, which is known as multiplexing. It was determined that heterodyning is a viable method for extracting signals from a multiplexed data stream, and that it is applicable to both AM and PM signals. Quadrature phase-shift keying is shown to be a valid method for doubling the information transmitted down a magnonic waveguide, and a discussion is presented about how the principles of phase-shift keying could be applied to wider questions in Magnon Computing.

Chapter 6 summarises the key ideas and results of the thesis, and considers some further experiments that may be of interest.

Acknowledgments

First and foremost, I would wholeheartedly like to thank my supervisor, Prof. John Gregg, for taking me under his wing and allowing me to play around in his laboratory for the last four years. His polymathic approach to Physics has been as illuminating as it has been inspirational, and his unconventional insights and stories have made the entire DPhil. process all the more enjoyable.

I would like to thank Prof. James Binney and Prof. Dr. Burkard Hillebrands for provocative and fruitful discussions about the work, and Prof. Arzhang Ardavan and Dr. Junjie Liu for their assistance using the commercial spectrometer. I would also like to thank Mathew Newport for both training and supervising me in the use of the machines in the research workshop.

I would like to express my gratitude to my lab partners and colleagues - Dr. Nelson Fung, Richard Morris, Alistair Inglis, Aaron Briggs, and Monika Mycroft - who have provided me with good company in room 174 over the years, and have always been there, ready to hold a soldering iron for me when called upon.

I would not be writing this thesis today were it not for my parents and my brother. For encouraging my curiosity from an early age, and for the love, support, and guidance they have given me over my whole life, to them I am truly grateful.

Last but by no means least, I thank my wife, Rachel. She has been with me right from the start, and has had the patience to see me through to the end. For her companionship on this journey, and for having unwavering confidence and belief in my abilities, even when I did not, I can never thank her enough.

Calvin Tock, December 2017

Contents

Abstract i

Acknowledgments ii

Contents iii

List of Figures vi

List of Tables ix

List of Symbols and Abbreviations x

1 Introduction 1
- 1.1 Spintronics and Magnonics: the 'big picture' . . . 1
  - 1.1.1 The problem . . . 1
  - 1.1.2 A solution or two . . . 1
- 1.2 Spin, charge, and magnon currents, and everything in between . . . 2
  - 1.2.1 Spin currents . . . 3
  - 1.2.2 Magnon currents . . . 3
  - 1.2.3 Magnon modes . . . 6
  - 1.2.4 Interconversion techniques: The magnonician's toolbox . . . 8
- 1.3 Magnon Computing . . . 11
  - 1.3.1 Some current devices... . . . 12
  - 1.3.2 Motivation for work into AM/PM and multiplexing . . . 17

2 The Spin Battery: Theory 19
- 2.1 Overhauser introduction: something old, something new... . . . 19
- 2.2 Pre-requisite Theory . . . 20
  - 2.2.1 Magnetic Resonance . . . 20
  - 2.2.2 Spin-flip relaxation channels . . . 21
- 2.3 Overhauser theory . . . 24
  - 2.3.1 The energy level diagram . . . 24
  - 2.3.2 The Overhauser effect in metals . . . 26
- 2.4 The Spin Battery Model . . . 29
  - 2.4.1 The general principle . . . 29
  - 2.4.2 Electrochemical potential splitting to number densities . . . 30
  - 2.4.3 The Diffusion-like equations . . . 32
  - 2.4.4 The Spin Battery Experiment . . . 32
  - 2.4.5 Solving the equations . . . 33

2.4.6 The inverse spin Hall voltage generated from the spin current 35
2.4.7 Numerical simulations 36

3 The Spin Battery: Experiments 41
3.1 General laboratory experimental methods 41
3.1.1 Fabrication techniques 41
3.1.2 How-to guide 50
3.1.3 Experimental techniques 53
3.2 Spin Battery Experimental Results 67
3.2.1 Preliminary data 67
3.2.2 YIG/Pt 71
3.2.3 Ag/Pt and Cu/Pt 74
3.2.4 Ni/Pt 75
3.3 Discussion of the results, and conclusions about the Spin Battery . . 79
3.3.1 Why such a small signal? 79
3.3.2 Three models of Ferromagnets and Ferromagnetic resonance . 80
3.3.3 The Spin Battery Model Redux 82
3.3.4 Conclusions 87

4 The AM/PM Converter 88
4.1 Introduction to Amplitude and Phase modulation, and the ζ notation 88
4.2 The AM/PM converter 90
4.3 Experimental results for the AM/PM inter-converters 90
4.3.1 AM/PM signal generation and detection 90
4.3.2 AM/PM conversion in a YIG waveguide 92
4.4 Potential application to other magnon devices 96
4.5 Summary of AM/PM inter-converters 97

5 Magnon Multiplexing 98
5.1 Introduction 98
5.2 General experimental arrangement 99
5.2.1 Signal transmission 100
5.2.2 Signal generation 100
5.2.3 Signal detection and demodulation 101
5.3 Heterodyne downconversion 102
5.3.1 Heterodyning theory 102
5.3.2 Existing signal processing techniques 104
5.3.3 Heterodyning experimental results 106
5.3.4 Bandwidth and Filtering 110
5.3.5 Interferometry method 123
5.3.6 Interferometer Results 127
5.3.7 Troubleshooting/Design considerations 131
5.3.8 Non-linear crosstalk between magnon channels 134
5.4 Quadrature phase-shift keying 135
5.4.1 How it works 136
5.4.2 Experimental QPSK 139
5.4.3 Higher order phase-shift keying 140
5.4.4 Phase-shift keying conclusions 147
5.5 Conclusions on magnon multiplexing 147

6 Conclusions and Outlook **149**
6.1 Overhauser Spin Battery 149
6.2 Magnon Computing 151
6.2.1 AM/PM Converters 151
6.2.2 Multiplexing 152
6.2.3 General outlook 155

Bibliography **158**

List of Figures

1.1 Diagram showing the difference between charge, 'impure' spin, and 'pure' spin currents. . . . 4
1.2 Illustration of a magnon in a 1D ferromagnetic chain. . . . 7
1.3 Charge, Spin, and Magnon current interconversion methods. . . . 9
1.4 Diagram of the Spin Hall Effect. . . . 10
1.5 Schematic of the magnon majority gate. . . . 13
1.6 Schematic of the all-magnon transistor. . . . 16
1.7 Schematic of a magnon amplifier. . . . 17
1.8 Schematic of the all-magnon XOR gate. . . . 18

2.1 The Overhauser effect understood via energy level diagrams for an electron-nucleus system. . . . 25
2.2 Bandstructure of a simple paramagnetic metal in a magnetic field under microwave excitation. . . . 28
2.3 The principle behind the Overhauser Spin Battery. . . . 30
2.4 The Spin Battery experiment. . . . 33
2.5 The behaviour of the spin accumulation $\rho^* \Delta\bar{\mu}_{\uparrow\downarrow}$ in the Spin Battery device as predicted by the spin battery model. . . . 34
2.6 Diagram of the slice model for calculating the inverse spin Hall voltage in an irradiated metal sample. . . . 36
2.7 Plot of the dependence of the Spin Battery's inverse spin Hall voltage on the thickness of the silver with respect to the silver's spin diffusion length ($l_{\mathrm{Ag}}/\lambda_{\mathrm{Ag}}$) for various values of λ_{Ag}. . . . 40

3.1 The 'mushroom' substrate manipulator. . . . 44
3.2 A 'mushroom holder', a single rung of the substrate storage rack, and the substrate table. . . . 45
3.3 The vacuum chamber, with annotations showing the location of some of the key components. . . . 45
3.4 The storage rack, and the gearbox used to raise and lower it. . . . 46
3.5 A schematic diagram of the ESR Setup, showing the arrangement of the large electromagnets, the modulation coils, the Hall probe, the cryostat, and the ESR probe. . . . 57
3.6 The workings of a rhumbatron cavity resonator. . . . 60
3.7 Cross-sectional diagram of the cylindrical rhumbatron cavity used in the experiments, with dimensions in mm. . . . 61
3.8 Schematic of the microwave stripline experiment, with measurements in mm. . . . 62
3.9 Schematic of the ESR probe in a third angle orthographic projection. 63

3.10 Diagram of the rhumbatron sample holder. 64
3.11 Schematic diagram showing how a lock-in amplifier processes an ESR signal. 66
3.12 ESR traces of several thin film samples made in the Brucker EMX commercial spectrometer, presented to show the relative signal sizes. . 69
3.13 ESR traces of the AgPt film and Empty tube in the commercial spectrometer. 69
3.14 Rhumbatron ESR trace of DPPH at 10.524 GHz. 71
3.15 FMR signal of the YIG/Pt bilayer, measured via the changes in the throughput of the microwave stripline. 73
3.16 ISHE signal of the YIG/Pt bilayer, measured via a lock-in amplifier. . 73
3.17 ISHE and ESR traces for the NiPt bilayer, measured in the rhumbatron. 76
3.18 The symmetric and antisymmetric components of the curve fitted to the NiPt ISHE signal. 77
3.19 The Anomalous Hall Effect (AHE) when the applied field is just below $\boldsymbol{B}_{\text{FMR}}$. 78
3.20 Hysteresis loop in the 'ISHE' signal of the NiPt film around zero field. 79
3.21 Idealised bandstructures of a) a Pauli paramagnet, b) a Pauli paramagnet in an applied field, and c) a ferromagnet. 81
3.22 Diagram of the two-band model of a microwave irradiated ferromagnet, incorporating the quantum 'fuzziness' caused by co-operative superposition effects. 85

4.1 Diagrams of the newly proposed AM and PM inter-converters, with explanatory waveforms. 91
4.2 AM and PM microwave encoder circuit. 92
4.3 Diagram of the YIG waveguide used for the AM/PM interconversion experiments. 93
4.4 AM input signals, as measured with a heterodyne demodulator, with probe phases shifted by 180° between traces. 94
4.5 Demonstration of the AM to PM converter. 94
4.6 PM input signals, as measured with a heterodyne demodulator, with probe phases shifted by 180° between traces. 95
4.7 Demonstration of the PM to AM converter. 95
4.8 All-magnon AM and PM amplifiers. 96

5.1 Schematic of the basic multiplexing experiment. 100
5.2 Low-pass filter transmission properties, measured on a network analyser. 105
5.3 Input signal pulse shapes for the heterodyning experiments as measured by a crystal detector/diode. 107
5.4 Heterodyne demodulation of AM electrical signals at 3.15 GHz and 3.25 GHz. 108
5.5 Heterodyne demodulation of AM magnon signals at 3.15 GHz and 3.25 GHz. 109
5.6 Heterodyne demodulation of PM electrical signals at 3.15 GHz and 3.25 GHz. 111
5.7 Heterodyne demodulation of PM magnon signals at 3.15 GHz and 3.25 GHz. 111

5.8 Transmission spectrum through the YIG waveguide in its backward-volume mode. 112
5.9 2D plot of heterodyne demodulated AM magnon signals, 100 MHz apart, at 3.15 GHz and 3.25 GHz. 114
5.10 2D plot of heterodyne demodulated PM magnon signals, 100 MHz apart, at 3.15 GHz and 3.25 GHz. 114
5.11 Heterodyne demodulation of AM pulses at 3.15 GHz, where a second signal exists at a frequency that is 10, 25, and 100 MHz above. 116
5.12 Heterodyne demodulation of PM pulses at 3.15 GHz, where a second signal exists at a frequency that is 10, 25, 50, and 100 MHz above. . . 116
5.13 2D plot of heterodyne demodulated AM magnon signals, 100 MHz apart, at 3.15 GHz and 3.25 GHz. 118
5.14 2D plot of heterodyne demodulated AM magnon signals, 10 MHz apart, at 3.15 GHz and 3.16 GHz. 118
5.15 3D plot of heterodyne demodulated AM magnon signals, 100 MHz apart, at 3.15 GHz and 3.25 GHz. 119
5.16 3D plot of heterodyne demodulated AM magnon signals, 10 MHz apart, at 3.15 GHz and 3.16 GHz. 119
5.17 Effects of a 1 MHz low pass filter. 120
5.18 Diagrams of the Interferometer demodulator. 124
5.19 Interferometer demodulation of AM electrical signals at 3.15 GHz and 3.25 GHz. 128
5.20 Interferometer demodulation of AM magnonic signals at 3.15 GHz and 3.25 GHz (Blue and Red respectively), and the unprocessed magnonic signal (yellow). 128
5.21 Transmission spectrum through a section of the Interferometer circuit consisting of three splitters and some cables. 129
5.22 Interferometer demodulation of purely electrical AM pulses at 3.15 GHz, where a second signal exists at a frequency that is 10, 25, 50, 100, and 200 MHz above. 130
5.23 Demonstration of non-linearity in a power amplifier. 132
5.24 Definitions of angles used in the quadrature phase-shift keying discussion. 137
5.25 Constellation plot of the four QPSK states. 138
5.26 Experimental results of the magnon QPSK experiment. 141
5.27 Constellation plots (in the complex ζ plane) for three interfering waves. 144
5.28 Further constellation plots for three interfering waves. 145

List of Tables

1.1 Truth table for the three terminal majority gate. 13

3.1 Details of the resonances observed in Figure 3.12. 70

4.1 Table of input and output encoding formats of existing and author-proposed magnonic devices. 96

5.1 Crosstalk ratios for two AM or PM encoded signals of a given frequency separation. 117

5.2 Theoretical maximum bit-rates of the magnon waveguide for heterodyne demodulated multiplexed signals. 122

5.3 Table of DC outputs expected from a QPSK measurement for a variety of probe phases (θ). The appropriate equation is: $V = \cos((2n+1) \times 45° - \theta)$ 139

List of Symbols and Abbreviations

A list of the symbols used in this thesis is provided here. References to sections of particular relevance (such as where a symbol has been explicitly defined, or heavily used) are also, in some cases, included.

Symbol	Definition	Reference
$\boldsymbol{J_s}$,$\boldsymbol{J_c}$	Current density (Spin or charge)	§1.1,§2.4.4
$\boldsymbol{E}$	Electric field	
$\boldsymbol{B}$	Magnetic field	
$\boldsymbol{M}$	Magnetization	
$\boldsymbol{\mu}$,$\boldsymbol{\mu_n}$,$\boldsymbol{\mu_e}$	Magnetic moment (general, nuclear, and electronic)	§2.2.2
γ	Gyromagnetic ratio	§2.2.1
g	g-factor	§2.2.1
μ_{B}	Bohr magneton	
$\boldsymbol{I}$,$\boldsymbol{J}$	Angular momentum (nuclear and electronic)	§2.2.2
I_z,J_z	z component of angular momentum	§2.2.2
I^+,I^-,J^+,J^-	Raising and lowering operators	§2.2.2
$\bar{\mu}$	Electrochemical potential	§2.4.2
$\Delta\bar{\mu}_{\uparrow\downarrow}$	Electrochemical potential difference (between up and down spin channels)	§2.4.2
$g(E_\uparrow)$,$g(E_\downarrow)$	Electron density of states for specific spin channels (up or down)	Figure 2.2
ρ^*	Effective Density of states	§2.4.2
D	Diffusion constant	§2.4.2
$\tau_{\uparrow\downarrow}$	Spin-flip relaxation time	§2.4.3
R	Electron excitation rate	§2.4.3
λ	Spin-flip relaxation length	§2.4.5
$-_{\mathrm{H}}$,$-_{\mathrm{R}}$	Subscripts for 'Host' or 'Relaxer' material	§2.4.5
δ	Microwave skin depth	§2.4.6
θ_{ISHE}	Inverse spin Hall angle	§2.4.6
ω_{Probe}	Angular frequency of the 'Local Oscillator' input to an RF multiplier	§3.1.3,§5.3.1
τ_{f}	RC filter time constant	3.1.3
ζ	Relative phase/amplitude of a signal w.r.t. a reference source	§4.1
ξ^+,ξ^-	Binary-1 and binary-0 states encoded in phase modulated signal	Figure 5.24

Abbreviation	Meaning
FMR	Ferromagnetic Resonance
ESR	Electron Spin Resonance
NMR	Nuclear Magnetic Resonance
ISHE	Inverse Spin Hall Effect
FVMSW	Forward Volume Magnetostatic Spin Wave
BVMSW	Backward Volume Magnetostatic Spin Wave
MSSW	Magnetostatic Surface Spin Wave
YIG	Yttrium Iron Garnet
GGG	Gadolinium Gallium Garnet
DPPH	2,2-diphenyl-1-picrylhydrazyl
PM	Phase modulated/modulation
AM	Amplitude modulated/modulation

In loving memory of
my Father
from whom I am still learning.

Chapter 1

Introduction

1.1 Spintronics and Magnonics: the 'big picture'

1.1.1 The problem

Moore's Law, the law that states that the number of transistors in integrated circuits roughly doubles every two years, is coming to an end [1]. Computer processor clock speeds have been frozen since 2004 in an attempt to control the increasing heat-death issues caused by progressive miniaturization. Improvements in chip technology can continue for a few more years by reducing the size of individual components; however, if conventional silicon devices are made much smaller than the present (at time of writing) size of 10 nm, then components may become susceptible to quantum tunnelling, and cease to work at all [2]. This ticking countdown to conventional computational stagnation provides strong motivation to find an alternative computing paradigm that can replace or augment conventional charge-based devices.

1.1.2 A solution or two

Charge is the current currency of computing. Electrons, the most commonly used carrier of this charge, however, also carry another quantum, that of spin angular momentum. Devices that function via the transport and manipulation of 'spin' have been in development since the 1990's [3–5], and fall under the banner of 'Spintronics'.

Spintronics has proved very useful in modern data storage technology, with a prime example being its use within hard drive magnetic read heads. One of the alluring promises of Spintronics are devices that are able to store and process data within individual chips rather than ferrying information between data processing and data storage elements. Computers built from these types of components would be able to, for example, instantly awaken from sleep mode, as the processor could just carry on from its last state [6].

Electron spins also have an associated magnetic moment, which means that electrons that are near to each other can interact through magnetic interactions. Electrons in a magnetically ordered material are able to interact collectively so as to support magnetic excitations known as 'spin waves', in which spin angular momentum is able to flow through the system. These 'spin waves' can be quantized into 'magnons', the study of which is known as 'Magnon Spintronics' or 'Magnonics'.

Magnons are able to propagate in both electrically conductive and insulating materials, and are an exciting potential solution to the Moore's law problem as computers based around the flow of magnons do not require moving charge. This means that Ohmic heating will never be an issue for magnonic devices, and that they have therefore already beaten the key problem facing conventional semiconductor devices. The other important feature of magnon computing is that it is a wave-based paradigm. The power and significance of this will be discussed in later sections.

1.2 Spin, charge, and magnon currents, and everything in between

Conventional electronic devices operate using charge currents, which are generally conveyed by electrons. Technology based on Magnonics or Spintronics will rely on the flows of magnons or spins to operate. In this section, some of the properties of these magnon and spin currents are discussed, as well as some of the difficulties with converting between them.

1.2.1 Spin currents

Electrons are spin-$\frac{1}{2}$ particles and can therefore be considered to be in either an 'up' state or a 'down' state with respect to any given measurement axis. Conventional charge currents usually have equal quantities of up and down electrons within them, and therefore no net flow of spin. If a current of electrons is produced in which one spin state is favoured over the other, then that current is spin-polarized. An extreme case of this is a fully polarized beam in which all of the spins are in their 'up' state, for example. This polarized electron stream carries both a net spin and a net charge. This type of current is called an 'impure' spin current.

If two counter-propagating polarized electron streams in which the polarizations of the two streams are opposite are now considered, there is an equal number of up spins going one way as there are down spins going the other. In this case, there is a large flow of angular momentum but no net flow of charge. This is called a 'pure' spin current, as the flow of spin has been fully decoupled from the flow of charge. This is an important and desirable feature, as it again provides a potential way of avoiding the overheating problem of conventional devices.

The difference between conventional, impure spin, and pure spin currents is depicted in Figure 1.1.

1.2.2 Magnon currents

Magnons are the quasi-particles associated with quantized spin waves, which describe small, propagating excitations/deviations of bound electrons' spins from their fully ordered magnetic ground state within a ferromagnetic crystal lattice [7].

The magnons commonly encountered in condensed matter physics (such as in inelastic neutron scattering [8]) tend to be high energy magnons, mediated by the exchange interaction, whereas the magnons used in Magnonics are driven by the physics of long-range dipolar interactions, which leads to longer wavelengths, and much lower energies [9]. These are often called 'magnetostatic' spin waves.

To visualize what a magnon looks like, the derivation of the magnon in a Heisen-

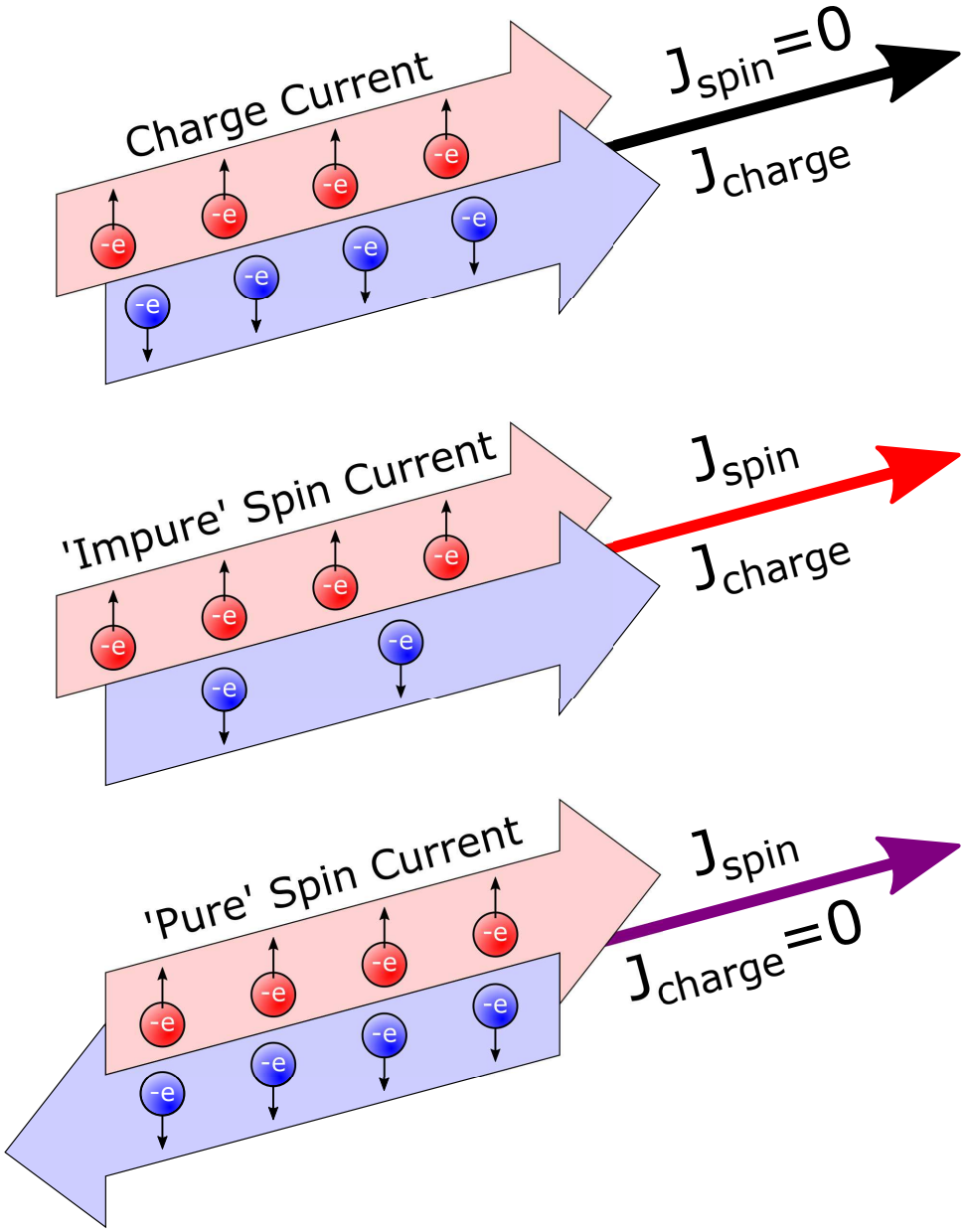


Figure 1.1: Diagram showing the difference between charge, 'impure' spin, and 'pure' spin currents. In the charge current, equal populations of up and down electrons flow in the same direction. This current has a net flow of electrons, and thus charge, but no net flow of spin. If a charge current is polarized, and more of the flowing electrons are of one spin type than the other, then an 'impure' spin current is created, in which both spin and charge are transported by the electrons. If two 'impure' currents of the same magnitude flow in opposing directions, then there is no net flow of charge, but there is a flow of spin. As spin and charge currents have been fully decoupled, this is known as a 'pure' spin current.

berg ferromagnetic chain can be considered [10]. The general principle is to take a 1D ferromagnetic chain and flip one of the spins, for example on site $\boldsymbol{R}$. This state ($|\boldsymbol{R}\rangle$) is not an eigenstate of the Hamiltonian of the system, but if the correct linear combination of states in which a single spin has been flipped is made, it is possible to construct an eigenstate. The correct superposition takes the form

$$|\boldsymbol{k}\rangle = \frac{1}{\sqrt{N}} \sum_{\boldsymbol{R}} \mathrm{e}^{i\boldsymbol{k}\cdot\boldsymbol{R}} |\boldsymbol{R}\rangle \tag{1.1}$$

where N is the number of spins in the chain. The probability of finding the single flipped spin on any given site is given by $|\langle \boldsymbol{k}|\boldsymbol{R}\rangle|^2 = \frac{1}{N}$, which, in effect, means that the spin-flip has been equally distributed across all of the spins. Viewed classically, this can be thought of as each of the spins deviating from perfect alignment by a small angle. Each of the spins will then precess with a fixed phase relationship to its neighbour that is defined by $\boldsymbol{k}$. A diagram of this interpretation of the magnon is shown in Figure 1.2.

Additional insight into the quantum picture of the magnon can be derived by considering the 'particle in a box' model of covalent bonding between two hydrogen atoms [11]. In this case, the energy of the electron localised to one of the hydrogen atoms is

$$E = \frac{\hbar^2 \pi^2}{2 m_e L^2}$$

where L is the size of the box. When the electron is allowed to delocalise over the positions of both of the atoms, the size of the box increases to $2L$, and the energy of the electron decreases to

$$E = \frac{\hbar^2 \pi^2}{2m(2L)^2}.$$

By viewing the magnon as an itinerant spin-flip, parallels can be drawn between the magnon and the hydrogen molecule that helps clarify the nature of the energy cost of creating a magnon. By flipping a single spin on a specific site in a ferromagnetic chain, the 'cost' is that of the very large exchange quantum. By allowing that spin to delocalise to anywhere on the chain (via a series of mutual spin-flips with its

neighbour), the size of the 'box' has now increased from a single site to the entire chain, and the energy of the system has, much like the electron in the hydrogen molecule, decreased. Understanding the justification for the energy cost of creating a magnon will be useful for the discussion in section 3.3.2.

1.2.3 Magnon modes

The dispersion relation (the relationship between energy and momentum of a spin wave) for low-energy magnon modes confined within a thin film sample is highly dependent on the geometry of the experiment. There are three vectors to consider: the direction of magnon propagation, $\boldsymbol{k}$, the direction of the magnetization of the film, $\boldsymbol{M}$, and the vector perpendicular to the film's plane, $\boldsymbol{n}$. $\boldsymbol{k}$ always lies in the plane of the film, so is perpendicular to $\boldsymbol{n}$. The magnon dynamics are therefore dependent on the relative direction of the magnetization vector.

There are three general magnon modes, characterized by the following arrangements. Forward Volume Magnetostatic Spin Waves (FVMSW) occur when the magnetization is parallel to $\boldsymbol{n}$. Backward Volume Magnetostatic Spin Waves (BVMSW) occur when $\boldsymbol{M}$ is parallel to $\boldsymbol{k}$. Magnetostatic Surface Spin Waves (MSSW) occur when the magnetization is perpendicular to both $\boldsymbol{n}$ and $\boldsymbol{k}$. Details of the different dispersion relations for each of these modes can be found in reference [12].

All of the experiments in this thesis used one-dimensional magnonic waveguides, and were performed using magnons in their backward volume mode. Some of the magnonic devices discussed in this thesis, however, have two-dimensional geometries, meaning that backward volume waves may be unsuitable (due to the highly anisotropic nature of the magnon dispersion relation), and forward volume waves are needed instead. In the forward volume mode, magnons can propagate in any direction within the film, including around corners (such is in Figure 4.1), which can be useful for certain magnonic circuit elements.

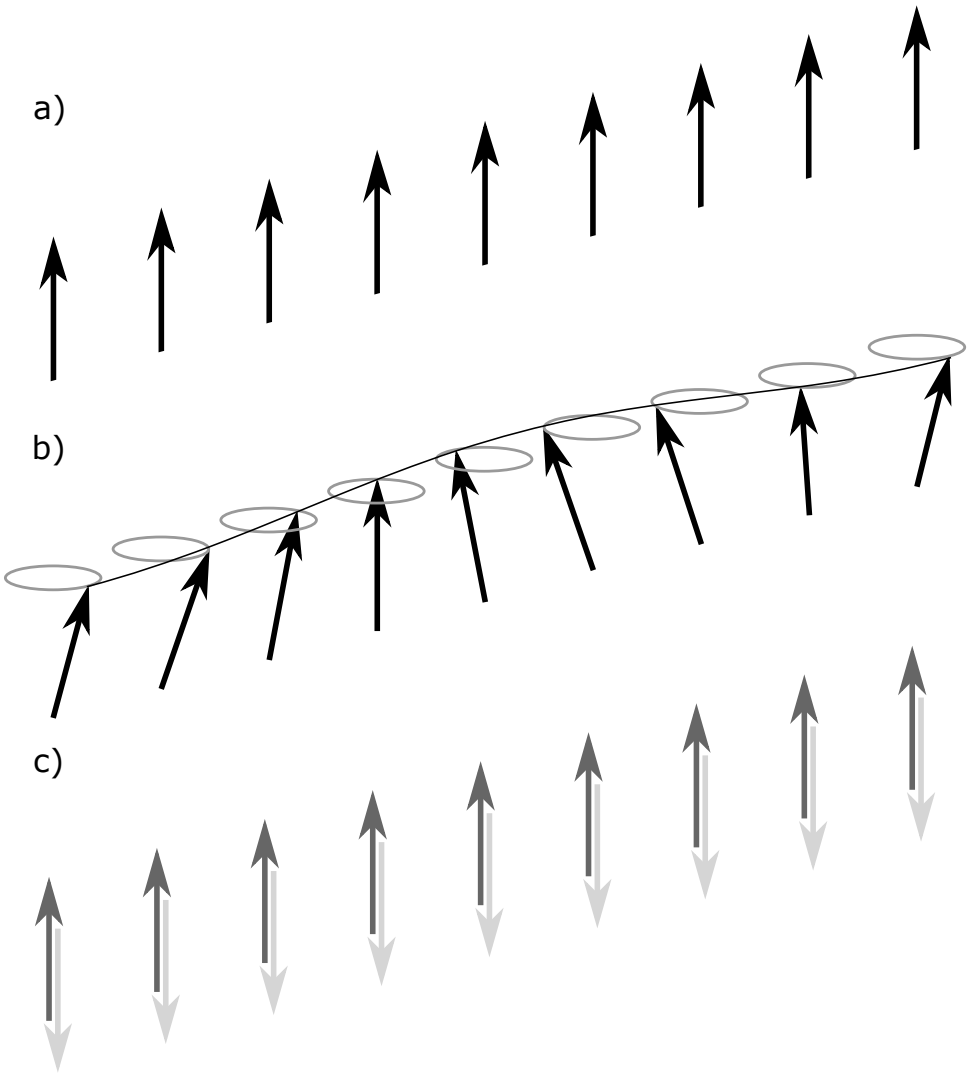


Figure 1.2: Illustration of a magnon in a 1D ferromagnetic chain. a) A 1D ferromagnet in its ground state. All of the constituent spins are aligned. b) The semi-classical depiction of a 1D chain ferromagnet containing a magnon. Each spin has deviated from its ground state by a small angle. All the spins now precess around the vertical axis, and have a fixed phase relation to their neighbours. c) A quantum illustration of the magnon. A single spin is flipped in the chain, which leads to the spins entering a superposition state in which the single spin-flip has a small probability of being detected on any given site. This means that each spin has a non-zero probability of being found in its 'down' state, though is more likely to be found in its 'up' state. The relative probabilities are shown here by fading each of the states by an appropriate amount. This depiction is not of great use here, as the phase information is not visible; however, the 'fading' idea will be helpful when it is revisited in §3.3.3.

Yttrium Iron Garnet (YIG)

Yttrium Iron Garnet, or YIG ($Y_3Fe_5O_{12}$), is a synthetic garnet crystal and has the lowest magnon damping factor of any known material [12]. This low damping leads to magnon decay lengths on the order of 10 mm when grown in films with thicknesses of around 1 µm [13]. This makes YIG an ideal material with which to perform magnonic experiments, and is why it is used as the primary magnonic material in this thesis.

Thin films of YIG are difficult to manufacture, and, until recently, equally difficult to purchase. This is a factor that must be considered when designing experiments, as it may not be possible to create unconventionally shaped waveguides due to lack of access to the necessary materials. In §4.3.2, a linear waveguide was used for this reason.

Other magnonic materials that are currently available (such as $Ni_{81}Fe_{19}$ (Permalloy) or $Co_{40}Fe_{40}B_{20}$), have much shorter magnon decay lengths, but also have much shorter magnon wavelengths [13]. This means that, although they are more challenging to work with for laboratory-based experiments, these materials may be more useful in the future when attempting to reduce the size of a magnonic circuit. This is especially apparent when considering the magnonic crystal (see §1.3.1), which needs physical perturbations on the same scale as the magnon wavelength to function.

1.2.4 Interconversion techniques: The magnonician's toolbox

Magnon, spin, and conventional charge currents all have their own strengths and weaknesses, and the best computers of the future will use a combination of these newer types of current and the old. For Magnonics and Spintronics to be integrable with conventional electronics, methods of current interconversion are required. Fortunately, several methods have already been developed, and are shown in Figure 1.3. References providing more details on each of these methods can be found in the caption, as only the few techniques relevant to the thesis are discussed here.

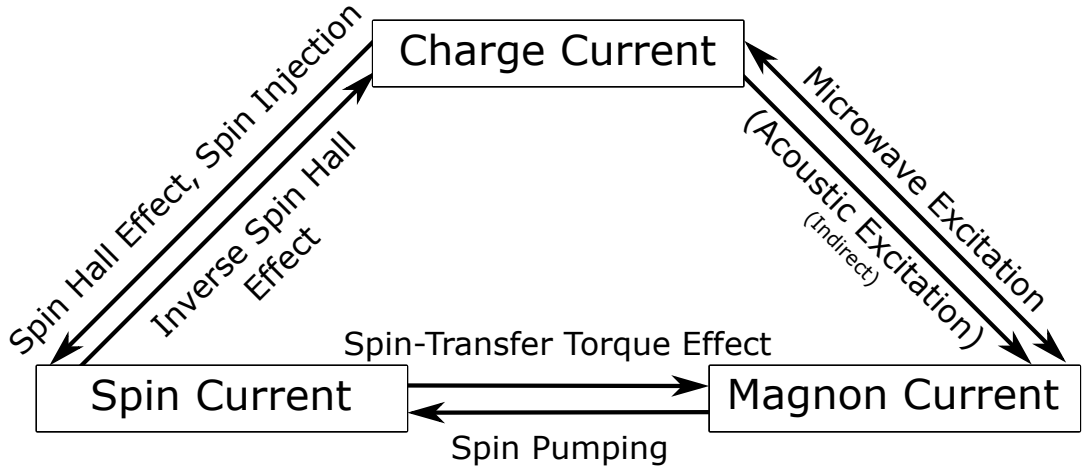


Figure 1.3: Charge, Spin, and Magnon current interconversion methods. The direct and inverse spin Hall effects are discussed in the main text, as is microwave excitation and spin pumping. References pertaining to the other three methods shown in this diagram are provided here: Spin Injection [3], Spin-transfer torque effect [14], and Acoustic excitation [15]. Acoustic excitation is more accurately linked to voltage, however, it is included here as it is still an electrical method for generating magnons.

The direct and inverse spin Hall effects

When a current is passed through certain metals which have large spin-orbit interactions, the spin up and spin down electrons (on average) scatter in different directions [16]. Although the effect can often be small [17], it still results in oppositely aligned spins accumulating on opposite sides of the metal (a spin accumulation) in the direction perpendicular to the current flow. This is known as the (Direct) Spin Hall Effect ((D)SHE). This can be seen in Figure 1.4.

If a pure spin current is passed through the same metal, there is no net charge flow, which leads to the question 'How can the pure spin current be detected?'. The inverse spin Hall effect (ISHE) provides a solution.

The ISHE works, unsurprisingly, as the exact inverse of the SHE. When two counter-propagating beams of electrons polarized with opposite spins pass through a metal with a strong spin-orbit coupling, they both (on average) scatter in the *same* direction. This leads to a charge current, and therefore a voltage build up across the material, which can then in turn be measured [18]. This in conjunction with the SHE, provides a useful technique for converting between spin and conventional currents.

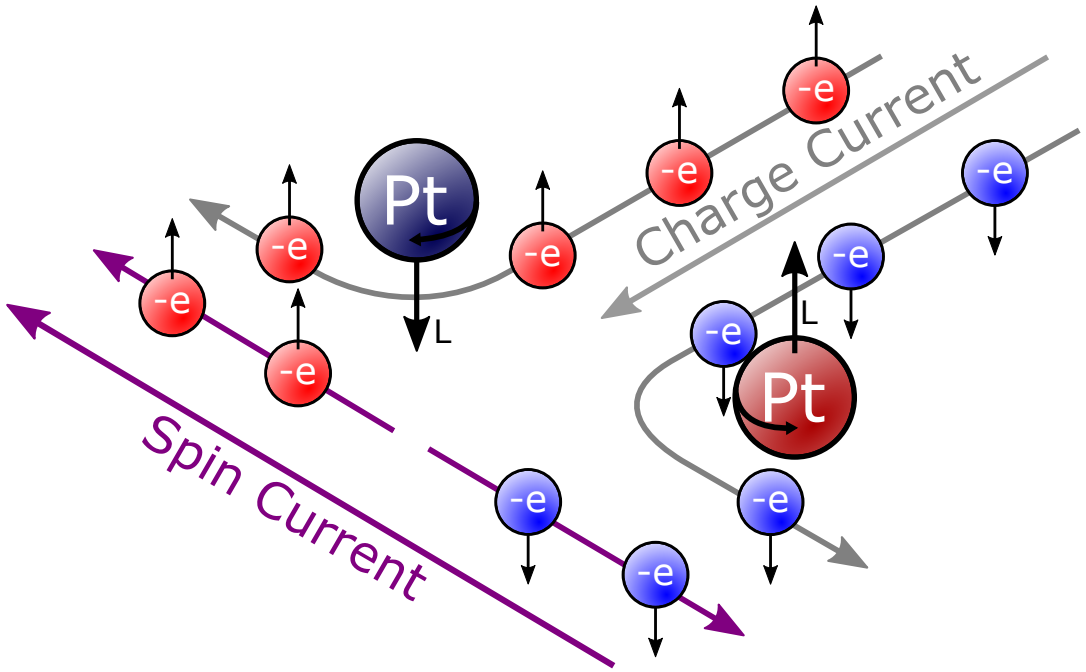


Figure 1.4: Diagram of the Spin Hall Effect. Spins are preferentially scattered in opposite directions by the metal ions, leading to a perpendicular spin current. By reversing the flow of electrons, the inverse spin Hall effect can be observed (in which a spin current scatters into a charge current).

Microwave excitation

Conventional electronics can be integrated with spin waves directly through the use of microwave antennae [19]. By applying microwaves to a microstrip antenna lying across a magnon waveguide, an oscillating magnetic field is set up inside the waveguide (in addition to the already applied bias field). This locally oscillating field causes the magnetization in the vicinity of the antenna to precess, which under the correct conditions (frequency, bias magnetic field strength) can lead to two counter-propagating spin-waves (one in each direction away from the antenna) [20]. Microwave antennae are useful as they can also be used to detect spin waves. When a spin-wave passes the antenna, the precessing magnetization induces a small, detectable microwave current in the antenna.

It is worth noting here that the range of magnonic modes than can be excited by an antenna is dependent on its design. A simple single stripline antenna cannot efficiently excite magnons whose $\boldsymbol{k}$'s correspond to wavelengths that are shorter than the width of the antenna [21].

Spin Pumping and the Spin Battery

Spin pumping is a method by which magnons in a ferromagnet can drive a spin current into an adjacent normal metal. The usual argument for spin pumping goes like this: A precessing magnetization in a ferromagnet applies a torque to the electrons in the non-magnet close to the material interface [22]. Applying this torque reduces the angular momentum of the precessing magnetization of the ferromagnet, and leads to a spin current flowing away from the interface, into the normal metal. An alternative way of viewing this process is to think of a magnon transferring its angular momentum to the electron, or a current of magnons being converted to a spin current, as required.

Both of these explanations invoke the classical vector model of the ferromagnet precessing in a field. The explanations usually characterize the spin pumping effect phenomenologically using spin-mixing conductance. A detailed discussion of these explanations of spin pumping can be found in reference [23].

The first two chapters of this thesis are centred around the development and testing of an alternative quantum mechanical explanation for microwave spin pumping for metal-metal bilayers, based on the concepts of the Overhauser effect. We provide a microscopic account of spin-pumping between ferromagnetic and normal metals, and show that paramagnet-paramagnet bilayers should also be able to act as a Spin Battery and generate a spin-motive force.

1.3 Magnon Computing

Although magnons were theoretically predicted in 1930 [24] and experimentally discovered in 1946 [25], they have largely been ignored as a potential basis for new technologies until fairly recently. Over the past decade, a small but dedicated global community of scientists have been researching Magnonics, and have been working to create and develop novel devices based on the magnon. Magnon Computing is an even younger speciality, with even fewer active researchers. Despite this fact, some

significant and powerful developments have already emerged, starting with the replication of current digital computation algorithms. Magnon computing has great potential, as it promises devices that will dissipate three orders of magnitude less power than silicon-based technology, have clock speeds potentially into the Terahertz, and have nanometre device footprints [26]. The development of these types of devices is a worthy pursuit, however magnon computing is capable of much more.

As a wave-based technology, magnon computers are able to make use of an entirely different toolbox of physical phenomena not presently available to particle-based conventional computers. These include interference, non-linear dynamics, and signal multiplexing, the latter of which is the focus of Chapter 5. Below, some of the interesting devices that have already been developed are discussed, as they provide insight into the potential of magnon computing.

1.3.1 Some current devices...

Majority gate

The majority gate is a prime example of the power of wave-based computing. The three-input device utilizes interference between the three input waves/magnon streams, and produces an output that is in the same digital state as the majority of the inputs. A diagram of one implementation of the device [27] is shown in Figure 1.5. In this case, the binary states of 1 and 0 have been encoded into the phase of the magnons.

The truth table for the majority gate is shown in Table 1.1. An interesting observation is that if the first input is held constant, the other two inputs have the same logical operations as an AND gate or an OR gate, depending on the state of the first input. This in effect means that it is possible to change the logical operation of the component as and when necessary, or, put another way, a single component is able to perform two different logical operations, which is obviously beneficial in terms of spatial efficiency.

As alluded to previously, and discussed in detail later, it should be possible

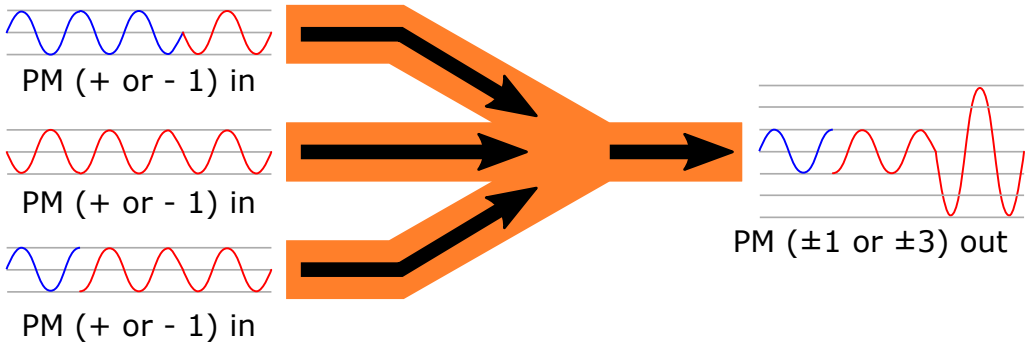


Figure 1.5: Schematic of the magnon majority gate. Three phase-modulated signals enter the majority gate. The blue and red colouring represents a phase shift of 180°, which corresponds to the encoding of the binary-0 and binary-1 states. When the three channels combine, the waves interfere, and then exit the device. The output signal has the same phase (but not necessarily amplitude) as the majority of the input signals.

Inputs			Outputs
A	B	C	Y
0	0	0	0
0	0	1	0
0	1	0	0
0	1	1	1
1	0	0	0
1	0	1	1
1	1	0	1
1	1	1	1

Table 1.1: Truth table for the three terminal majority gate. Holding the first input constant leads to the other two inputs experiencing either an AND or OR gate, depending on the state of the first.

to multiplex magnon streams that are operating at different frequencies down the same waveguide. If this possibility extends to the majority gate, then it should be possible to perform (potentially different) logical operations on several data streams simultaneously, using a single majority gate. The potential of such a device should not be underestimated.

One problem with the majority gate presented here, is that the output is contaminated with amplitude information, e.g. the amplitude of the output is different for a 111 state and a 110 state. This is an important problem that needs to be addressed before the output of this majority gate can be used in other magnon circuit elements, and is discussed briefly in §5.4.3.

Magnonic crystals

The magnonic crystal is a type of artificial crystal. It can be created by applying an artificial lattice to a magnon waveguide in the form of some spatially periodic perturbation (magnetic or physical), in which the period of the structure matches the period of some of the magnons to be used. Propagating magnons of the 'incorrect' frequency will not be overly affected by the crystal, whereas magnons of the appropriate frequency are able to interact with this lattice, perhaps being reflected by it entirely. This is an example of how the transmission properties of the waveguide are altered by the presence of an artificial crystal — rejection bands appear in the transmission spectra in which certain magnons are not able to propagate.

Two types of magnonic crystals exist — static, and dynamic. Static crystals can be created by, for example, scoring periodic lines onto the YIG waveguide itself [13]. This type of crystal does not vary its properties over time, but is still able to interact with the resonant magnons.

Dynamic crystals have the interesting property that they can be turned 'on' and 'off'. This can be achieved in the magnon case by producing a meandering wire above the waveguide, and applying a current [28]. This creates a spatially modulating magnetic field in the waveguide with a periodicity defined by the construction of

the crystal. Turning the current off removes the perturbation, and thus the effects of the crystal can be toggled.

This is interesting as the crystal can be turned on while a signal is propagating along the waveguide. Doing so leads to the magnon pulses being trapped in the crystal, as the crystal is now a region in which the magnons are not permitted to propagate. If the crystal is turned off again at the correct time, the magnon pulse train leaves the crystal from the same direction that it entered, in a 'first in, last out' fashion, leading to a reversal of the order of the pulses. What this dynamic magnon crystal has achieved (in an entirely analogue way) is time-reversal of a data stream, which is normally a computationally expensive task.

Magnonic crystals (both static and dynamic) provide an additional element to the ever increasing magnon computing toolkit. An applied example of the magnonic crystal can be found in the all-magnon transistor.

All-magnon transistor

A necessary element in any magnon-based computer is the magnonic analogue to a conventional transistor. This component should be able to use one magnon current to gate another, with no external electrical involvement. The all-magnon nature of this device is important, as it would enable the construction of complex magnonic circuits without the requirement of lossy conversions back to electrical signals.

One implementation of the magnon transistor has already been developed [29]. This device is depicted in Figure 1.6. The device works by applying a static magnonic crystal to a waveguide, and attaching an additional branch to the waveguide, extending from the middle of the magnon crystal (which is the equivalent to the 'gate' terminal).

Magnons of the 'incorrect' frequency (that can freely pass through the crystal) are initially sent along the waveguide from the 'source' to the 'drain'. When the transistor is activated, magnons of the 'correct' frequency are applied to the gate input. As they are unable to propagate out of the magnonic crystal, the magnon

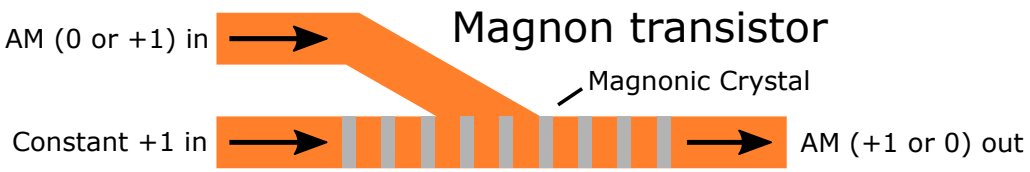


Figure 1.6: Schematic of the all-magnon transistor. A continuous, unmodulated magnon signal that is able to pass through the magnonic crystal is sent along the waveguide. The transistor is switched by introducing a second gating magnon current into the side of the magnonic crystal. These magnons are confined to the crystal, and do not propagate further, but are able to scatter the original magnon stream, reducing the overall output of the device. As the output magnon signal strength is now controlled by the presence or absence of the gating current, the devices can be considered to be a transistor.

density inside the crystal is greatly increased. This leads to an increase in magnon-magnon scattering, including between the signal magnons and the gating magnons. This increased scattering reduces the emitter output of the device, and, to within a threshold level, stops the initial magnon signal. When the gating magnons are switched off, scattering is reduced, and the signal magnons are once again free to flow.

Magnon amplifier

An example of a simple circuit that makes use of the all-magnon transistor is the magnon amplifier [29] shown in Figure 1.7. This device operates by taking a large, continuous magnon stream and splitting it in two. The two branches propagate over a certain distance before recombining, and flowing to the device output. One of the branches is longer than the other by such a distance that the magnons from the two branches destructively interfere at the recombination point.

The other branch contains a magnon transistor, gated by the signal that is to be amplified. When activated, this has the effect of reducing the flow of magnons through that branch. This leads to a reduction in the destructive interference at the device output, and the magnons flowing from the non-transistor branch are now able to exit the amplifier unhindered. As the control signal can be of a lower amplitude than the continuous stream, the output can be considered to be amplified.

In reference [29], it is highlighted that there is a balance to be made between the

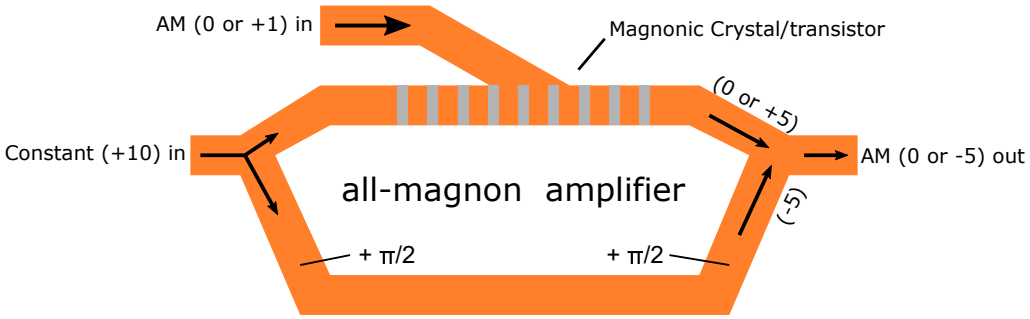


Figure 1.7: Schematic of a magnon amplifier. The device operates in a similar fashion to the magnon transistor, however an additional path has been added to the circuit. This path travels half a wavelength further than the transistor path before the two channels recombine. This leads to destructive interference when the transistor is open, and an output signal when the transistor is closed. As the magnon amplitude required to gate the transistor is less than the magnon signal that can be gated, the output can be greater than the input, and the circuit performs as an amplifier.

relative amplitudes of the control and the power inputs, as the magnon transistor does not operate with 100% efficiency. If the correct balance is struck, then a net gain is obtainable across the device, and the device indeed acts as an amplifier.

XOR gate

A more advanced circuit that replicates a conventional logic operation while using fewer components is the XOR circuit. This takes a similar form to the all-magnon amplifier, however each branch now has a magnon transistor, as shown in Figure 1.8. By using the two transistor inputs as the two logical inputs, and following through the circuit with interference in mind, it can be deduced that the output follows the same truth table as an XOR gate.

1.3.2 Motivation for work into AM/PM and multiplexing

The second part of this thesis investigates two specific challenges that need to be addressed before the full potential of magnon computing can be realised. The first problem is that the method by which data is encoded into any given magnon stream is not always consistent. Sometimes amplitude modulation (AM) is used, as is the case for the magnon transistor, whereas other times the signal is phase modulated

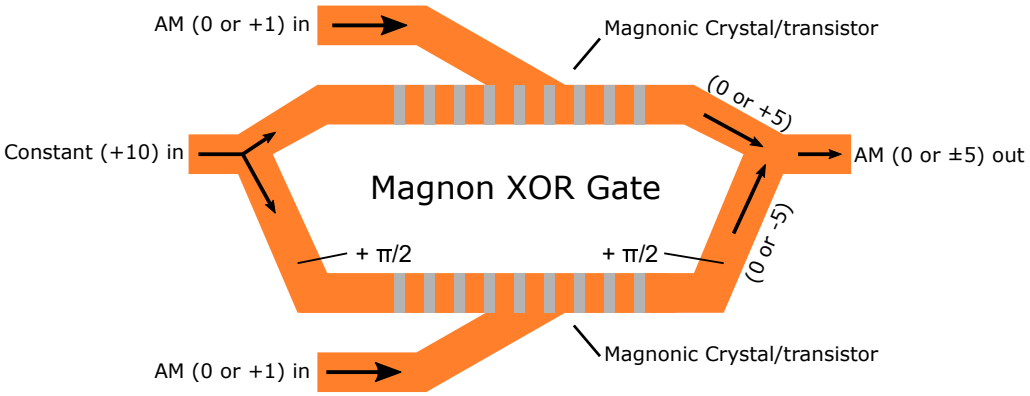


Figure 1.8: Schematic of the all-magnon XOR gate. The device operates in a similar fashion to the magnon amplifier, however now both branches contain a transistor. If exactly one gate is open, then a signal is able to flow. If both or neither are open, then the output is zero due to destructive interference, or a simple lack of magnons.

(PM), such as with the majority gate. Chapter 4 attempts to address this problem of how to convert between amplitude and phase modulated signals.

The second challenge that is investigated is that of magnon multiplexing. As mentioned in the discussion of the majority gate in §1.3.1, several signals can be theoretically processed simultaneously if different frequencies are used to carry them. How these signals can be separated from each other, and what effect they have on each other inside the waveguide are a few of the problems of multiplexing addressed in Chapter 5. In this chapter, the quantity of data that can be sent down a waveguide in any given time window is considered, and a method for doubling this value known as quadrature phase-shift keying (QPSK) is discussed.

Chapter 2

The Spin Battery: Theory

2.1 Overhauser Introduction: something old, something new...

As mentioned in §1.1.2, the Spintronics community is relatively young, beginning in earnest in the 1990's with the discovery of giant magnetoresistance [4, 5] and spin injection [3]. At least that is what anyone who works in the area will tell you. In reality, active research into the behaviour of spins (both electronic and nuclear) in condensed matter has been ongoing since the middle of the 20^{th} Century under the stewardship of the magnetic resonance community [30]. Even though both communities deal in the same currency, spin angular momenta, there has been surprisingly little communication between the two. Investigating how applicable some of the well-established techniques developed over 50 years ago are to today's Spintronic problems was the starting point of this work, and has led to the development of a new Spin Battery device based on the Overhauser effect, which was published here [31].

The Overhauser Effect is a resonance technique in which microwave excitation of the electronic system in a metal leads to the polarization of its nuclei [32]. A full derivation of the system can be found in reference [30], however an outline of the physical processes involved can be found below.

2.2 Pre-requisite Theory

2.2.1 Magnetic Resonance

The two most common forms of magnetic resonance are nuclear magnetic resonance (NMR) and electron paramagnetic spin resonance (ESR or EPR). The typical frequency ranges for these types are radio and microwave frequencies respectively. The underlying mechanisms behind electronic and nuclear magnetic resonance are almost identical. As this work is predominantly interested in ESR, electronic spins will be used in the subsequent description, but a nuclear spin could easily be substituted.

When a magnetic moment is placed in an external magnetic field, a torque arises which tends to align the moment with the applied $\boldsymbol{B}$ field, minimizing the energy $\mathcal{H} = -\boldsymbol{\mu} \cdot \boldsymbol{B}$. If the magnetic moment has an associated angular momentum, the torque leads to gyroscopic precession. For a given magnetic field and moment, this precession has a characteristic frequency, known as the Larmor frequency [30]. If a second external magnetic field is also applied to the moment, this time varying in time at the Larmor frequency, the field is said to be resonant. This resonant field is able to force the magnetic moment to transition between spin states, which, for spin-half systems such as electrons, lead to 'spin-flips'. These 'spin-flips' can be thought of in the quantum picture as an electron transitioning between two Zeeman-split energy levels. The change in energy between these two states is accounted for by the absorption or emission of a resonant photon.

Gyromagnetic ratios

The relationship between the magnetic moment of a particle and its spin angular momentum is known as the gyromagnetic ratio, and is given by the simple ratio: $\gamma = \frac{m}{S}$, where m is the magnetic moment and S is the spin angular momentum. If the derivation of the Larmor precession found in reference [30] is followed, it is found that $\gamma = \frac{\omega}{|\boldsymbol{B}|}$, where ω is the Larmor precession frequency, and $|\boldsymbol{B}|$ is the applied magnetic field. A useful form of this parameter is given when divided by

2π, as $\frac{\gamma}{2\pi} = \frac{f}{|\boldsymbol{B}|}$, which for a free electron is known to be $28.02495164(17)\,\mathrm{GHzT}^{-1}$ [33]. This is a useful form for laboratory use, as once the resonance frequency of the microwave cavity detector has been determined, the appropriate magnetic field that would lead to the sample resonating at that frequency can be applied.

Another useful quantity is the g-factor, which is extracted from $\frac{f}{|\boldsymbol{B}|}$ by dividing by $\frac{\mu_\mathrm{B}}{h}$, which has a numerical value of $13.996378\,\mathrm{GHz\,T}^{-1}$. This provides a dimensionless value (which for the electron is $g_e \approx -2.00232$ [33]) which is sometimes easier to work with than the other related quantities. All of these relationships are summarized in the equation:

$$\gamma_\mathrm{e} = \frac{q_\mathrm{e}}{2m_\mathrm{e}} g_\mathrm{e} = 2\pi \times 13.996378\,\mathrm{GHz\,T}^{-1} g_\mathrm{e} = \frac{g_\mathrm{e}\mu_\mathrm{B}}{\hbar} = \frac{\omega}{B}$$

Ferromagnetic resonance

A third kind of magnetic resonance is ferromagnetic resonance, or FMR. As the name suggests, this applies when performing magnetic resonance in a ferromagnetic material (although it can also occur in ferrimagnets too). Due to the exchange interaction, the spins in the sample prefer to align with one another to form a coherent macroscopic quantum state, which responds to resonant microwave excitations as a single precessing magnetic moment. This system can be treated in a similar fashion to ESR, however the individual electronic spin $\boldsymbol{S}$ must now be replaced by the much larger macroscopic magnetization $\boldsymbol{M}$. The resonance frequency for FMR also shifts from the ESR value of $\omega_{res} = \gamma|\boldsymbol{B}|$ to $\omega_\mathrm{FMR} = \gamma\sqrt{|\boldsymbol{B}|(|\boldsymbol{B}| + \mu_0|\boldsymbol{M}|)}$ for the case of a thin film sample with an in-plane field [7]. Ferromagnets are discussed further in §3.3.2.

2.2.2 Spin-flip relaxation channels

So far, only the way in which magnetic resonance can be used to drive electrons from one spin state to another has been discussed. Normally only the excitation part of this interaction is considered, where the energy of the spin is increased as

it transitions to a higher energy state, however it is also possible that the resonant absorption can cause a stimulated emission, relaxing the spin back to its lower spin state.

There are several mechanisms by which spins can relax back to their lower energy state. Collectively, these can be characterized by a certain relaxation time, the spin-flip relaxation time, $\tau_{\uparrow\downarrow}$. This parameter includes contributions from (for example) magnetic impurity scattering, phonon interactions, and spin-orbit interactions. Two specific spin-relaxation channels relevant to our particular experiments are the dipole-dipole interaction, and the Fermi contact interaction, which are discussed below.

Dipole-dipole interaction and the Fermi Contact interaction

The dipole-dipole interaction describes the interaction between two different spins, or magnetic dipoles, separated by $\boldsymbol{r}$. The general Hamiltonian of this interaction can be written as: [30]

$$\mathcal{H} = -\frac{\mu_0 \gamma_1 \gamma_2 \hbar^2}{4\pi |\boldsymbol{r}|^3} \left(3 \left(\boldsymbol{S}_1 \cdot \hat{\boldsymbol{r}}\right) \left(\boldsymbol{S}_2 \cdot \hat{\boldsymbol{r}}\right) - \boldsymbol{S}_1 \cdot \boldsymbol{S}_2\right) \tag{2.1}$$

Using the well-known formula for raising and lowering operators $S^{\pm} = S_x \pm iS_y$ [34], and some inspired substitutions (notably, $1 = \frac{3}{2}(\sin^2\theta + \cos^2\theta) - \frac{1}{2}$), this can be arranged into the form

$$
\begin{aligned}
\mathcal{H} &= \frac{\mu_0 \gamma_1 \gamma_2 \hbar^2}{4\pi |\boldsymbol{r}|^3}(A + B + C + D + E + F) \\
A &= S_{1z} S_{2z}(1 - 3\cos^2\theta) \\
B &= -\frac{1}{4}({S_1}^+ {S_2}^- + {S_1}^- {S_2}^+)(1 - 3\cos^2\theta) \\
C &= -\frac{3}{2}({S_1}^+ S_{2z} + S_{1z} {S_2}^+)\sin\theta\cos\theta \mathrm{e}^{-i\phi} \\
D &= -\frac{3}{2}({S_1}^- S_{2z} + S_{1z} {S_2}^-)\sin\theta\cos\theta \mathrm{e}^{i\phi} \\
E &= -\frac{3}{4} {S_1}^+ {S_2}^+ \sin^2\theta \mathrm{e}^{-2i\phi} \\
F &= -\frac{3}{4} {S_1}^- {S_2}^- \sin^2\theta \mathrm{e}^{2i\phi}
\end{aligned}
\tag{2.2}
$$

Looking at this equation, it can be seen that there are terms that result in both spins increasing or decreasing their S_z value, which are termed 'flip-flip' or 'flop-flop' terms. There are also terms that lead to one particle being raised while the other is lowered, which are termed 'flip-flop' terms. Terms of this form are vitally important to the Overhauser effect, and will be discussed further later.

In systems where the two spin species are in fixed positions with respect to each other (such as two neighbouring nuclei, or a nucleus and an electron which is bound to a nearby magnetic impurity), equation 2.1 can be used in its present form. If one spin system is delocalised, and is free to move around with respect to the other (as is the case for an itinerant electron and a nucleus), then equation 2.1 is no longer sufficient to describe the magnetic interaction, and the Fermi Contact Interaction must be considered instead.

The Fermi Contact Interaction The dipole-dipole interaction works well for magnetic particles that are spatially separated. In the case of an electron orbiting a nucleus in its S-state, there is a non-zero probability that the electron will be found *inside* the nucleus. This causes problems as the dipole-dipole interaction blows up to infinity. When this problem is resolved properly [35], the new Fermi Contact

Interaction Hamiltonian can be found:

$$\begin{aligned} \mathcal{H} &= A\boldsymbol{I}\cdot\boldsymbol{J} \\ A &= -\frac{2}{3}\mu_0 \left\langle \boldsymbol{\mu_n}\cdot\boldsymbol{\mu_e}\right\rangle |\Psi(0)|^2 \end{aligned} \tag{2.3}$$

Interestingly, the vectors here can be expanded into the form

$$\boldsymbol{I}\cdot\boldsymbol{J} = I_z J_z + \frac{1}{2}(I^+J^- + I^-J^+)$$

which contains the same operator terms as the B term of the dipole-dipole interaction. This means that both interactions enable 'flip-flop' transitions. As both the dipole-dipole interaction and the Fermi contact interaction enable electrons to flip their spins, they both provide additional relaxation channels to an excited electron. The significance of these 'flip-flop' type interactions are discussed in the next section.

2.3 Overhauser theory

The Overhauser effect is a two-step process in which microwave pumping of a material's electronic system leads to the polarization of the nuclei within the material. A good discussion on the subject can be found in reference [30], however it will also be discussed here.

2.3.1 The energy level diagram

Initially the energy level diagram for electron-nucleus pairs in an applied magnetic field is considered. This is presented in Figure 2.1. In this diagram, the strength of the nuclear Zeeman interaction is greater than the $\boldsymbol{I}\cdot\boldsymbol{J}$ interaction. The energy levels begin thermally populated, with the electrons polarized and the nuclei unpolarized. By applying a microwave field at the electron transition frequency, some electrons are excited into their upper states. These are able to relax back to their ground-states via direct, 'allowed' transitions, so eventually a dynamic equilibrium is reached.

Due to the presence of the $\boldsymbol{I}\cdot\boldsymbol{J}$ interaction, 'flip-flop' relaxation processes are also

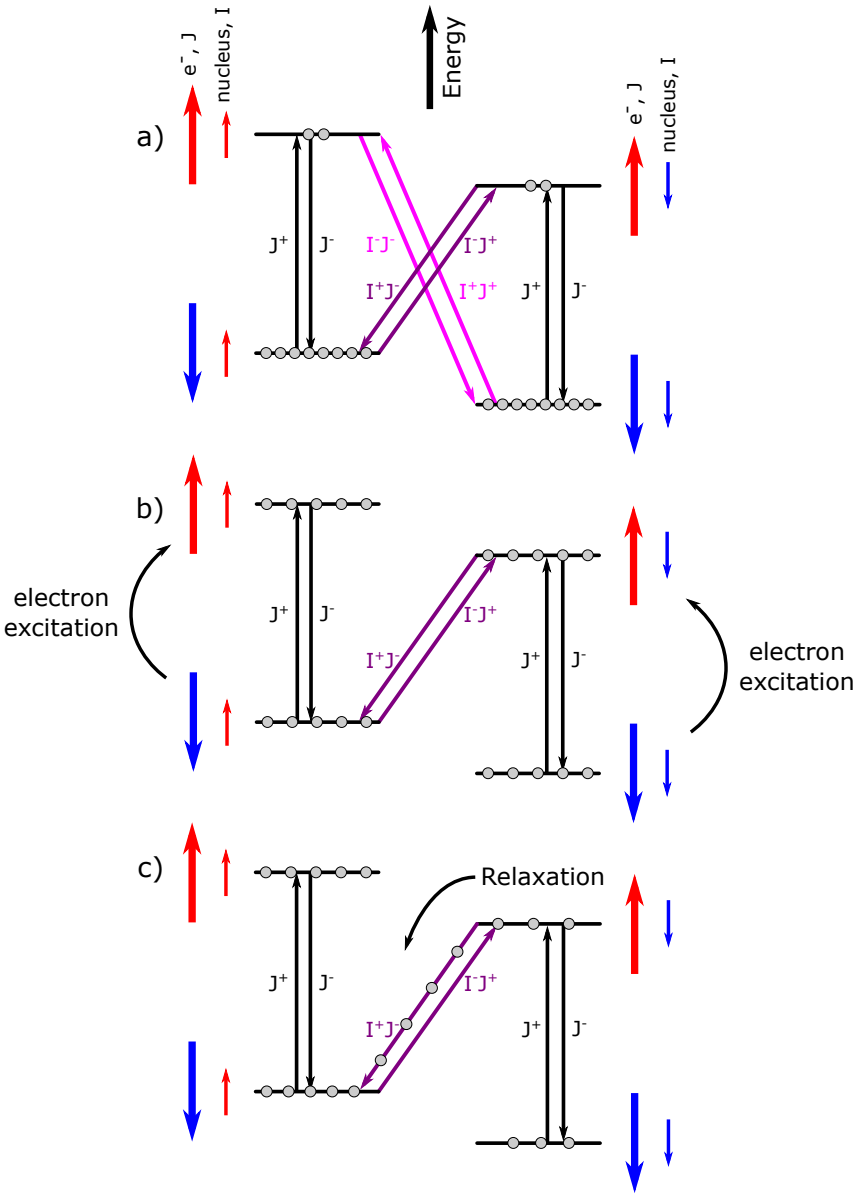


Figure 2.1: The Overhauser effect understood via energy level diagrams for an electron-nucleus system. The energy levels represent the combined energy of any given electron-nucleus pair, and are labelled by the corresponding spin states (The large and small arrows representing the electron and the nuclear spins respectively). The grey circles illustrate the relative population of the states. a) The energy levels for the thermal equilibrium state in an applied magnetic field, with both direct, flip-flip, and flip-flop transitions indicated. Each side of the diagram is equally populated, so there is no net nuclear polarization. b) An excited state, in which microwave pumping has excited electrons from their lower state. The excited electrons can now relax via single spin flips, or the flip-flop transition. Flip-flip relaxations are also possible, however due to the dominance of the Fermi Contact interaction, they are relatively slow, so have been removed from the diagram. c) Flip-flop relaxations lead to states on the left of the diagram being much more populated than the states on the right. This represents the creation of a nuclear polarization, which is the expected outcome of the Overhauser Effect.

active. Over time this will lead to states on the left-hand side of the diagram cross-relaxing to the right through this flip-flop process. Greater occupancy of states on one side of the diagram than the other represents a nuclear polarization, the predicted outcome of the Overhauser effect.

Aside: The Solid Effect

In the case where the dipole-dipole interaction is present, and the Fermi contact interaction is absent, both 'flip-flip' and 'flip-flop' processes can be exploited. If microwaves are applied at either of these frequencies (corresponding to the electron Zeeman energy ± nuclear Zeeman energy), it is possible to drive these 'forbidden' transitions. Driving these transitions effectively equalizes the populations of these two states, which are then able to reach equilibrium with the rest of the system. The equilibrium reached will have polarized nuclei, but the polarization will depend on which of the diagonal transitions was pumped. This process is known as the 'Solid Effect', and together with the Overhauser effect are collectively known as 'Dynamic Nuclear Polarization'.

2.3.2 The Overhauser effect in metals

Spin channels and Pauli paramagnetism

In a metal, the electrons are not bound to specific atoms, but are itinerant. The behaviour of such electrons is well encapsulated in bandstructure theory, as is their behaviour under an applied magnetic field with the Pauli paramagnetism model [11]. Fortunately, not only it is possible to explain the Overhauser effect within the confines of this model, it also provides the first step towards understanding the Spin Battery proposal.

Figure 2.2a shows the simple bandstructure of an idealized paramagnetic metal with no externally applied field. The density of states and the electrochemical potential ($\bar{\mu}$) are presented separately for each spin species. This is necessary as the two 'spin channels' do not behave in the same way under the application of magnetic

fields.

Figure 2.2b shows how the bandstructure of the metal changes after the instantaneous application of a magnetic field. The electrochemical potential of the two bands is now split by an energy of $\Delta E = 2\mu_B B$. After a period of time on the order of the spin-flip relaxation time $\tau_{\uparrow\downarrow}$, the system will have relaxed in such a way as to equalize the electrochemical potentials of the two channels. This is depicted in Figure 2.2c. This three-step process is the same familiar story of Pauli paramagnetism presented in elementary condensed matter physics textbooks [11].

Figure 2.2d shows what happens to the system under the application of a resonant microwave field. The microwaves work to equalize the populations of the two spin channels [35], driving spins from the lower energy, more populous channel into the higher energy spin state. Just as with the energy level description in §2.3.1, a dynamic equilibrium will form that balances the microwave excitations with the spin-flip relaxation rate. This equilibrium can be characterized by the difference between the electrochemical potentials of the two channels $\Delta\bar{\mu}_{\uparrow\downarrow}$, and is known as the electrochemical potential difference. Under very strong microwave pumping, the limit may be reached in which the population difference between the two channels has been removed entirely, and the full electrochemical potential splitting of $\Delta\bar{\mu}_{\uparrow\downarrow} = 2\mu_B B$ is restored. This is the state presented in Figure 2.2d.

Figure 2.2e shows two possible relaxation processes for the excited electrons. This includes the 'allowed' transition J^-, and the 'forbidden' transition J^-I^+, which correspond to vertical and diagonal relaxation transitions in Figure 2.1 respectively. The J^-I^+ transition in Figure 2.2e is not horizontal, as the vertical axis of this diagram represents electronic energy only, and this transition transfers some energy to the nuclear system.

In both Figures 2.1 and 2.2, it can be seen that direct pumping of the electron transition leads to the electronic spin system entering a non-equilibrium state. In the case of the metal, this is identified as an electrochemical splitting. In the language of Spintronics, this electrochemical splitting is called a 'spin accumulation', and it

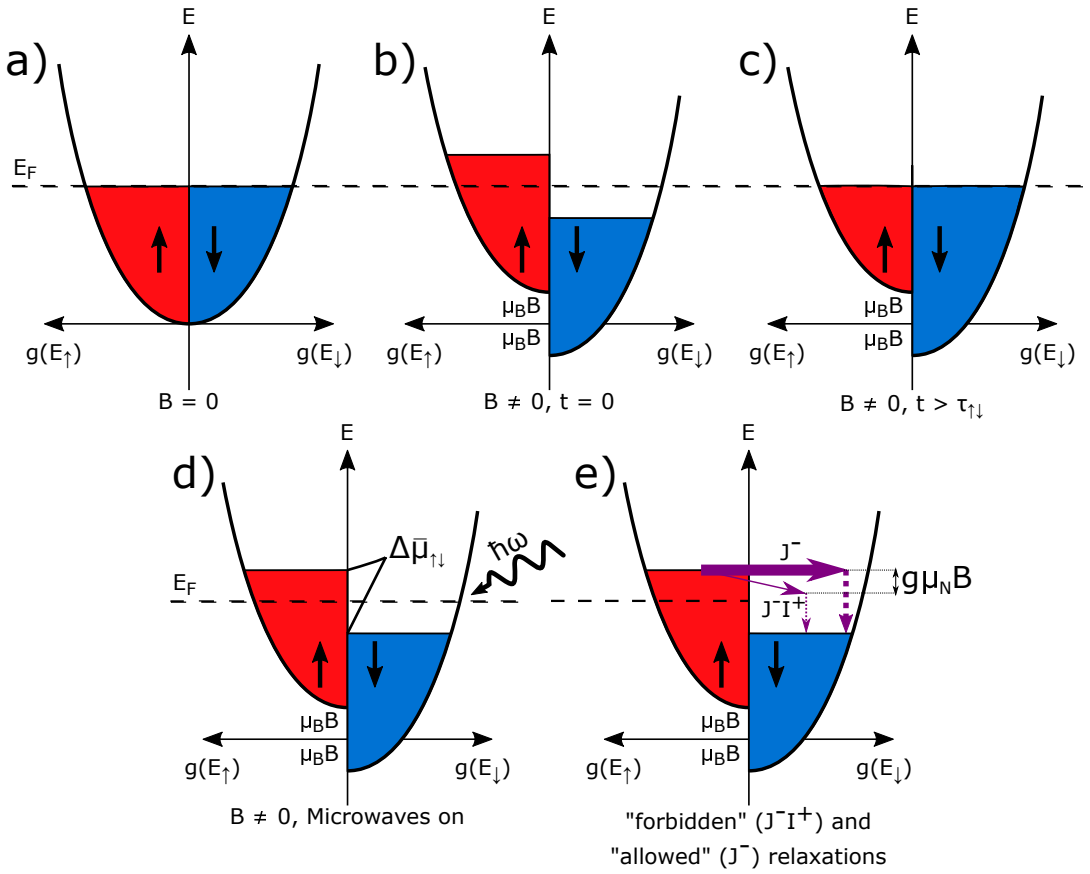


Figure 2.2: Bandstructure of a simple paramagnetic metal. a) shows the bandstructure of an ideal paramagnetic metal. b) shows the effect of instantaneously applying a magnetic field to the metal. Note the transient electrochemical splitting that appears between the two spin channels. c) depicts the system after it has had time to relax. In d), the electrochemical potential splitting has been restored by applying strong microwave radiation. e) shows two different relaxation channels that an excited electron may take. One of these (the 'forbidden' J^-I^+ transition) leads to polarization of the nuclei.

is this element of the Overhauser effect that will be used to generate a pure spin current in the Spin Battery.

2.4 The Spin Battery Model

2.4.1 The general principle

In Figure 2.2d, a spin accumulation was created by microwaving a metallic sample, and was characterized by the parameter $\Delta\bar{\mu}_{\uparrow\downarrow}$, the electrochemical potential splitting. Figure 2.2e showed two ways that this electrochemical potential splitting could relax, via two different types of spin-flip relaxation process. But what happens if a third relaxation method is introduced: diffusion?

If a region within a uniform-density electron gas is considered that contains more up spins than down, then that region, unlike the rest of the gas, has a non-zero $\Delta\bar{\mu}_{\uparrow\downarrow}$. Random diffusion processes (which can be characterised by Fick's first law: Flux $= -D\boldsymbol{\nabla}n$ where D is the diffusion constant, and n is the number density [36]) lead to more up spins diffusing away from the region than towards, and similarly, more down spins diffusing into the region than away. This process represents a net flow of up electrons out and down electrons in, which is identified as a spin current. In terms of $\Delta\bar{\mu}_{\uparrow\downarrow}$, a spin current has flown down the electrochemical potential gradient. Using the effective density of states (ρ^*) introduced in §2.4.2, this spin current can be written as $\boldsymbol{J_s} = -D\rho^*\boldsymbol{\nabla}\Delta\bar{\mu}_{\uparrow\downarrow}$.

If a situation can be devised in which an electrochemical potential gradient is present in a system where $\Delta\bar{\mu}_{\uparrow\downarrow}$ is symmetrical about the Fermi surface, then it will be possible to produce a pure spin current, in which angular momentum is able to flow unencumbered by charge transport.

One way of engineering such a situation would be to create an interface between a microwave excited material and a second material in which the spin relaxation time is very short. This would in effect 'short-circuit' the two spin channels, resulting in $\Delta\bar{\mu}_{\uparrow\downarrow} \approx 0$. This would lead to greatly differing electrochemical potential differences,

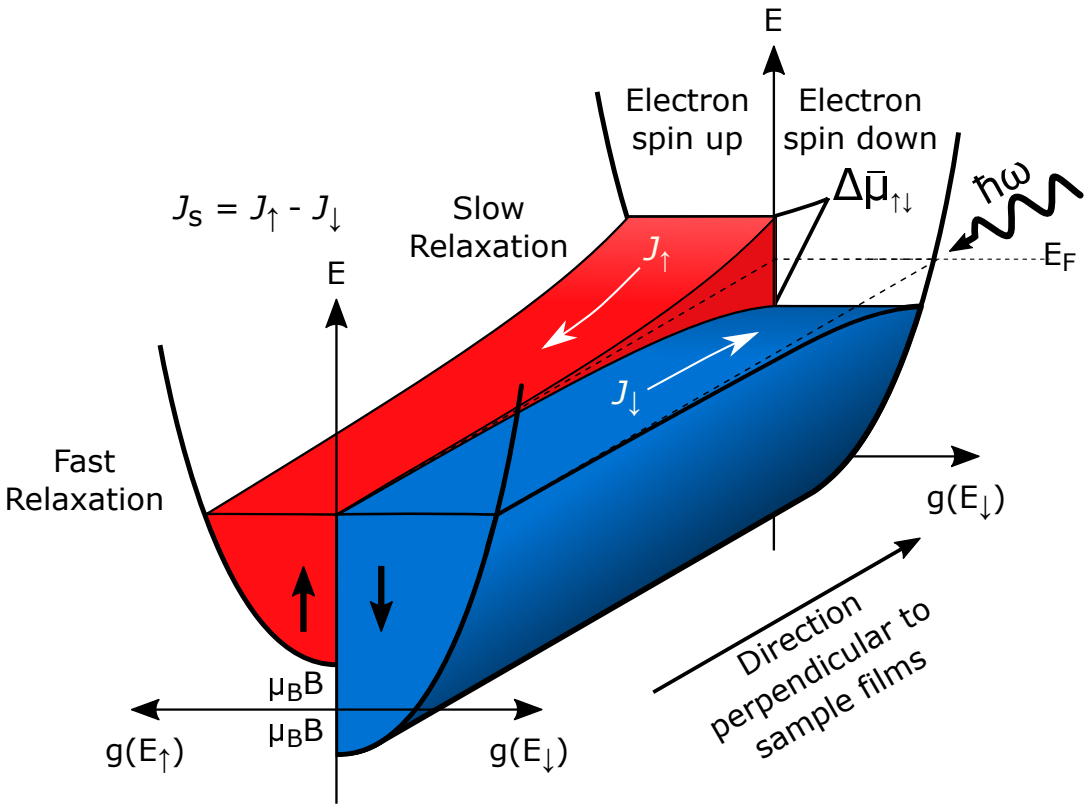


Figure 2.3: The principle behind the Overhauser Spin Battery. The two spin channels are depicted for a metal bilayer in which the two metals have vastly differing spin-flip relaxation times. The electrochemical potential gradients for each spin species leads to two 'impure' spin currents $J_\uparrow$ and $J_\downarrow$. When both of these are considered simultaneously, a flow of angular momentum is observed with no net flow of charge: a 'pure' spin current $\boldsymbol{J_s}$.

which would in turn result in an electrochemical potential gradient, and thus a spin current. This is depicted in Figure 2.3. In this plot, it can be seen how the spatial variation in the electrochemical potentials for each channel leads to counter propagating spin currents. As the flows are always of the same size, the resultant net flow is a pure spin current. This method of pure spin current generation is christened the 'Overhauser Spin Battery'.

2.4.2 Electrochemical potential splitting to number densities

To model the Overhauser Spin Battery, diffusion-like equations (which are usually written in terms of particle number) are necessary. Presently, the parameter in use

($\Delta\bar{\mu}_{\uparrow\downarrow}$) is in energy units, so a way of relating this to a spin density is required.

The 'undergraduate' way of making this conversion (as seen when determining the magnetization of a Pauli paramagnet [11]) is to simply multiply the density of states at the Fermi energy $g(E_\mathrm{F})$ by the relevant energy difference (e.g. $\mu_\mathrm{B}B$). This works if one assumes that the density of states is flat over the region of interest, and that $T = 0$ (which leads to a clean step in population at the Fermi surface).

For a real system, these approximations are not necessarily valid. For $T \neq 0$, the population of a given state is weighted by the Fermi function $f(\epsilon)$, where

$$f(\epsilon) = \frac{1}{\mathrm{e}^{(\epsilon-\bar{\mu})/kT} + 1}$$

A way to incorporate this into the calculation is to use an 'effective density of states' ρ^*, where

$$\rho^* = \int g(\epsilon) f'(\epsilon) \mathrm{d}\epsilon$$

and $f'(\epsilon)$ is the derivative of the Fermi function. As the density of states $g(\epsilon)$ can be different for each spin channel, two different effective densities of state, ${\rho_\uparrow}^*$ and ${\rho_\downarrow}^*$ arise. Multiplying the effective density of states by the electrochemical potentials for each channel ($\bar{\mu}_\uparrow$,$\bar{\mu}_\downarrow$) gives the particle number densities for each spin species, $n_\uparrow$ and $n_\downarrow$, which represents the deviation away from the static equilibrium population for each channel.

While it is possible to construct and solve diffusion equations for each of these spin channels, one further step can be taken to save work later. If the difference between $n_\uparrow$ and $n_\downarrow$ is found, the evolution of the spin accumulation can be calculated directly. By noting that in a simple paramagnetic metal, ${\rho_\uparrow}^* \approx {\rho_\downarrow}^* \approx \rho^*$, $n_\uparrow - n_\downarrow$ can be expanded and simplified as follows:

$$n_\uparrow - n_\downarrow = {\rho_\uparrow}^* \bar{\mu}_\uparrow - {\rho_\downarrow}^* \bar{\mu}_\downarrow = \rho^* \Delta\bar{\mu}_{\uparrow\downarrow}$$

This allows for the spin accumulation to be described using $\rho^*\Delta\bar{\mu}_{\uparrow\downarrow}$, which is a quantity whose evolution can be calculated via diffusion-like equations.

2.4.3 The Diffusion-like equations

Having converted the electrochemical potential splitting into a number density, an equation can be set up to describe how the spin accumulation evolves over time. Beginning with the continuity equation and accounting for spin current, spin-flip relaxation ($\tau_{\uparrow\downarrow}$ is the spin-flip relaxation time), and spin excitation (R is the number of spins excited per second per unit volume), a one-dimensional equation that describes the evolution of the spin accumulation can be written down.

$$\begin{aligned} &\rho^* \frac{\mathrm{d}\Delta\bar{\mu}_{\uparrow\downarrow}}{\mathrm{d}t} = -\boldsymbol{\nabla}\cdot\boldsymbol{J}_{\mathbf{s}} - \frac{\rho^*\Delta\bar{\mu}_{\uparrow\downarrow}}{\tau_{\uparrow\downarrow}} + R = 0 \\ =&\rho^* \frac{\mathrm{d}\Delta\bar{\mu}_{\uparrow\downarrow}}{\mathrm{d}t} = \rho^* D\nabla^2\Delta\bar{\mu}_{\uparrow\downarrow} - \frac{\rho^*\Delta\bar{\mu}_{\uparrow\downarrow}}{\tau_{\uparrow\downarrow}} + R = 0 \\ =&\rho^* D\frac{\partial^2\Delta\bar{\mu}_{\uparrow\downarrow}}{\partial x^2} - \frac{\rho^*\Delta\bar{\mu}_{\uparrow\downarrow}}{\tau_{\uparrow\downarrow}} + R = 0 \end{aligned} \tag{2.4}$$

Solving these equations will require boundary conditions, and to apply boundary conditions an experiment is needed.

2.4.4 The Spin Battery Experiment

The simplest Spin Battery experiment takes the form a metallic bilayer in which one material (the Relaxer) has a much faster spin-flip relaxation time than the other (the Host). The Host must also have an excitable ESR transition. The experimental arrangement of such a device is shown in Figure 2.4.

The thicknesses of each of the films are shown on the x axis, as are the directions of the applied static and microwave fields. If the Relaxer has a large spin Hall angle, then any spin current travelling in the x direction will be converted into a voltage in the y direction via the inverse spin Hall effect (§1.2.4). This voltage can be detected by the voltmeter shown in the diagram, and provides evidence that a spin current has been generated.

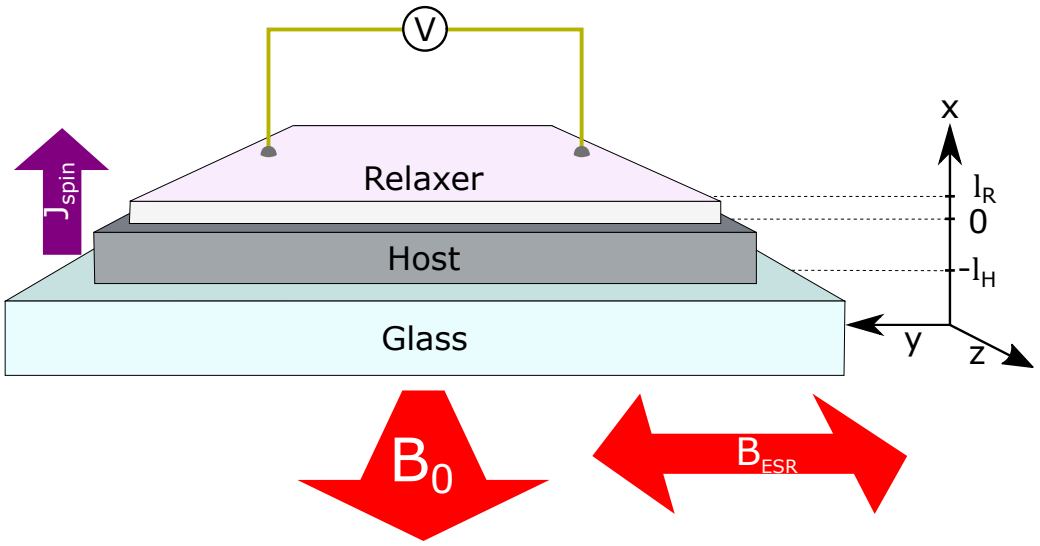


Figure 2.4: The Spin Battery experiment. Resonant microwave excitations in the Host lead to an electrochemical potential gradient which drives spins into the Relaxer. If the Relaxer has a large spin Hall angle, then the spin current will be converted into a measurable inverse spin Hall voltage.

2.4.5 Solving the equations

Using the experimental arrangement in Figure 2.4, the boundary conditions of the system can be written down:

$$\begin{aligned}
&\boldsymbol{J}_{\mathrm{s_H}}(0) = \boldsymbol{J}_{\mathrm{s_R}}(0) = -\rho^* D_{\mathrm{H}} \boldsymbol{\nabla} \Delta\bar{\mu}_{\uparrow\downarrow_{\mathrm{H}}}(0) = -\rho^* D_{\mathrm{R}} \boldsymbol{\nabla} \Delta\bar{\mu}_{\uparrow\downarrow_{\mathrm{R}}}(0) \\
&\Delta\bar{\mu}_{\uparrow\downarrow_{\mathrm{H}}}(0) = \Delta\bar{\mu}_{\uparrow\downarrow_{\mathrm{R}}}(0) \\
&-\rho^* D_{\mathrm{H}} \boldsymbol{\nabla} \Delta\bar{\mu}_{\uparrow\downarrow_{\mathrm{H}}}(-l_{\mathrm{H}}) = 0 \\
&-\rho^* D_{\mathrm{R}} \boldsymbol{\nabla} \Delta\bar{\mu}_{\uparrow\downarrow_{\mathrm{R}}}(l_{\mathrm{R}}) = 0
\end{aligned} \tag{2.5}$$

which leads to solutions:

$$\begin{aligned}
\rho^* \Delta\bar{\mu}_{\uparrow\downarrow_{\mathrm{H}}} &= \left(\frac{(R_{\mathrm{R}}\tau_{\uparrow\downarrow_{\mathrm{H}}} - R_{\mathrm{H}}\tau_{\uparrow\downarrow_{\mathrm{R}}}) D_{\mathrm{R}} \lambda_{\mathrm{H}}}{\left(D_{\mathrm{R}}\lambda_{\mathrm{H}} \coth\left(\frac{l_{\mathrm{H}}}{\lambda_{\mathrm{H}}}\right) + D_{\mathrm{H}}\lambda_{\mathrm{R}} \coth\left(\frac{l_{\mathrm{R}}}{\lambda_{\mathrm{R}}}\right) \right)} \right) \left(\frac{\cosh\left(\frac{x+l_{\mathrm{H}}}{\lambda_{\mathrm{H}}}\right)}{\sinh\left(\frac{l_{\mathrm{H}}}{\lambda_{\mathrm{H}}}\right)} \right) + R_{\mathrm{H}}\tau_{\uparrow\downarrow_{\mathrm{H}}} \\
\rho^* \Delta\bar{\mu}_{\uparrow\downarrow_{\mathrm{R}}} &= \left(\frac{(R_{\mathrm{R}}\tau_{\uparrow\downarrow_{\mathrm{H}}} - R_{\mathrm{H}}\tau_{\uparrow\downarrow_{\mathrm{R}}}) D_{\mathrm{H}} \lambda_{\mathrm{R}}}{\left(D_{\mathrm{R}}\lambda_{\mathrm{H}} \coth\left(\frac{l_{\mathrm{H}}}{\lambda_{\mathrm{H}}}\right) + D_{\mathrm{H}}\lambda_{\mathrm{R}} \coth\left(\frac{l_{\mathrm{R}}}{\lambda_{\mathrm{R}}}\right) \right)} \right) \left(\frac{\cosh\left(\frac{x-l_{\mathrm{R}}}{\lambda_{\mathrm{R}}}\right)}{\sinh\left(\frac{l_{\mathrm{R}}}{\lambda_{\mathrm{R}}}\right)} \right) + R_{\mathrm{R}}\tau_{\uparrow\downarrow_{\mathrm{R}}}
\end{aligned} \tag{2.6}$$

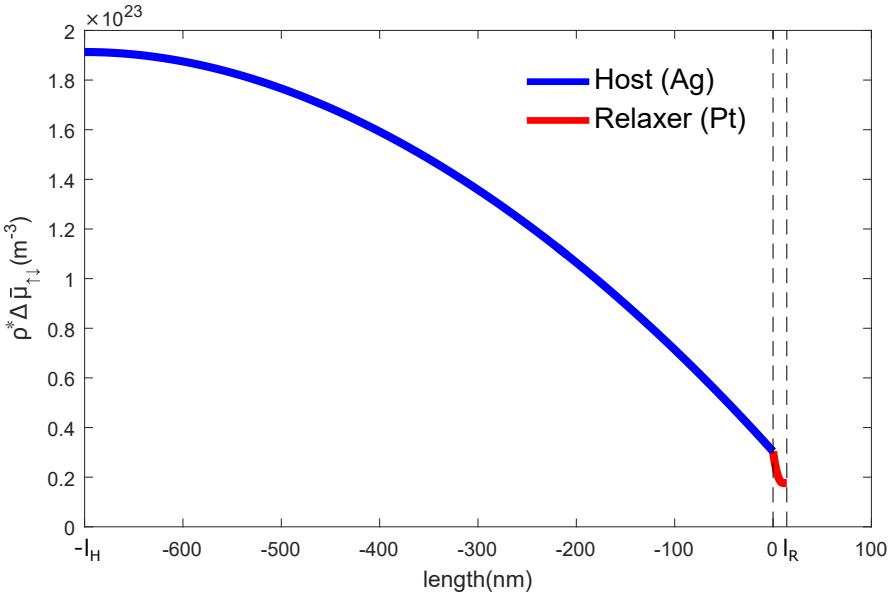


Figure 2.5: The behaviour of the spin accumulation $\rho^*\Delta\bar{\mu}_{\uparrow\downarrow}$ in the Spin Battery device as predicted by the spin battery model. The resulting gradient in $\rho^*\Delta\bar{\mu}_{\uparrow\downarrow}$ is the origin of the spin-motive force which drives the spin current into the Relaxer. The parameters used here were: $l_{\mathrm{H}} = \lambda_{\mathrm{H}} = 700\,\mathrm{nm}$ [38], $l_{\mathrm{R}} = \lambda_{\mathrm{R}} = 7.3\,\mathrm{nm}$ [38], $R_{\mathrm{H}} = R_{\mathrm{R}} = 1.2 \times 10^{32}\,\mathrm{s^{-1}m^{-3}}$, $\rho_{\mathrm{H}} = 1.59 \times 10^{-8}\,\Omega\mathrm{m}$, and $\rho_{\mathrm{R}} = 1.06 \times 10^{-8}\,\Omega\mathrm{m}$.

where λ is the spin relaxation length, defined as

$$\lambda = \sqrt{D\tau_{\uparrow\downarrow}}. \tag{2.7}$$

D can be calculated using the Einstein relation [10]

$$D = \frac{k_{\mathrm{B}}T}{\rho n e^2}. \tag{2.8}$$

where n is the electron number density and ρ is the resistivity.

Equation 2.6 describes the steady-state solution for the spin accumulation across the two halves of the metallic bilayer. The solutions are plotted for a silver/platinum bilayer in Figure 2.5, using the parameter values shown in the caption. Silver and platinum are two of the materials used in the later experiments, as silver has a slow spin-flip relaxation time compared to platinum [37], and platinum is known to have a large spin Hall angle, which makes it ideal for spin current detection [38].

2.4.6 The inverse spin Hall voltage generated from the spin current

The next part of the calculation is to determine the thicknesses of the metal layers that optimizes the inverse spin Hall voltage. The two relevant equations here are

$$\boldsymbol{J_s} = -D\rho^* \boldsymbol{\nabla} \Delta\bar{\mu}_{\uparrow\downarrow}$$

$$\boldsymbol{J_c} \propto \theta_{\text{ISHE}} \boldsymbol{J_s} \times \boldsymbol{\sigma}$$

where $\boldsymbol{J_s}$ and $\boldsymbol{J_c}$ are the spin and charge currents respectively, and $\boldsymbol{\sigma}$ is the polarization of the spins. θ_{ISHE} is the inverse spin Hall angle, and represents the degree to which a travelling spin is perpendicularly diverted from its original path by the spin Hall effect [39].

To calculate the voltage generated from the inverse spin Hall effect, a monolayer is divided up into slices of thickness Δx. Each slice acts as both a resistor and a current source (as it will generate charge current proportional to the spin current flowing through the slice). Figure 2.6 depicts this for the case of only three slices. By applying Ohms law and taking the continuum case as $\Delta x \to 0$, an equation for the expected inverse spin Hall voltage from a monolayer film of thickness l can be reached:

$$V = \rho y \frac{\int_0^l j_c(x)\mathrm{d}x}{\int_0^l \mathrm{d}x}.$$

Expanding this analysis to a bilayer with thicknesses l_{H} and l_{R} for the two metals, the ISHE voltage for a spin current in the bilayer is given by:

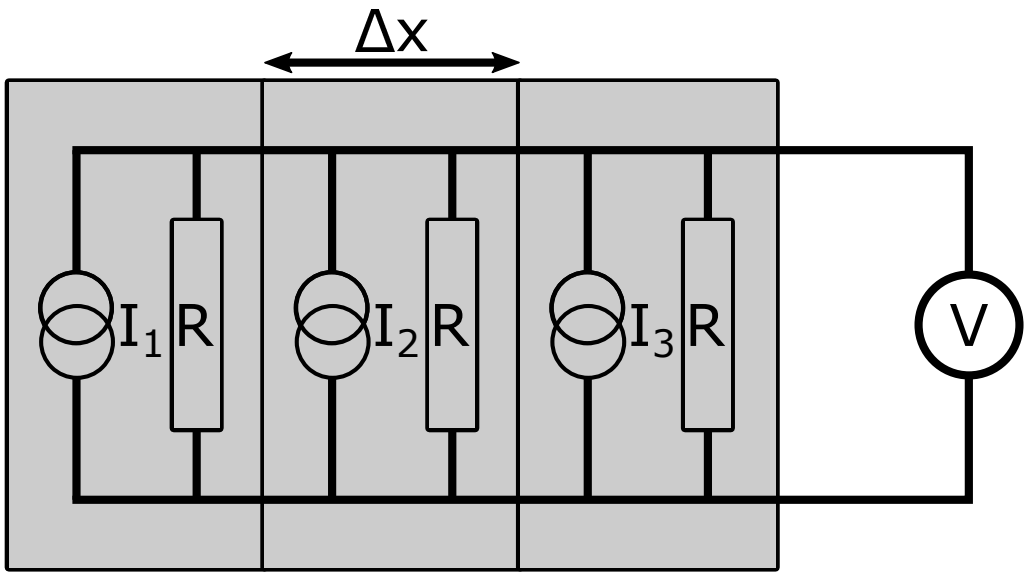


Figure 2.6: Diagram of the slice model for calculating the inverse spin Hall voltage in an irradiated metal sample.

$$
\begin{aligned}
V &= \left(\frac{\rho_{\mathrm{H}}\rho_{\mathrm{R}}}{(\rho_{\mathrm{H}}l_{\mathrm{R}}+\rho_{\mathrm{R}}l_{\mathrm{H}})}\right) y \left(\int_{-l_{\mathrm{H}}}^{0} j_{c_{\mathrm{H}}}(x)dx + \int_{0}^{l_{\mathrm{R}}} j_{c_{\mathrm{R}}}(x)dx\right) \\
V &= e\left(\frac{\rho_{\mathrm{H}}\rho_{\mathrm{R}}}{(\rho_{\mathrm{H}}l_{\mathrm{R}}+\rho_{\mathrm{R}}l_{\mathrm{H}})}\right) y \left(D_{\mathrm{H}}\theta_{\mathrm{ISHE_H}}\int_{-l_{\mathrm{H}}}^{0}\rho^{*}\nabla\Delta\bar{\mu}_{\uparrow\downarrow_{\mathrm{H}}}dx + D_{\mathrm{R}}\theta_{\mathrm{ISHE_R}}\int_{0}^{l_{\mathrm{R}}}\rho^{*}\nabla\Delta\bar{\mu}_{\uparrow\downarrow_{\mathrm{R}}}dx\right) \\
V &= e\left(\frac{\rho_{\mathrm{H}}\rho_{\mathrm{R}}}{(\rho_{\mathrm{H}}l_{\mathrm{R}}+\rho_{\mathrm{R}}l_{\mathrm{H}})}\right) y \left(D_{\mathrm{H}}\theta_{\mathrm{ISHE_H}}\rho^{*}\Delta\bar{\mu}_{\uparrow\downarrow_{\mathrm{H}}}\Big|_{-l_{\mathrm{H}}}^{0} + D_{\mathrm{R}}\theta_{\mathrm{ISHE_R}}\rho^{*}\Delta\bar{\mu}_{\uparrow\downarrow_{\mathrm{R}}}\Big|_{0}^{l_{\mathrm{R}}}\right)
\end{aligned}
\tag{2.9}
$$

which can be written in its final form of:

$$
\begin{aligned}
V = e\left(\frac{\rho_{\mathrm{H}}\rho_{\mathrm{R}}y}{(\rho_{\mathrm{H}}l_{\mathrm{R}}+\rho_{\mathrm{R}}l_{\mathrm{H}})}\right)\left(\frac{\left(R_{\mathrm{R}}\tau_{\uparrow\downarrow_{\mathrm{H}}}-R_{\mathrm{H}}\tau_{\uparrow\downarrow_{\mathrm{R}}}\right)D_{\mathrm{H}}D_{\mathrm{R}}}{\left(D_{\mathrm{R}}\lambda_{\mathrm{H}}\coth\left(\frac{l_{\mathrm{H}}}{\lambda_{\mathrm{H}}}\right)+D_{\mathrm{H}}\lambda_{\mathrm{R}}\coth\left(\frac{l_{\mathrm{R}}}{\lambda_{\mathrm{R}}}\right)\right)}\right)\times\dots \\
\left(\frac{\lambda_{\mathrm{R}}\theta_{\mathrm{ISHE_R}}\left\{\cosh\left(\frac{l_{\mathrm{R}}}{\lambda_{\mathrm{R}}}\right)-1\right\}}{\sinh\left(\frac{l_{\mathrm{R}}}{\lambda_{\mathrm{R}}}\right)}+\frac{\lambda_{\mathrm{H}}\theta_{\mathrm{ISHE_H}}\left\{\cosh\left(\frac{l_{\mathrm{H}}}{\lambda_{\mathrm{H}}}\right)-1\right\}}{\sinh\left(\frac{l_{\mathrm{H}}}{\lambda_{\mathrm{H}}}\right)}\right)
\end{aligned}
\tag{2.10}
$$

2.4.7 Numerical simulations

Using Equations 2.8 and 2.7, Equation 2.10 can be solved when the following parameters are specified: The resistivity of the Host and Relaxer ρ_{H} and ρ_{R}, the sample dimensions y and l, the excitation rate R, the temperature T, the ISHE angle θ_{ISHE},

and the spin diffusion length λ. Values for most of these parameters are defined by the experiment or can found in the literature (which will be discussed below), however, the value of R must be calculated.

An estimation of R (the number of spin-flips per second per unit volume) was made by dividing the number of electrons within a Zeeman energy of the Fermi surface by the spin-flip relaxation time. This gives an approximation of the number of spin-flips per second required to maintain a large $\rho^* \Delta\bar{\mu}_{\uparrow\downarrow}$. The number of active spins was approximated using $g(E_\mathrm{F}) \times \mu_\mathrm{B} B$ where the density of states at the Fermi surface is calculated as $g(E_\mathrm{F}) = \frac{3n}{2E_\mathrm{F}}$ with $E_\mathrm{F} = \frac{\hbar^2}{2m}(3\pi^2 n)^{\frac{2}{3}}$ (using the model of a 3D electron gas). Using $n = 10^{29}\,\mathrm{m}^{-3}$, $B = 0.6\,\mathrm{T}$, $T = 300\,\mathrm{K}$, $\rho = 1.59 \times 10^{-8}\,\Omega\mathrm{m}$ [40] and $\lambda = 700\,\mathrm{nm}$ [38], the calculated value of R is $1.2 \times 10^{32}\,\mathrm{s}^{-1}\mathrm{m}^{-3}$.

Skin depth

Equation 2.4 can be solved analytically to provide an ISHE voltage given by Equation 2.10, however this solution ignores the effect of microwave skin depth. For silver, at 10 GHz the skin depth is of the order $\delta = 600\,\mathrm{nm}$, which is on the same order of magnitude as the spin diffusion length, which means that the decay in microwave penetration is unlikely to be negligible in systems of this size. The effects of the skin depth can be added to Equation 2.4 by multiplying the excitation term R by an exponential decay of $\exp^{\frac{-x-|l_\mathrm{H}|}{2\delta}}$. Adding this term makes the solution messy so it is not recorded here, however, as the equations can be solved numerically on a computer, this term will be included for the simulations performed below. It is worth noting that the exponential decay does not greatly affect the peak output voltage, changing its value by less than a factor of 2.

Input parameters

To proceed with the numerical simulations, values must be assigned to the key parameters. The Host is chosen to be silver, and the Relaxer is chosen to be platinum. The values $y = 10\,\mathrm{mm}$, $l_\mathrm{R} = \lambda_\mathrm{R}$, $R = 1.2 \times 10^{32}\,\mathrm{s}^{-1}\mathrm{m}^{-3}$, $T = 300\,\mathrm{K}$,

$\rho_{\mathrm{Ag}} = 1.59 \times 10^{-8}\,\Omega\mathrm{m}$ [40], $\rho_{\mathrm{Pt}} = 1.06 \times 10^{-7}\,\Omega\mathrm{m}$, and $\delta_{\mathrm{Ag}} = \sqrt{\frac{\rho}{\pi f \mu_{\mathrm{r}}\mu_0}} = 633\,\mathrm{nm}$ where $f = 10\,\mathrm{GHz}$ are used. l_{H} is allowed to vary. This leaves θ_{ISHE} and λ still to specify.

There is debate in the literature as to the 'correct' values of these parameters. Wang [38] claims that $\lambda_{\mathrm{Ag}} = 700\,\mathrm{nm}$, $\lambda_{\mathrm{Pt}} = 7.3\,\mathrm{nm}$, $\theta_{\mathrm{ISHE}\mathrm{Ag}} = 0.0068 \pm 0.0007$ and $\theta_{\mathrm{ISHE}\mathrm{Pt}} = 0.10 \pm 0.01$, whereas Bass [37] records values of $\lambda_{\mathrm{Ag}} = 132 - 152\,\mathrm{nm}$ at room temperature. Hoffmann [39] presents measurements of $\theta_{\mathrm{ISHE}\mathrm{Pt}}$ that range between 0.11 and 0.01. As the model has been simulated on a computer, it is possible to investigate the effect that varying these parameters has on the system. This will be explored below.

Sensitivity to perturbations

By looking at Equation 2.10, it is possible to predict which parameters will be most sensitive to perturbation. In the last bracket of Equation 2.10, it is noted that $\frac{\{\cosh(x)-1\}}{\sinh(x)}$ varies between 0.24 and 1 as x increases from 0.5 to infinity. This means that, so long as $l \simeq \lambda$, this term can be approximated as a numerical factor, and the bracket can be broadly simplified to $(\lambda_{\mathrm{H}}\theta_{\mathrm{ISHE}^{\mathrm{H}}} + \lambda_{\mathrm{R}}\theta_{\mathrm{ISHE}^{\mathrm{R}}})$. As this is the only term containing θ_{ISHE}, by looking at the relative sizes of $\lambda\theta_{\mathrm{ISHE}}$ for the two materials, it is possible to determine which material will contribute the most to V_{ISHE}. For silver and platinum, $\lambda\theta_{\mathrm{ISHE}} = 4.76\,\mathrm{nm}$ and $0.73\,\mathrm{nm}$ respectively (using $\lambda_{\mathrm{Ag}} = 700\,\mathrm{nm}$, $\lambda_{\mathrm{Pt}} = 7.3\,\mathrm{nm}$, $\theta_{\mathrm{ISHE}\mathrm{Ag}} = 0.0068$ and $\theta_{\mathrm{ISHE}\mathrm{Pt}} = 0.10$) indicating that the silver is the dominant generator of spin current.

Equation 2.10 is linear with respect to y, R, and θ_{ISHE}, so fluctuations in these values should only lead to linear fluctuations in V_{ISHE}. Fluctuations in ρ, l, and λ, however, will lead to a more complex response. As the values of ρ reported in the literature are in generally good agreement for both silver and platinum, the interaction between l and λ is of primary interest and is explored below.

Data Plots

By plotting the ISHE voltage with respect to the ratio $l_{\mathrm{H}}/\lambda_{\mathrm{H}}$ and observing the maxima, it is possible to determine the optimal thickness of the Host film (with respect to its spin diffusion length). This will enable the investigation into whether it is better to have a thick film which can generate lots of spin current, but short out the ISHE voltage generated, or a thin film that does not produce as much spin current, but is able to maintain a greater voltage across itself. Plots of this type can be made for various λ_{H}, which will provide insight into the interaction between λ and ρ. These are presented in Figure 2.7.

Figure 2.7 plots V_{ISHE} against $l_{\mathrm{H}}/\lambda_{\mathrm{H}}$ for various values of λ_{Ag}, using $\lambda_{\mathrm{Pt}} = 7.3\,\mathrm{nm}$, $\theta_{\mathrm{ISHE\,Ag}} = 0.0068$ and $\theta_{\mathrm{ISHE\,Pt}} = 0.10$, in addition to the parameters stated above. For most of the traces, the optimal thickness of λ_{Ag} is close to one, and when it is not, the voltage generated for a ratio of one is within a numerical factor of the maximum voltage. This suggests that aiming to match the thickness of the film to λ is worthwhile, however, failure to do so is not critical to the output signal.

Using this model, it is predicted that it should be possible to create an Overhauser Spin Battery device out of a silver/platinum bilayer with an output voltage of $\approx 5\,\mu\mathrm{V}$. The host metal should have a thickness on the order of its spin-flip relaxation length in order to maximize the spin current generated, and the sample should be as large as possible to maximize the ISHE voltage.

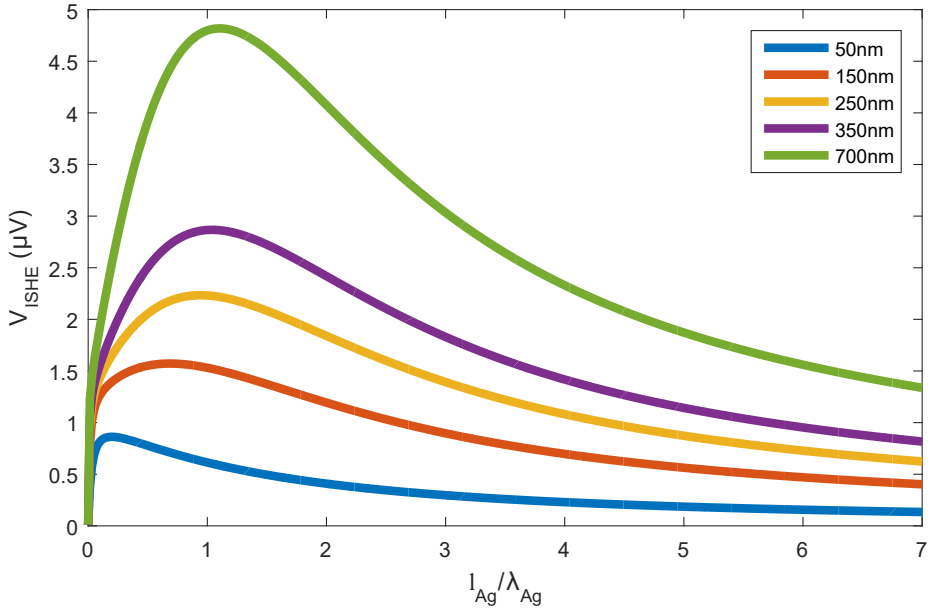


Figure 2.7: Plot of the dependence of the Spin Battery's inverse spin Hall voltage on the thickness of the silver with respect to the silver's spin diffusion length ($l_{Ag}/\lambda_{\mathrm{Ag}}$) for various values of λ_{Ag} (labelled in the legend). For $\lambda_{\mathrm{Ag}} = 700\,\mathrm{nm}$, the maximum V_{ISHE} of $4.81\,\mu\mathrm{V}$ is obtained with $l_{\mathrm{Ag}}/\lambda_{\mathrm{Ag}} = 1.103$ which gives a thickness of $l_{\mathrm{Ag}} = 772\,\mathrm{nm}$.

Chapter 3

The Spin Battery: Experiments

3.1 General laboratory experimental methods

In this chapter, details are provided of some of the experimental techniques and apparatus used for our Spin Battery experiments. This covers sample fabrication, experimental design and construction, and output measurement methods. Some of the techniques used are already well established, but are outlined here for convenience.

3.1.1 Fabrication techniques

System requirements

Most of the thin-films used in the experiments were grown in-house in the author's group's thin-film production facility, which was repaired, upgraded, and rendered operational over the course of this thesis. This was a necessary step, as it allowed for greater flexibility and control of the thin-film production process than that which could be afforded by a commercial grower.

Most of the Spin Battery experiments were performed on thin metallic films, which were predominantly arranged in a bilayer format. Cleanliness at the interface between the two layers has previously been highlighted as an important factor in device efficiency [41], so it was therefore desirable to be able to produce all of the

necessary thin films on the sample without breaking vacuum. Fulfilling this requirement was one of the main reasons that the thin-film facility needed upgrading.

The second requirement of the system was that it was to be able to produce thin-films by both evaporation and sputtering methods. This would allow for maximum flexibility in terms of which materials could be deposited.

The final requirement was again to do with cleanliness, but this time of the substrate. The samples used were grown on (Thermo scientific) glass microscope slide substrates, which had been pre-cleaned using 'Decon 75' solution. Previous laboratory work [15] has shown greater success with film growth if the substrate is also pre-sputtered. Despite using the same electronics outside of the vacuum chamber, pre-sputtering requires a different internal arrangement to sputter deposition, and therefore, the system design needed to allow for this.

The vacuum system

The basic vacuum system comprises the vacuum pumps, the pressure gauges, and the two vacuum chambers, separated by a pneumatically-driven gate.

The larger 'main chamber' is the one in which thin-films are made via sputtering and evaporation, whereas the smaller 'load lock' chamber is used for pre-sputtering and storing samples under vacuum while the evaporation boats are refilled. Both chambers have their own independent pumping and monitoring systems, such that the pressures can be equalized between them before the gate is opened. The main chamber also has a small leak-valve attached, which is connected to a tank of argon gas. This allows for the careful insertion of the gas, which is important during the sputtering process.

The pumps Both chambers are evacuated using a rotary backed turbo pump. The load lock was pumped by a Leybold Turbovac 360 turbo pump, which was backed by a Leybold Trivac D25B rotary pump, and the main chamber was pumped by a Leybold Turbovac 600C turbo pump, backed by a Leybold Trivac S40B rotary pump. Isolation valves were installed between the rotary and turbo pumps for both

lines, so that it is possible to vent the rotary pumps when the system is turned off. To avoid damage, the turbo pumps must only be turned on when their water cooling system is active and the pressure of the chamber is already below 10^{-1} mbar.

A butterfly valve was installed between the turbo pump and the vacuum chamber for the main chamber only. This is an important element of the system when it comes to sputtering, as by carefully controlling the rate of evacuation while also controlling the rate of gaseous influx using the aforementioned leak-valve, it is possible to control the pressure of the chamber precisely.

Pressure gauges The pressure of the two chambers was monitored using several pressure gauges, which operate over various regimes. The Edwards Pirani PR10-K operates from atmosphere down to 10^{-2} mbar and was used on the load lock. The Edwards Penning CP25-K operates from 10^{-2} mbar down to 10^{-7} mbar and was used on both chambers. The Leybold Thermovac TM20 and TR211 sensor operates from atmosphere down to 10^{-3} mbar and takes the place of the Pirani for the main chamber.

The Pirani gauge and the Thermovac gauge operate by measuring the electrical properties of a heated filament, which loses heat at a rate that depends on the pressure of the gas being measured [42]. The Penning gauge however, uses a high voltage (kV) between a cold cathode/anode pair to measure the resistance of the gas. When a gas ion strikes the cathode, electrons are emitted which are drawn towards the anode. A magnetic field is applied so that the electrons travel in a spiral trajectory, which increases the likelihood of a collision in which the electron ionises further gas atoms, and hence extends the gauge operating range to lower pressures. The current measured between the two electrodes is related to the pressure of the gas [43].

Sample manipulation

As the film fabrication and sample preparation devices are located in different regions of the vacuum chamber, it was necessary to develop a method for manipulating and

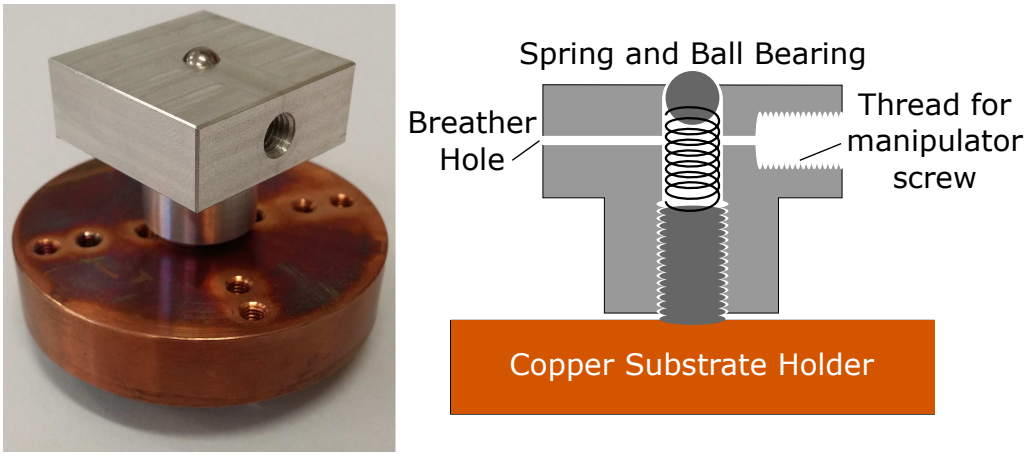


Figure 3.1: The 'mushroom' substrate manipulator. The sprung ball bearing can hold the 'mushroom' in place when it is inserted into the 'mushroom holder' by engaging with the hex socket of the screw which mounts the 'mushroom holder' onto the sample table or sample storage rack. It can be easily removed again with the application of gentle force.

moving samples around the inside of the vacuum chamber while remaining under vacuum.

The solution that was implemented involved adding to the simple solid copper substrate holders a custom-made attachment which was named the 'mushroom'. These 'mushrooms' are able to slide and lock into machined 'mushroom holders', which were attached to both a storage rack in the load lock, and a substrate table suspended in the main chamber. The schematics of these parts, and a diagram of the system are presented in Figures 3.1, 3.2, and 3.3.

The 'mushrooms' can be moved between the 'mushroom holders' in the main chamber and those in the load lock using the manipulator arm. This is simply a long rod, which is at one end magnetically coupled to a handle outside the chamber, and has a threaded protrusion at the other. This thread can be screwed into a hole tapped in the 'mushroom', allowing the manipulator arm to pick up and release the 'mushroom' as required. The arm is therefore able to enter the main chamber, retrieve the substrate holder, and deposit it in the storage rack before the load lock gate is shut. By doing this, it is possible to keep the sample in a low pressure environment while the main chamber is opened (which is a necessary step when refilling the evaporation boats).

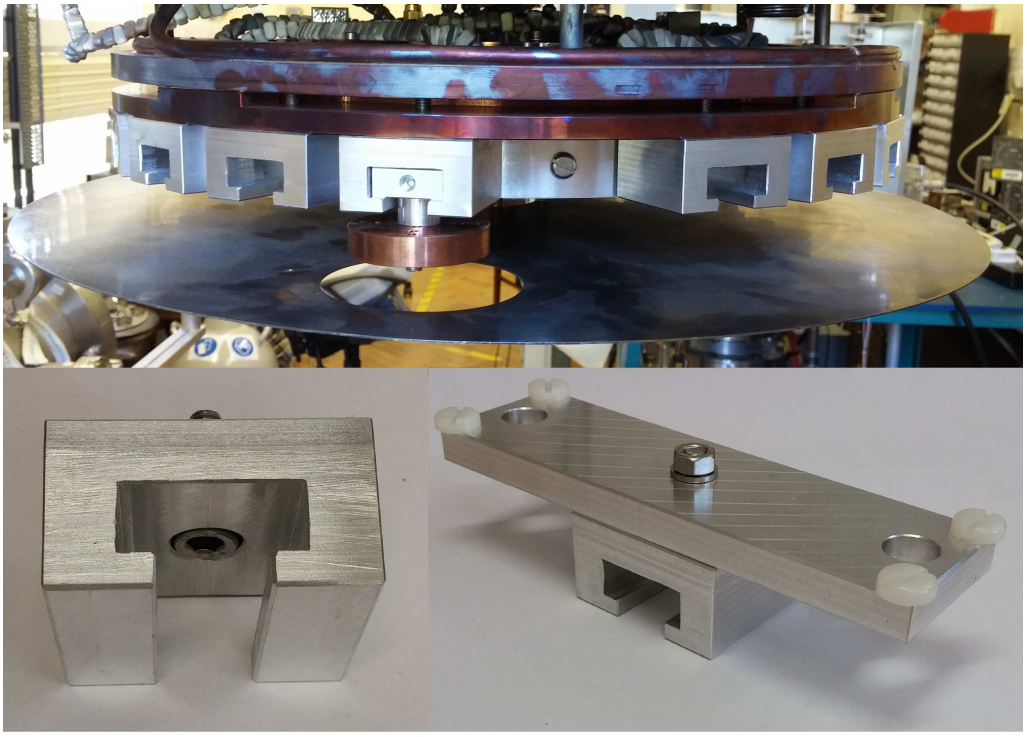


Figure 3.2: Bottom: A 'Mushroom holder' (left), and a single rung of the substrate storage rack (right). Top: The substrate table with a loaded 'mushroom' above the hole in the shield.

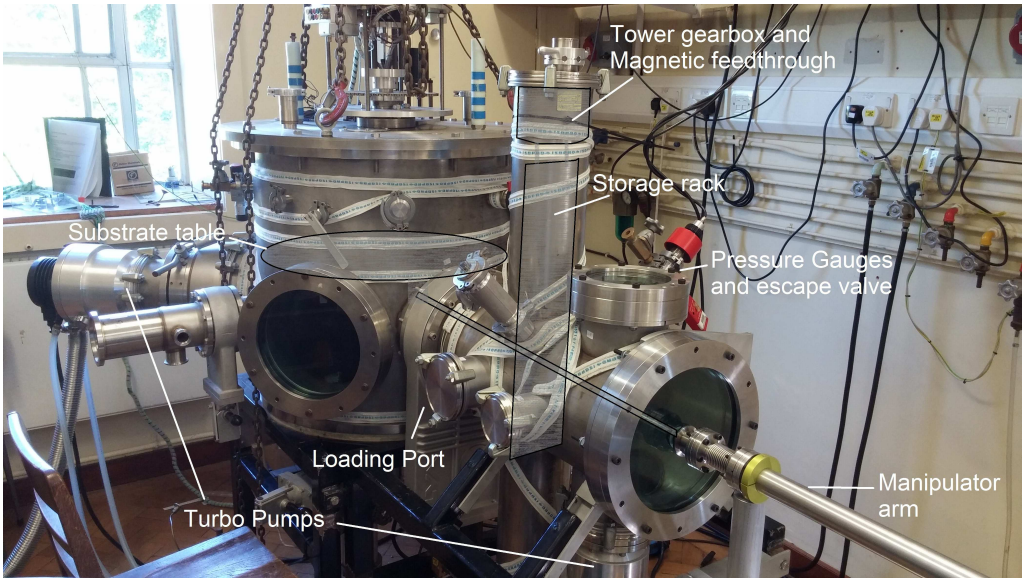


Figure 3.3: The vacuum chamber, with annotations showing the location of some of the key components. The 'main chamber' contains the substrate table, and can be isolated from the 'load lock' (which contains the storage rack) by using the pneumatic gate between them.

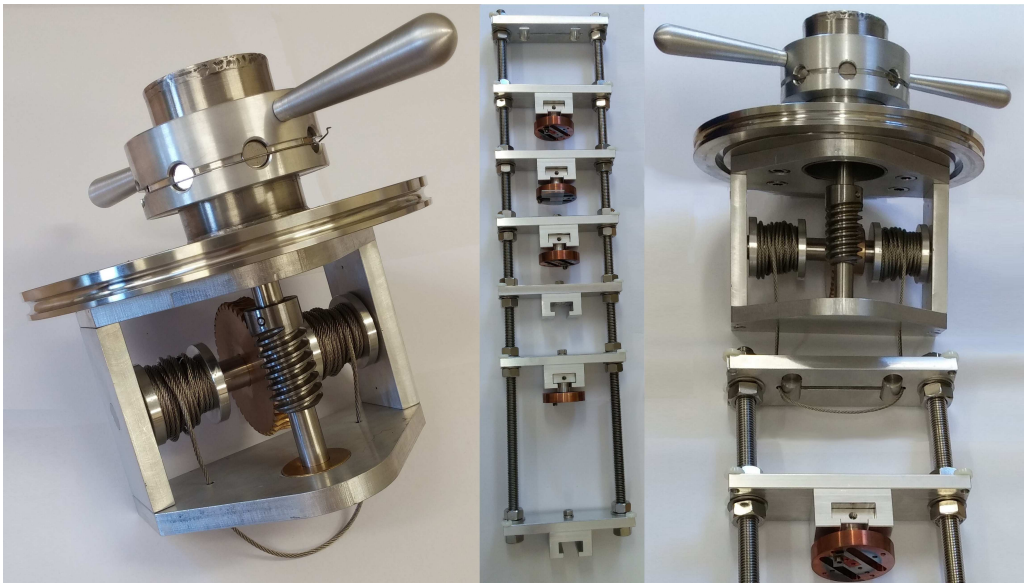


Figure 3.4: The storage rack, and the gearbox used to raise and lower it. The gearbox can be driven by the handle, which is magnetically connected to the crankshaft via two sets of magnets in an octopole arrangement.

Originally, the storage rack was designed to hold several different samples simultaneously, and was built to be able to move vertically. This functionality has since been removed, as a modification that required fixing the storage rack in place to allow for film pre-sputtering has been made. The nature of and reasoning behind this modification will be covered in §3.1.1, but it is noted here that it is easily reversible. The method by which the storage rack is raised and lowered is shown in Figure 3.4. The magnetic octopole in the handle is coupled to a similar octopole inside the tube, which in turn is connected to the worm gear in the gearbox. Turning the handle can therefore unwind the cable, allowing the storage rack to move down under gravity.

Sputtering and pre-sputtering

Sputtering is a process by which a target is eroded by the bombardment of high energy ions [44]. It can be achieved in the laboratory by using microwave techniques to generate a plasma in the vicinity of the water-cooled target at low pressures. When ions in the plasma strike the target, atoms of the target material are removed, and drift away. If these land on the nearby substrate, a thin film forms.

Pre-sputtering is a process that works in exactly the same way, except the target

is not the metal that needs to be deposited, but is in fact the substrate itself. The bombardment of plasma ions instead cleans the surface of the substrate.

The plasmas used for sputtering are created by a device called a magnetron. The key elements of the magnetron are the target, made of the material that is to be deposited, and the ring of permanent (NdFeB) magnets hidden beneath, which creates a toroidal magnetic field above the target. The magnetron is electrically isolated from the vacuum chamber, and is positioned near the substrate. Microwaves are applied to the magnetron (An AE RFX-600 was used to generate microwaves of 13.56 MHz at around 30 W), which excites the low-density gas (argon gas at a pressure of 10 μbar) into its plasma state. The plasma is confined by the magnetic field, which allows the plasma to sputter the target material more efficiently.

To pre-sputter a substrate, the substrate takes the place of the magnetron, and it is to the substrate that the microwaves are now applied. Again, the substrate must be electrically isolated from the rest of the chamber, otherwise the microwaves short to ground. As the manipulation system built to transport samples around the chamber was grounded in several places, it was necessary to make the modifications to the storage rack mentioned in §3.1.1.

One of the storage rack rungs was altered, such that the 'mushroom holder' was isolated from the aluminium rung itself. A copper wire was attached between the 'mushroom holder' and an electric feed-through in the chamber wall. This allowed for microwaves to be applied to the 'mushroom holder' and thus to the 'mushroom' and substrate without shorting to ground. A large button magnet was placed on top of the rung below the modified rung to assist with confining the plasma to the substrate. The addition of the connecting wire between the chamber wall and the storage rack is the feature which restricts the rack's vertical movement. If it were removed, the option of vertical travel would be restored, but at the cost of the ability to pre-sputter.

Thermal evaporation

Thermal evaporation can be used to produce thin films by passing a large current through a tungsten evaporation boat containing the material to be deposited. The Ohmic heating of the boat leads to temperatures which can melt and evaporate the deposition material. This method is known as 'resistive evaporation'.

The system that was constructed for resistive evaporation is driven by two transformers. The first is a 2 kW variac (variable autotransformer), whose mains voltage input is isolated by a soft-start device, designed to avoid the voltage spike generated on activation upsetting the mains. Its output is connected to the second transformer, which is a hand wound 25:1 step-down transformer (196 turns of 30 A wire, 8 turns of 300 A wire). During the evaporation process, this combination can produce currents on the order of 200 A at 6 V. This is the highest value that has been experimentally recorded before the evaporation boat itself melted, breaking the circuit. When this occurred however, the variac was only at 25% of its maximum output so higher currents may be achievable.

The output of the second transformer is connected to two large water-cooled copper bolts which protrude into the vacuum chamber. Each of these bolts has a copper clamp at its end. A thin strip of tungsten metal ($40\,\text{mm} \times 10\,\text{mm} \times 30\,\mu\text{m}$) is suspended between the clamps, completing the circuit, and acts as the evaporation boat. Carefully weighed amounts of deposition material are placed on the tungsten strip, and, once the chamber has been pumped to a low pressure (usually around 10^{-6} mbar), are completely evaporated by the applied current. The metal vapour travels from the evaporation boat to the nearby substrate, where it then condenses into a thin film.

An important additional step before the material is evaporated is to preheat the deposition material using a low applied current. This is done while the substrate is shielded, and allows for any contaminants on the metal to be burned off before the film is deposited.

Calibration

Before either deposition method can be usefully used, the system must be calibrated. This was achieved using a quartz crystal monitor. Sauerbrey discovered that the oscillation frequency of a thin piezoelectric crystal is dependent on the mass of the material deposited upon it [45]. By measuring how this characteristic frequency changes from before to after the deposition, the thickness of the deposited film can be calculated. The governing equation for this is

$$\Delta f = -\frac{2f_0^2}{A\sqrt{\rho_\mathrm{q}\mu_\mathrm{q}}}\Delta m = \frac{2f_0^2}{\sqrt{\rho_\mathrm{q}\mu_\mathrm{q}}}\rho_\mathrm{metal}\Delta t$$

where f_0 is the resonance frequency, Δf is the frequency change, A is the area of the quartz crystal, ρ_q is the density of quartz, μ_q is the shear modulus of the quartz, and Δm is the change of mass on the quartz crystal surface. ρ_metal is the density of the deposited metal, and Δt is the thickness of the film deposited. This can be arranged into a useful form for specific materials by collecting the constants together

$$\Delta t(\,\mathrm{m}) = \frac{\Delta f(\,\mathrm{MHz})}{f_0^2(\,\mathrm{MHz})C_i}.$$

The constants of some elements used are: $C_\mathrm{Ni} = 2013.208$, $C_\mathrm{Pt} = 4856.330$, and $C_\mathrm{Cu} = 2028.809$.

Depositions were calibrated by placing the quartz monitor in the same position that the substrate would normally occupy. Frequency readings at a given pressure were taken before the deposition, and again some time after the deposition, allowing for the thickness to be calculated. The time delay was necessary to allow for the crystal to cool down, as thermal variations distort the frequency measurement. In the case of the sputtering, the duration, power, and pressure were recorded for each calibration deposition so that the same conditions could be repeated for deposition onto the substrate. For resistive thermal evaporation, several test charges were used to calculate the relationship between the mass of the initial charge and the thickness

of the final film. By making these measurements, it is then possible to produce films with known thicknesses by using the correct mass in the evaporation charge.

3.1.2 How-to guide

In this section, the process by which samples were grown in the author's laboratory is described in detail. Details pertaining to the specific apparatus are included in order to assist any future students who may need to use the thin-film fabrication facility.

Preparation

Substrates (such as Thermo Scientific glass microscope slides) were prepared for thin-film deposition by first bathing them in a 1:20 dilution of Decon 75 surface cleaning solution. Samples were then bathed in clean water to remove any residual cleaning fluid, before being dried by paper towel. Care was taken here to ensure no lint or dust remained on the substrate.

Substrates were then mounted on the copper substrate holder, which was then installed into the pre-sputtering rung of the sample storage rack within the load lock chamber via the side loading port. The electrical feedthrough which connects to the pre-sputtering rung should have been identified at this point, and the button magnet used to localise the plasma should have also been put in place.

The main chamber was prepared by loading an appropriately weighed amount of a material onto the tungsten strip evaporation boat if resistive evaporation was to be used. (For the NiPt bilayer created for the Spin Battery experiments, 2.9 mg of Ni and 1.7 mg of Pt were used to produce films 40 nm and 10 nm thick respectively). If sputtering was to be used, the appropriate target must have been installed onto the magnetron. Once this was done, both chambers were sealed. The dividing gate must have been open at this point.

Pre-sputtering

It was then possible to begin evacuating the chamber using the roughing (rotary) pumps. Once the pressure reached 10^{-1} mbar, the cooling water for the turbo pumps was turned on, followed by the main chamber turbo pump. When the pressure dropped to 10^{-5} mbar, the butterfly valve was closed, and the valve to the load lock pump was shut. Using the leak valve, argon gas was inserted into the chamber. The butterfly valve was opened slightly, and the leak valve adjusted such that the pressure of the argon gas stabilized to around 25 µbar.

The radio frequency source was then connected to the matching network, which was in turn connected to the electrical feed-through leading to the pre-sputtering rung of the storage rack. A 13.56 MHz 30 W signal was applied to the matching network. The matching network was adjusted until the reflected power was minimized, and a plasma was struck. The RF power could then have been increased if it were desirable. The pressure was adjusted to around 10 µbar, and a timer was started. The NiPt sample was pre-sputtered for 5 minutes with 30 W of microwaves at 10 µbar. After the pre-sputtering was finished, the microwaves were turned off, the leak valve was shut, and the butterfly valve was reopened.

Sample transfer

The sample was then transferred into the main chamber. The manipulator arm was screwed into the 'mushroom', while care was taken not to accidentally poke the mushroom out of the mushroom holder prematurely. Once a good connection had been made, the substrate holder was slid into the main chamber. The storage rack can be raised and lowered to assist in vertically aligning the mushroom at the end of the arm with the mushroom holder within the main chamber. Once the sample was secure on the substrate table in the main chamber, the arm was unscrewed and retracted. The pneumatic door was then shut. The substrate table was then rotated by hand using the control gear on top of the chamber until the sample was located above the relevant deposition device. The coloured wheel on top of the chamber was

used to assist in aligning the sample with the magnetron or evaporation boats.

Sputtering

Sputtering was performed in a similar manner to the pre-sputtering above. The magnetron was connected to the output of the matching network, and the magnetron cooling water was turned on. A plasma was struck using the same method as above. The thickness of the film produced was dependant on the RF power (which usually ranged between 50 to 100 W), duration of deposition, and pressure in the chamber (usually between 4 and 15 μbar). This was previously calibrated by performing a short deposition onto a quartz monitor, as described in §3.1.1.

Resistive evaporation

Evaporation was performed by first turning on the cooling water for the evaporation boats. The soft-start device was plugged in and turned on, while the variac transformer was set to 0. The evaporation shield was moved in between the sample and the boat, and the pressure of the chamber was reduced to below 10^{-5} mbar before current was applied to the boat. Sufficient current was applied to bring the boat and evaporation load to a cherry-red colour for 10 s before returning to zero current. This 'pre-cook' ensured that there were no contaminants on the evaporation charge or boat that would disrupt the growth of the film.

After the pre-cook, the shield was rotated to expose the substrate to the evaporation boat. The variac was used to increase the current until the evaporation charge evaporates away. This occurred around 150 V. Care was taken to avoid melting the evaporation boat, as this would contaminate the sample, as well as necessitate fitting a replacement boat.

After deposition

Having grown the first layer, the pressure of both chambers was returned to around 10^{-1} mbar, and the pneumatic gate was opened. The substrate table was rotated

such that the manipulator arm was able to screw into the mushroom. The sample was then moved from the main chamber to the storage rack in the loading lock. The gate was shut, and the main chamber pumps were deactivated. The main chamber was then brought up to atmospheric pressure so that the next evaporation charge could be loaded. Once the system was again pumped down (caution: ensure that an active turbo pump never sees a pressure higher than 1 mbar!), the substrate was transferred to the main chamber, and subsequent depositions were performed as above. Once all depositions were complete, the sample was removed from either the main chamber via a side port, or by opening the lid.

3.1.3 Experimental techniques

All of the experiments in this section have the same basic physics at their core: magnetic resonance. Whether it be ferromagnetic resonance (FMR) or electron spin resonance (ESR), the experimental arrangements are nearly identical. Before describing the full experimental setup, it is noted that the signals generated from these experiments can be very small, and difficult to detect. One method of detection, and indeed the one used here, is phase sensitive detection using a lock-in amplifier, described below.

Lock-in amplifier

The lock-in amplifier is a device designed to pick out a tiny signal from a lot of background noise by shifting the desired signal (and only the desired signal) to DC, and then applying heavy filtering to remove all of the other frequency components. This is achieved via a combination of signal modulation and multiplication ('heterodyning' - see §5.2.3).

To use a lock-in amplifier, a characteristic of the experiment must be modulated in such a way that the output of the experiment is also modulated at the same, known frequency. One example would be modulating the magnetic field applied to a sample when the resonance condition was met. This would then have the effect of

moving on and off resonance, which would appear similar to turning the sample 'on and off'. This oscillation would appear in the output measurement at the modulation frequency, which can be detected by the lock-in amplifier.

Now that the output signal is oscillating at the modulation frequency, the entire input to the lock-in amplifier (which is the entire output from the experiment) is multiplied by a sinusoidal wave of the same, known frequency. For consistency across this thesis, this frequency will be referred to as ω_{Probe}. Multiplying two cosines together leads to two different cosines whose frequencies are the sum and difference of the original two. Applying this to a general input signal (which contains an arbitrary number of signals of different phases, frequencies, and amplitudes) allows the output of the lock-in amplifier to be written as:

$$\begin{aligned} &\sum \left\{ A_i \cos\left(\omega_i t + \phi_i\right) \right\} \times B \cos\left(\omega_{\text{Probe}} t\right) = \\ =&\sum \left\{ \frac{1}{2} A_i B \left(\cos\left(\left(\omega_i - \omega_{\text{Probe}}\right) t + \phi_i \right) + \cos\left(\left(\omega_i + \omega_{\text{Probe}}\right) t + \phi_i \right) \right) \right\} \end{aligned} \tag{3.1}$$

As the probe frequency matches that of the modulation applied to the sample, the desired, modulated signal now appears as a DC term. It is also noted that the frequencies of the $\frac{1}{f}$ background noise that previously obscured the desired signal have been shifted to cluster around ω_{Probe}. By applying a strong low-pass filter after the multiplication process, the modulated signal should become the dominant signal in the result, as the higher frequency terms (including most of the noise!) will be filtered out. It is by this method that the lock-in amplifier is able to pick out an experimental signal at a known frequency even if there are relatively high background noise levels.

Time constants: theory The simplest type of low-pass filter that can be used after the multiplication stage of the lock-in process is an RC filter consisting of a resistor and a capacitor in a voltage divider arrangement (with the capacitor going

to ground). The equation governing the voltage throughput of the filter is

$$V_{\text{out}} = V_{\text{in}} \frac{1}{1 + j\omega RC} = V_{\text{in}} \frac{1 - j\omega RC}{1 + (\omega RC)^2}, \tag{3.2}$$

and the (rise) time response takes the form

$$V(t) = V_0 \left(1 - \exp^{-\frac{t}{RC}}\right). \tag{3.3}$$

A useful parameter for characterising filters of this type is the 'time constant', which is defined as $\tau_{\text{f}} = RC$. The logic of this name can be seen by considering Equation 3.3 and noting that RC takes the place of the decay constant in the exponential term, and has units of time.

The effect of the time constant on the throughput signal is two-fold. Using Equation 3.2 to calculate $\left|\frac{V_{\text{out}}}{V_{\text{in}}}\right|$, it can be seen that signals will be attenuated by the filter by a factor of $\frac{1}{\sqrt{1+(\omega RC)^2}}$. The time constant in this case is related to the frequency above which the attenuation becomes significant (the cut-off frequency) which can be given as $f_{\text{f}} = \frac{1}{2\pi RC}$. When the time constant is increased, f_{f} decreases, and fewer non-DC components can pass through the filter without being greatly attenuated.

Although it appears that a large time constant will give the best filtering, there is a flip side to the choice of τ_{f} which is encapsulated in Equation 3.3. Here, it can be seen that a large time constant leads to a slow response time of the output signal. This means that when the desired signal is present in the input to the lock-in, the lock-in will need to wait a time on the order of τ_{f} for the capacitor to charge up before it is able detect the signal. This is an important factor to consider when choosing the rate at which one of the variables is swept in an experiment that is using a lock-in amplifier.

When choosing an appropriate time constant for an experiment, the balance between strong filtering and slow response time must be considered, especially in conjunction with the experimental sweep rate and the size of the resonance. It is

noted here that stronger filtering can be achieved by placing several *RC* filters in series. This has the effect of increasing the attenuation for a given value of τ_{f}, and is often recorded using units of dB per octave. This too has its drawbacks, as it also increases the response time of the system.

Time constants: experimental considerations In the apparatus used for the experiments (Figure 3.5), there was a significant amount of metal (in the form of the cryostat and the rhumbatron) between the sample and the coils used to modulate the magnetic field. Given that the microwave skin depth of copper or aluminium is on the order of 2 mm at 1 kHz, and on the order of $7-8$ mm at 100 Hz, it is necessary to use a low (~ 100 Hz) modulation frequency for field modulation experiments, or else risk attenuating the modulating field.

If the frequency of the modulating field is low, the modulated signal will be hidden behind a greater quantity of $\frac{1}{f}$ noise. As this noise exists as random fluctuations in the input signal, (only existing at any given frequency for a short period of time), it can be filtered out by increasing the time constant, and slowing the response of the output signal. The values of τ_{f} that were experimentally determined to sufficiently reduce the $\frac{1}{f}$ noise were either 1 s or 3 s. Taking into consideration the arguments made above, it is desirable to set the $\boldsymbol{B}$-field sweep rate such that the resonance is covered in around 30-60 s.

The ESR Setup

With the details of the detector understood, it is now possible to see how it fits in with the rest of the experiment. The arrangement is presented in Figure 3.5.

First, microwaves are generated using an HP 8672A synthesized signal generator, which are amplified up to around 30 dBm using a Miteq AMF-7B amplifier. These pass down the ESR probe into the cryostat, and into the experimental cavity. The output of the experiment leaves the cryostat before being rectified by a HP 8470B crystal detector. Once rectified, the output signal goes to the Y_1 trace of an oscilloscope, and also the input of the lock-in detector.

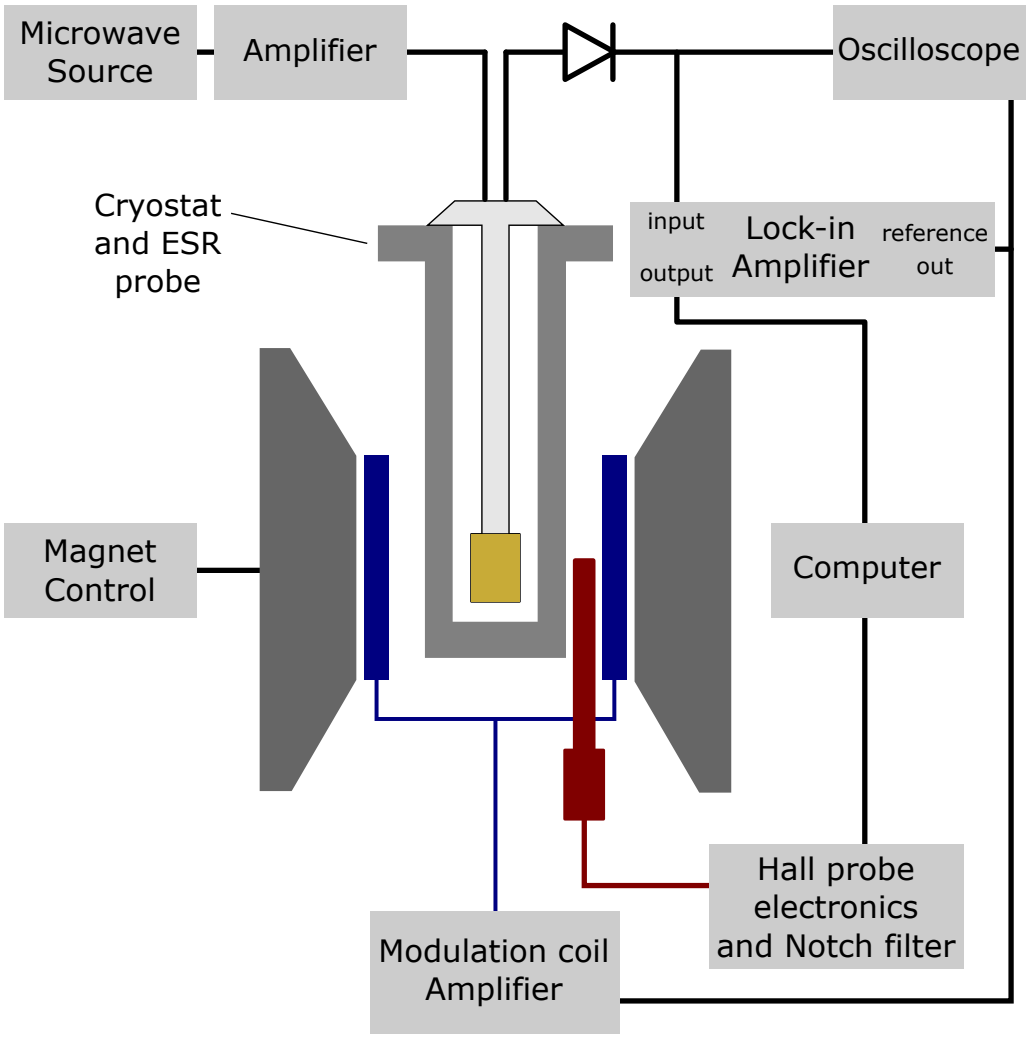


Figure 3.5: A schematic diagram of the ESR Setup, showing the arrangement of the large electromagnets, the modulation coils, the Hall probe, the cryostat, and the ESR probe. A more detailed diagram of the ESR probe can be found in Figure 3.9.

Meanwhile, the reference frequency of the lock-in amplifier ω_{Probe} is amplified by an Ecko Sound RX1200 amplifier before going into the modulation coils and the Y_2 channel of the oscilloscope. The modulation coils are able to produce oscillating fields at 87.5 Hz of up to 3 mT when a 100 V voltage is applied.

The static magnetic field is applied by a Newport Instruments electromagnet capable of generating fields of up to 1 T. This magnet has a large pole face separation of around 70 mm, however it is able to deliver a fairly uniform field due to the presence of the large soft-iron cores in each of the water-cooled coils.

The magnetic field at the sample is measured by a Hall sensor. This produces a voltage that is related to the magnetic field experienced by the probe. To read the static applied magnetic field, the signal must be filtered to remove frequency components at ω_{Probe}. This is important when the applied field is being slowly swept, and the $\boldsymbol{B}$ field measurement is being used as the x-axis of a plot on the computer.

Microwave excitation of the sample

Upon entering the experimental cavity, the microwaves need to be applied to the sample being tested. In the experiments, this was done using two different methods: via microwave striplines or microwave cavities.

The Rhumbatron Microwave cavities come in many shapes and sizes. The design used for these experiments is called a 'Rhumbatron', and has some clever design features which makes it especially suited to the task at hand. The rhumbatron takes the form of a cylindrical cavity with an internal stub, and is depicted in 3.7.

The workings of the cavity can be understood by invoking the idea of a capacitor and single inductive loop (Figure 3.6a). In this situation, when the capacitor is charged, the energy is stored in the electric field between the two plates. As the capacitor discharges, the electrons flow around the loop (generating a magnetic field), until the capacitor is charged with the opposite polarity. This process oscillates back and forth, transferring the energy between electric and magnetic fields. If several

of these inductive loops are connected in parallel, the resonance frequency of the system can be greatly increased, up into the GHz regime. The limit of adding these inductive loops is a single continuum of metal, forming the outside of a toroidal rhumbatron. If the original inductive loop is instead rectangular, the continuum shape becomes a cylinder with an internal cylindrical stub, as seen in Figure 3.6b, which has the same form as the rhumbatron used in our experiments.

The unusual shape of the rhumbatron cavity has an interesting effect on the localisation of the $\boldsymbol{E}$ and $\boldsymbol{B}$ fields that appear during cavity resonance. The $\boldsymbol{E}$ field is localised at the top of the cavity, between the 'capacitive plates', whereas the $\boldsymbol{B}$ field is located predominantly at the bottom of the cavity. This separation of the $\boldsymbol{E}$ and $\boldsymbol{B}$ fields is important for resonant experiments, as for ESR, only interactions between the sample and the $\boldsymbol{B}$ field, uncontaminated by $\boldsymbol{E}$ are of interest.

The rhumbatron cavity can be excited by coupling to either the electric or magnetic field. This can be done via an electrical stub in the vicinity of the 'capacitive plates', or by a small loop near the bottom of the cavity. Electric stubs were used in our system, as the experimental samples were positioned in region where the $\boldsymbol{B}$ field is largest. Two electric stubs were installed in the top of the cavity: the first was used for microwave insertion, whereas the second was used to measure the energy in the cavity, which is related to the cavity's quality factor 'Q'.

The rhumbatron was machined out of high-purity brass, and has the dimensions shown in Figure 3.7. The purity of the brass is important, as the presence of any magnetic impurities may lead to spurious absorption signals. Two small holes were drilled in the bottom of the rhumbatron to allow thin wires to enter the cavity and be attached to the spin battery sample. This was to enable ISHE measurements.

Stripline An alternative method for microwave excitation of the sample is to use a microwave stripline. This method uses the Oersted field around a coplanar stripline to interact with the sample. The experimental setup is depicted in Figure 3.8 (as are the dimensions of the stripline). The field experienced by the sample is less than that obtainable in the rhumbatron, however, as the sample does not need to

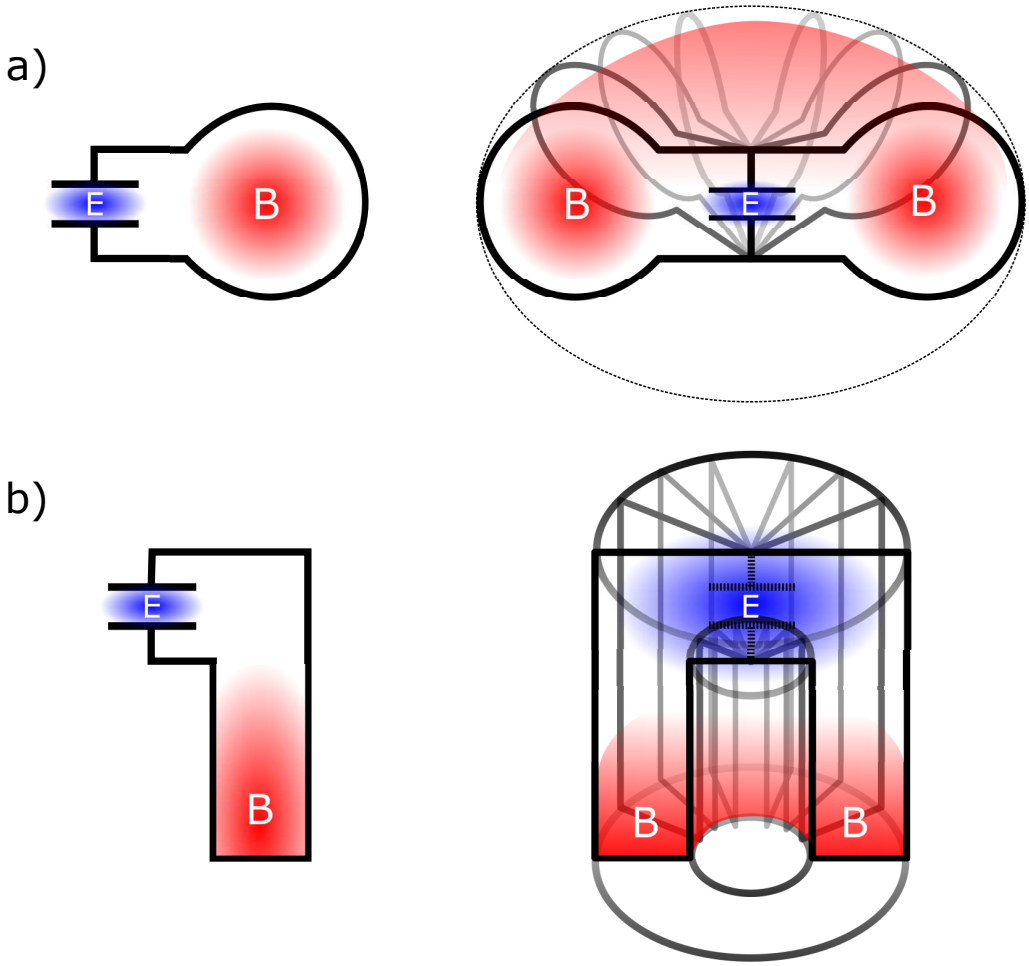


Figure 3.6: The workings of a rhumbatron cavity resonator. Stored energy oscillates between the $\boldsymbol{E}$ and $\boldsymbol{B}$ fields, the localisation of which is shown in all of the diagrams. a, left) A simple capacitor/inductive loop circuit. a,right) Several inductive loops connected to the same capacitor (now in 3D space). The many-loop limit of this case is a continuous surface, and forms the shell of a toroidal rhumbatron cavity. b,left) A different capacitor/inductive loop circuit. The $\boldsymbol{B}$ field is now predominantly located towards the bottom of the circuit. b, right) Several rectangular loops connected in the same fashion as above. The many-loop limit of this circuit is the cylindrical rhumbatron used for our experiments.

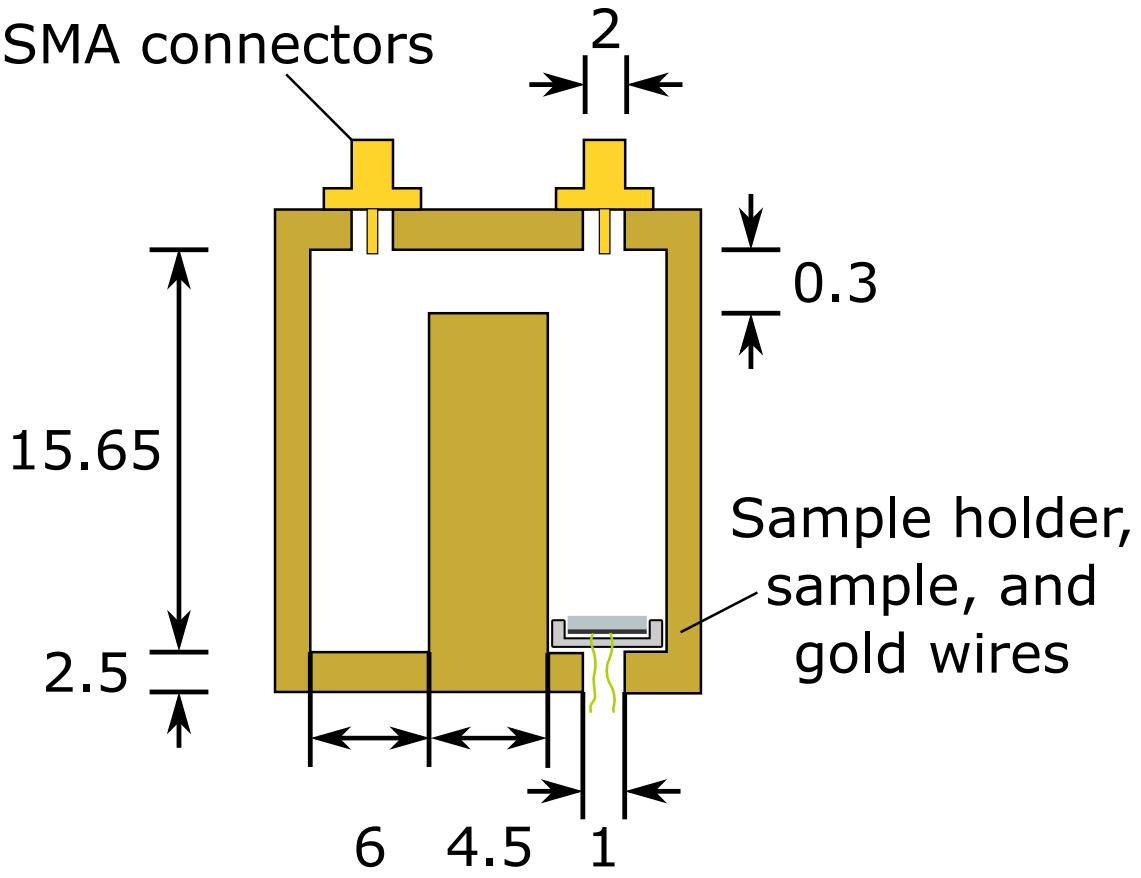


Figure 3.7: Cross-sectional diagram of the cylindrical rhumbatron cavity used in our experiments, with dimensions in mm. A detailed diagram of the sample holder can be seen in Figure 3.10.

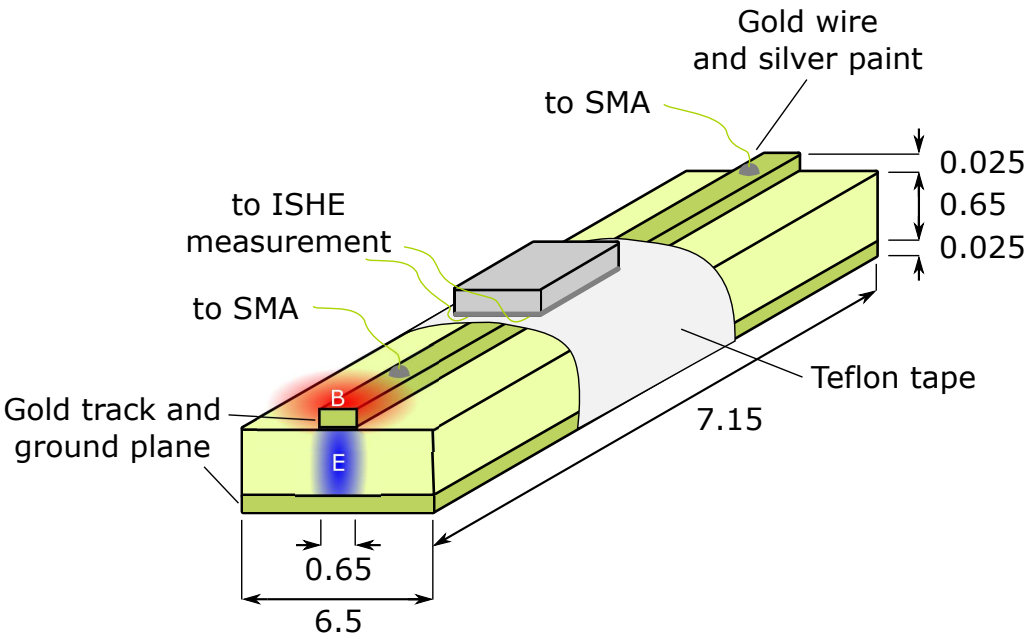


Figure 3.8: Schematic of the microwave stripline experiment, with measurements in mm. The localisation of the $\boldsymbol{E}$ and $\boldsymbol{B}$ fields are shown at one end of the stripline, but in reality extend all the way along. The main substrate of the stripline is made from ceramic.

be contained inside an enclosed cavity, it is easier to attach wires to the sample for making ISHE measurements.

Cryostat, and probe design

The cryostat used in these experiments was an Oxford Instruments variable temperature cryostat. It uses liquid helium to cool the experiment down to 4 K, and utilizes gaseous helium as a heat-exchanging gas inside the sample space. To perform the experiments in the sample space within the cryostat, while maintaining a hermetic seal at the top, it was necessary to design and construct an ESR probe for the purpose. This can be seen in Figure 3.9.

The probe originally used rigid stainless steel coaxial cable to electrically link the top and bottom of the cryostat. This was to avoid heat loss along the cables where possible. Unfortunately, the electrical loss in the cables was too large in the operational frequency range (-20 dBm each direction at 10 GHz), so the microwave cables were replaced with conventional tin-plated copper braid coaxial cable instead. Four cables travel up and down the probe: two for the microwave input and output,

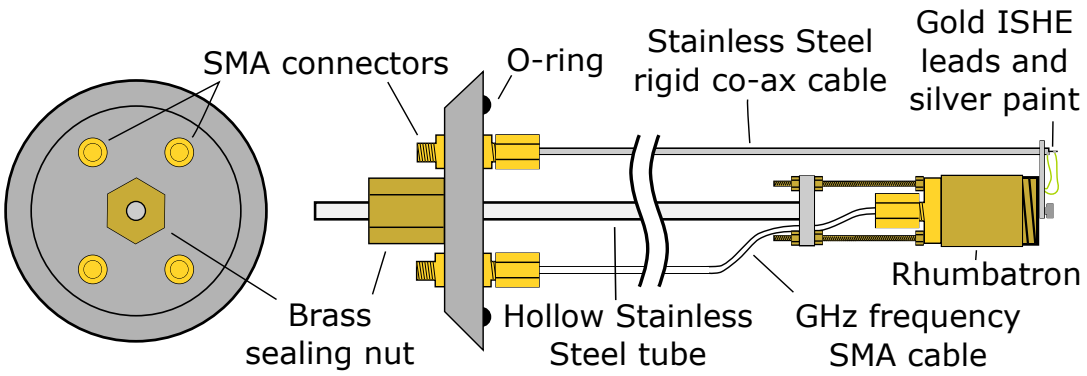


Figure 3.9: Schematic of the ESR probe in a third angle orthographic projection (not to scale). Two of the SMA connections are used to apply and extract microwaves from the rhumbatron. The other two connectors are used to enable the measurement of the ISHE signal. The brass sealing nut allows the entire probe to be raised and lowered within the cryostat, ensuring that the sample is in the correct position within the applied magnetic field.

and two for making ISHE measurements. At the bottom of the probe, it is possible to mount either the rhumbatron or the stripline, depending on the experimental requirements.

ISHE measurements

When performing ISHE measurements, it is necessary to connect two wires to the sample while it is being excited by microwaves. This is trivial when the stripline is being used (silver paint and thin gold wires can be used to connect the sample to an SMA connector), though it is much harder to do inside the rhumbatron. To solve the problem, a Teflon holder was produced to fit inside the rhumbatron and hold the sample in place. Two holes were drilled in the bottom to allow for the gold wires to leave the rhumbatron. The gold wires were coated in PVA glue to stop them from making electrical contact with the side of the rhumbatron. Once the wires were outside the rhumbatron, they were attached to the probe's ISHE lines with silver paint. The holder can be seen in Figure 3.10.

ISHE signals can be detected using the lock-in amplifier in the same way as ESR signals, as the ISHE only 'turns on' at the same time as the magnetic resonance that causes it. A more detailed account of the process of making an ESR measurement is presented below.

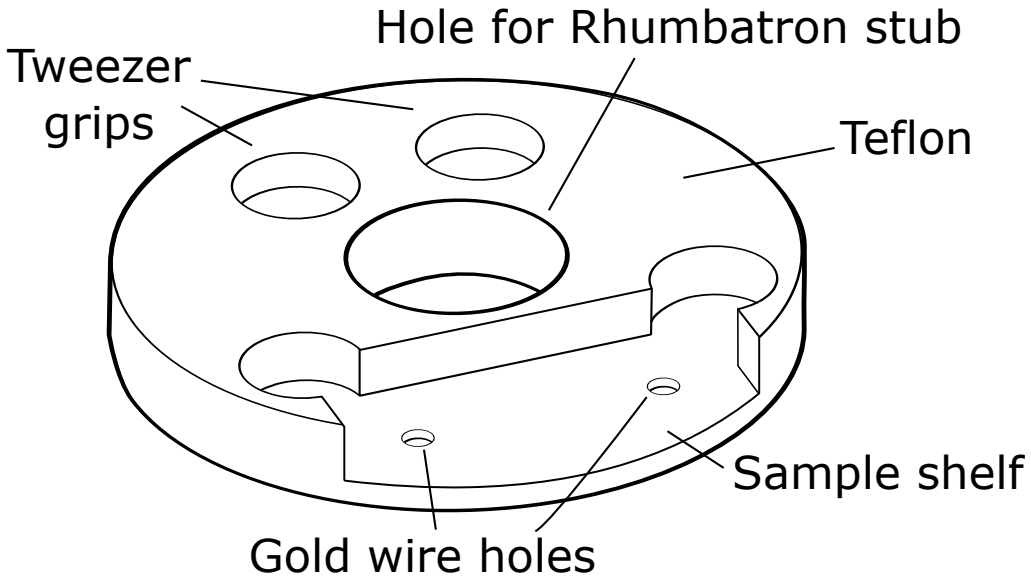


Figure 3.10: Diagram of the rhumbatron sample holder. This Teflon annulus fits snugly inside the rhumbatron and ensures that the metallic samples do not contact the rhumbatron wall.

ESR experimental details, and how to interpret the results

The physical theory behind magnetic resonance was discussed in §2.2.1, where it was determined that when radiation of the correct magnetic resonance frequency is applied to a sample in a magnetic field, the sample is able to absorb some of the energy from the microwaves.

If the microwaves are being applied using a microwave cavity, then the cavity will have a specific quality factor Q. As $Q = 2\pi \frac{\text{energy stored}}{\text{energy dissipated per cycle}}$, when the applied magnetic field is swept from below to above the resonance, there will be a dip in the Q factor, as the sample provides a new channel for energy loss from the cavity. This dip in Q factor can be detected by observing the variation in the transmission properties/output of the cavity.

If the microwaves are being applied to the sample by a stripline, there is no resonant circuit, and therefore no Q to measure. When the sample is on resonance, it locally changes the impedance of the stripline, which leads to both reflections and attenuation of the microwave signal. This can be detected as a dip in the microwave throughput of the stripline. It is noted that, in this case, as there is no resonant cavity, it is possible to sweep (and modulate) the frequency of the microwaves while

fixing the applied field, in addition to the aforementioned method of sweeping the field.

Interpreting the results The dips in the transmission of the microwave signal as either $\boldsymbol{B}$ or f is swept represent the 'tiny signal' mentioned in §3.1.3. Figure 3.11 shows how the ESR signal is processed by the lock-in amplifier. Figure 3.11a shows the relationship between the signal output and the applied field for a resonant experiment (at a constant frequency). Figure 3.11b shows how $\boldsymbol{B}$ changes with time, as $\boldsymbol{B}$ is swept with and without $\boldsymbol{B}$ field modulation. Figure 3.11c shows the output signal that would be measured using the modulated sweeps in Figure 3.11b. Figure 3.11d is the AC component of the modulated signal in 3.11c. When this signal is heterodyned, the envelope in Figure 3.11d is recovered, which is the 'result' provided by the lock-in amplifier. This signal turns out to be the derivative of the original resonance shape, and can be used to calculate the location of the resonance, as well as its linewidth. As the background noise has been filtered out, this method can be used to measure resonance lines that would usually be hidden behind background noise. It is also noted here that setting the amplitude of the modulation to be roughly equal to the resonant linewidth generally provides the largest signal output.

Field, frequency, and amplitude: sweep, modulate, or fix? When designing resonance experiments, there are several options as to the parameters that can be varied. The first choice to make is between fixed field/variable frequency or fixed frequency/variable field sweeps. As mentioned earlier, if a microwave cavity is being used, only the fixed frequency option is available as the cavity resonance condition dictates the operational frequency.

The second choice is what to modulate. As stated above, $\boldsymbol{B}$ is a good choice for ESR, as the field can be easily modulated using modulation coils, and a fairly sizable modulation (3 mT) is achievable. Unfortunately, for ISHE measurements, field modulation is a poor choice. This is because the small gold wires used to connect the sample to the SMA cables also 'see' the modulating $\boldsymbol{B}$ field, which can lead to an

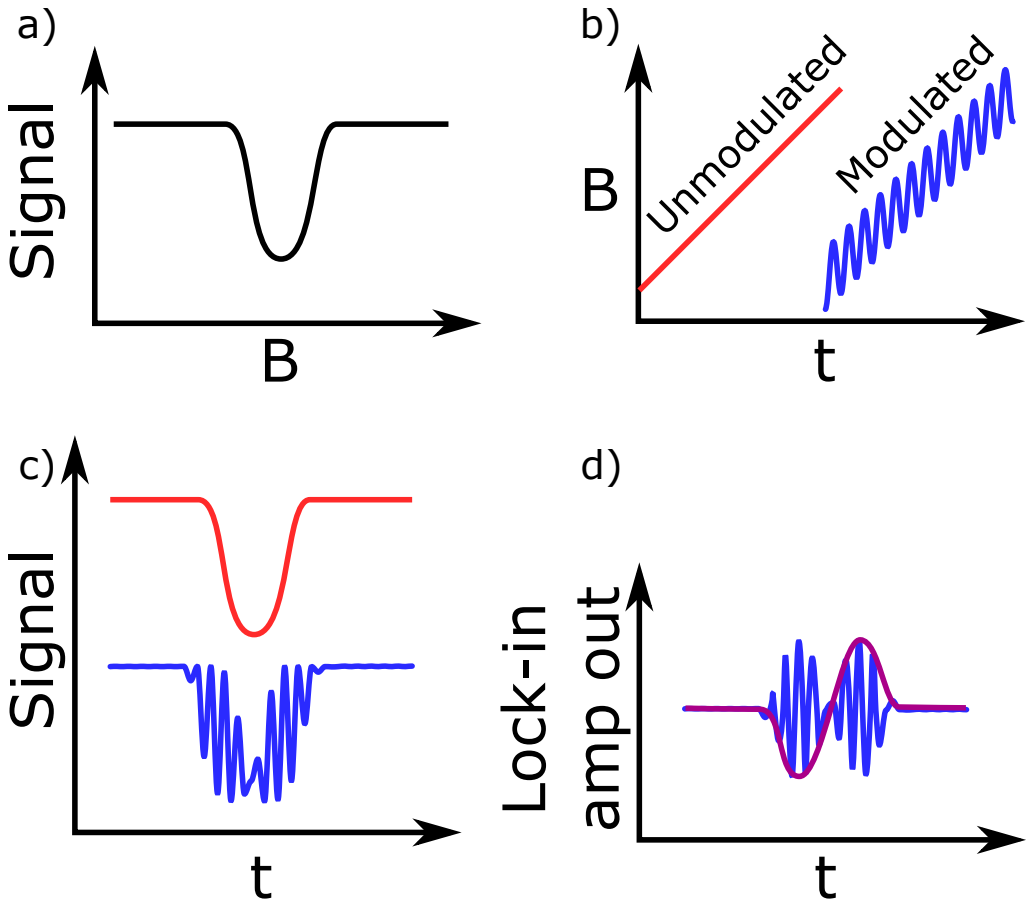


Figure 3.11: Schematic diagram showing how a lock-in amplifier processes an ESR signal. a) The original shape of the resonance signal as $\boldsymbol{B}$ is swept and f is held constant. b) Plot of magnetic field against time for the modulated and unmodulated field sweeps. c) Output signals from the rhumbatron with respect to time for the two different sweep profiles. d) The AC component of the modulated output signal, with the envelope found via heterodyne down-conversion added in purple. This envelope takes the form of the derivative of the original signal.

induced voltage developing across the ISHE output terminals, regardless of whether the system is on resonance or not. This contamination of the output ISHE signal with an erroneous signal at the modulation frequency renders the measurement useless.

It is also possible to modulate frequency. The microwave signal generators used have a 0.3, 1, 3, and 10 MHz frequency modulation setting built in. For the experiments here, this feature is unhelpful, as the linewidths of the materials being used are generally much wider than this. The linewidth of the resonant cavity used is however on this scale, which means a frequency modulated input would lead to an amplitude modulated throughput signal, which would overshadow any potential ESR measurements.

The final type of modulation available is amplitude modulation. Although ineffective for ESR measurements (modulating the amplitude of the input microwaves leads to modulation of the output microwaves, regardless of the resonance conditions), it is useful for ISHE measurements. As the ISHE signal should be zero until resonance occurs, amplitude modulation of the microwaves leads to the necessary amplitude modulation of the ISHE voltage as the field (or frequency) is swept across the resonance.

3.2 Spin Battery Experimental Results

The basic Spin Battery experiment was outlined in §2.4.4, and was performed for several different host/relaxer combinations. The results of these experiments are presented here, while a more detailed discussion of the data can be found in §3.3.

3.2.1 Preliminary data

Before diving in and attempting to measure new physics, preliminary measurements were made to ensure that the equipment was operational, and providing reliable data. This involved making measurements with known outcomes, as well as invest-

igating the resonant behaviour of monolayer films of some of the relevant materials.

Commercial spectrometer data

To facilitate the investigations into the spin battery using the author's equipment, a commercial continuous wave ESR spectrometer (a Brucker EMX) was used to investigate resonances in some of the samples. By establishing the relative sizes, g-factors, and linewidths of the resonances in the samples, it was easier to locate and investigate the same resonances in the in-house assembled ESR setup.

Figures 3.12 and 3.13 show the ESR traces (showing the derivative of the resonances) for films of NiPt, AgPt, CuPt, and a sample of DPPH, and one trace with an empty ESR sample tube. Details of these films (and of DPPH) are provided in sections below. A Lorentzian derivative curve was fitted to each of the traces, and the goodness-of-fit value (R-squared), along with the key fitting parameters (B_{Res} and linewidth) and their 95% confidence bounds (as produced by the fitting programme) were recorded in Table 3.1. B_{Res} was used in conjunction with the microwave frequency to calculate the corresponding g-values.

All of the measurements were made using microwaves of between 9.3 GHz and 9.9 GHz, though their precise values are provided in the caption and Table 3.1. The apparent deviation away from the $g \approx 2$ resonance in the AgPt case is caused by this frequency difference. This plot demonstrates the range of signal strengths that are being investigated. The absence of an obvious $g \approx 2$ ESR signal in the CuPt also highlights the fact that even with specialist equipment, it may not be possible to excite/detect ESR in some materials.

The g-factors and linewidths for the samples of NiPt, AgPt and DPPH presented in Table 3.1 were used to assist in further measurements in the ESR/ISHE setup. It is noted that the resonances in the CuPt trace appear far from the $g = 2$ value. It is proposed that these may be explained via the 'solid effect'.

Solid Effect in CuPt The solid effect occurs when the flip-flip or flip-flop transitions in the energy level diagram in Figure 2.1 are driven. This produces two

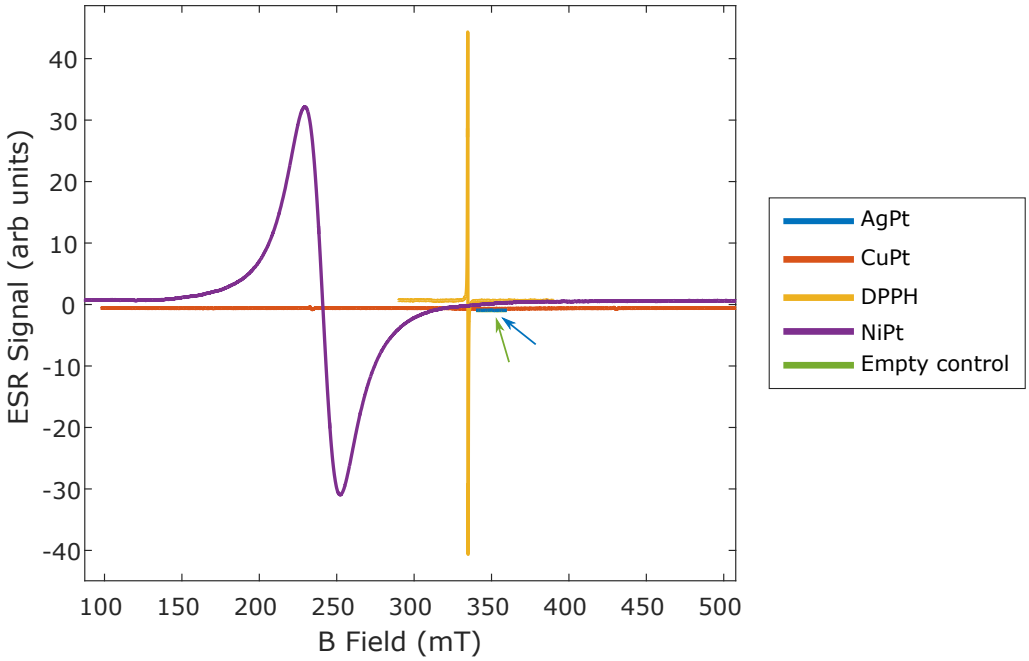


Figure 3.12: ESR traces of several thin film samples made in the Brucker EMX commercial spectrometer, presented to show the relative signal sizes. The microwave frequencies used for each sample were: AgPt - 9.8661830(5) GHz, CuPt - 9.3857560(5) GHz, DPPH - 9.3871540(5) GHz, NiPt - 9.3875360(5) GHz, and Empty ESR tube - 9.8682660(5) GHz. A zoomed in view of the AgPt and Empty tube traces is presented in Figure 3.13.

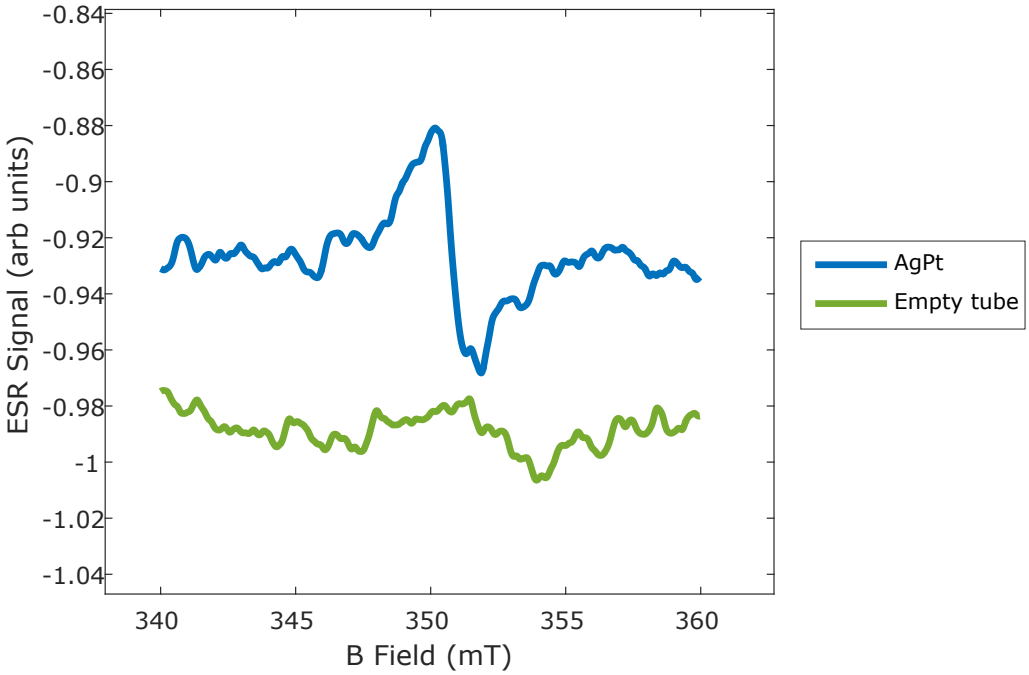


Figure 3.13: ESR traces of the AgPt film and Empty tube in the commercial spectrometer, with microwave frequencies of 9.8661830(5) GHz and 9.8682660(5) GHz respectively. The resonance in the AgPt is visible, but very small compared to the other traces in Figure 3.12.

Material	frequency (GHz)	B_{Res} (mT)	Linewidth (mT)	R-squared values of fit	$g = \frac{f}{B_{\mathrm{Res}} \times \frac{\mu_{\mathrm{B}}}{h}}$
AgPt	9.8661830(5)	350.8(0)	2.589(62)	0.9383	2.009
CuPt 0°	9.3857560(5)	233.5(0)	2.079(63)	0.9208	2.872
CuPt 0°	9.3857560(5)	429.8(0)	1.857(84)	0.8667	1.561
CuPt 45°	9.3870250(5)	289.8(0)	2.110(131)	0.7779	2.314
CuPt 45°	9.3870250(5)	419.2(0)	1.644(73)	0.7364	1.600
NiPt	9.3875360(5)	240.9(0)	38.93(4)	0.9997	2.784
DPPH	9.3871540(5)	334.7(0)	0.4475(9)	0.9993	2.004

Table 3.1: Details of the resonances observed in Figure 3.12. The CuPt resonances shown in Figure 3.12 are recorded as CuPt 0°, when the applied field was in the same plane as the sample. A second set of resonances were recorded for CuPt (but not plotted here) in which the sample was rotated by 45°. This was done to assist the characterization of the CuPt resonance peaks. B_{Res} and linewidth values were extracted from Lorentzian derivative fits of the data (R-squared values of each fit are recorded here). The 95% confidence bounds for the extracted parameters are indicated in brackets. The g-values are rounded to four significant figures.

resonances either side of the ESR resonance. Although there was no $g = 2$ resonance observed in the CuPt film, resonances were visible on either side. To determine whether the solid effect was responsible for these features, the CuPt sample was rotated 45° in the cavity, such that the applied magnetic field was no longer in the plane of the sample. This shifted the location of the resonance peaks, which are recorded in Table 3.1.

For a fixed frequency, the $\boldsymbol{B}$-field location of each of the resonances can be calculated by $\hbar\omega = (g_e\mu_{\mathrm{B}} + g_n\mu_n)\boldsymbol{B}_+ = (g_e\mu_{\mathrm{B}} - g_n\mu_n)\boldsymbol{B}_-$. The ratio of $\frac{\boldsymbol{B}_+}{\boldsymbol{B}_-}$ should be constant for both measurement angles. For the 0° measurement, this ratio is 0.5432. Using the g_n for platinum (0.60952 [46]), the theoretical ratio is 0.53342. This suggests that this measurement may be the solid effect in platinum.

The ratio for the 45° measurement is 0.6913, which suggests that the coincidence of the 0° and the theoretical ratios was just that - a coincidence. These greatly differing ratio measurements effectively rule out the possibility of the solid effect being responsible for the peaks. Instead, it is suggested that the resonances are down to impurities in the sapphire substrate. Unfortunately, it was not possible to investigate this further, as a clean, film-free substrate was not available.

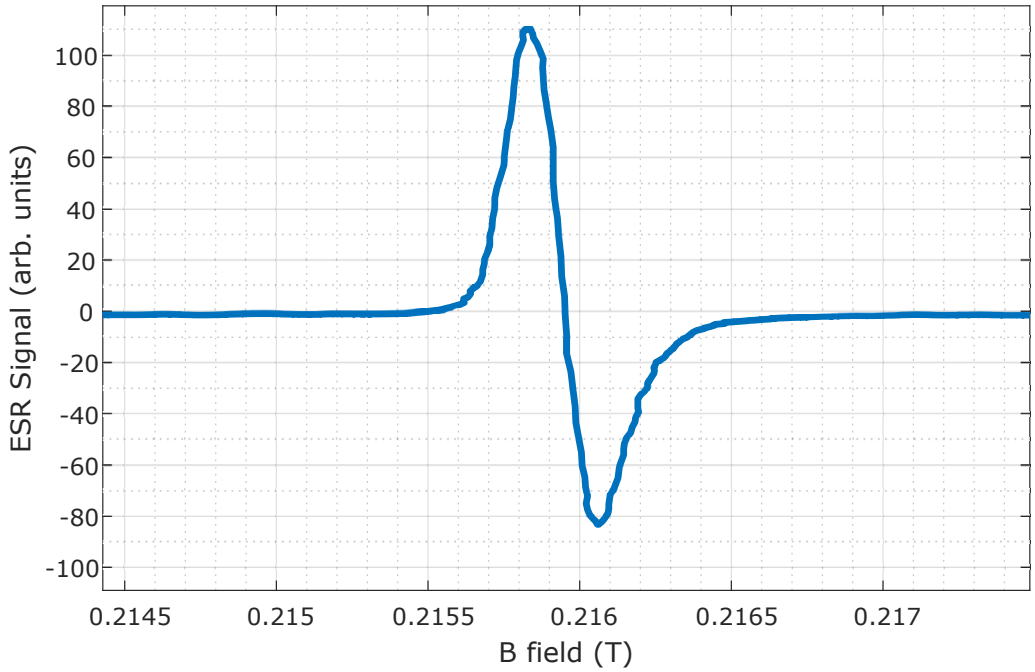


Figure 3.14: Rhumbatron ESR trace of DPPH at 10.524 GHz. The $\boldsymbol{B}$ field was modulated by 0.4 mT, and swept by 0.1 mTs^{-1}. The time constant on the lock-in amplifier was 1 s.

DPPH

2,2-diphenyl-1-picrylhydrazyl, or 'DPPH' as it is known, is an organic chemical compound which also happens to be a stable free radical. This makes it an excellent choice for usage in preliminary ESR experiments, as its paramagnetic properties are well characterized, and consistent. As a 'lighthouse' molecule, it is a popular choice for testing the functionality of a setup, as it is easy to detect and has a known g-factor, which allows for easy calibration of any applied magnetic fields.

Measurements of DPPH were periodically made over the entire course of the thesis to ensure that the field calibration of the magnets remained accurate. Figure 3.14 shows an ESR trace of DPPH in the rhumbatron. Details of the measurement are provided in the caption.

3.2.2 YIG/Pt

To test the ISHE measurement system, a sample of YIG/Pt was used. The sample comprised a $\approx 1\,\mu$m layer of YIG grown by liquid phase epitaxy [47] on a substrate

of gadolinium gallium garnet (GGG), topped with 10 nm of sputtered platinum. As a (ferri)magnetic insulator, YIG has a strong FMR resonance, that can be easily excited by striplines or antennae. Previous experiments [17, 38, 41, 48] have already successfully demonstrated spin pumping from YIG into platinum, as well as measured the inverse spin Hall voltage induced by this. This experiment was repeated here as a sanity check of the experimental setup.

The sample of YIG/Pt has two gold wires attached with silver paint that also connect to an SMA output port. The film is placed face down on some Teflon tape, which was in turn laid across a microwave stripline. Figure 3.15 shows the stripline throughput as the magnetic field was swept across the resonance. This measurement was made without the use of a lock-in amplifier, which was instead used to measure the ISHE signal generated by the spin pumping during the same run, which is seen in Figure 3.16. For this experiment, frequency was modulated sinusoidally by ± 1 MHz.

By repeating the experiment, but with the direction of the applied field reversed, it was possible to see that the direction of the ISHE voltage had been reversed. This is a tell-tale sign that ISHE had indeed been detected, as can be seen by revisiting §1.2.4.

It is noted that the shapes of the traces in Figure 3.16 are not Lorentzian derivatives as might be expected from lock-in measurements of a resonance experiment. This is due to the presence of both symmetric and anti-symmetric components in the raw ISHE signal. The anti-symmetric component is attributed to the Anomalous Hall Effect (AHE), which will be discussed in §3.2.4, whereas the symmetric component is generated by the inverse spin Hall effect. The fact that the two peaks that have the same sign (the two down peaks for the red trace and the two up peaks for the blue trace) are of different heights is evidence that there is indeed a symmetric component to the ISHE signal.

This experiment demonstrates that it is possible to replicate the ISHE measurements made in previous works [41], and provides a good foundation for further ISHE work.

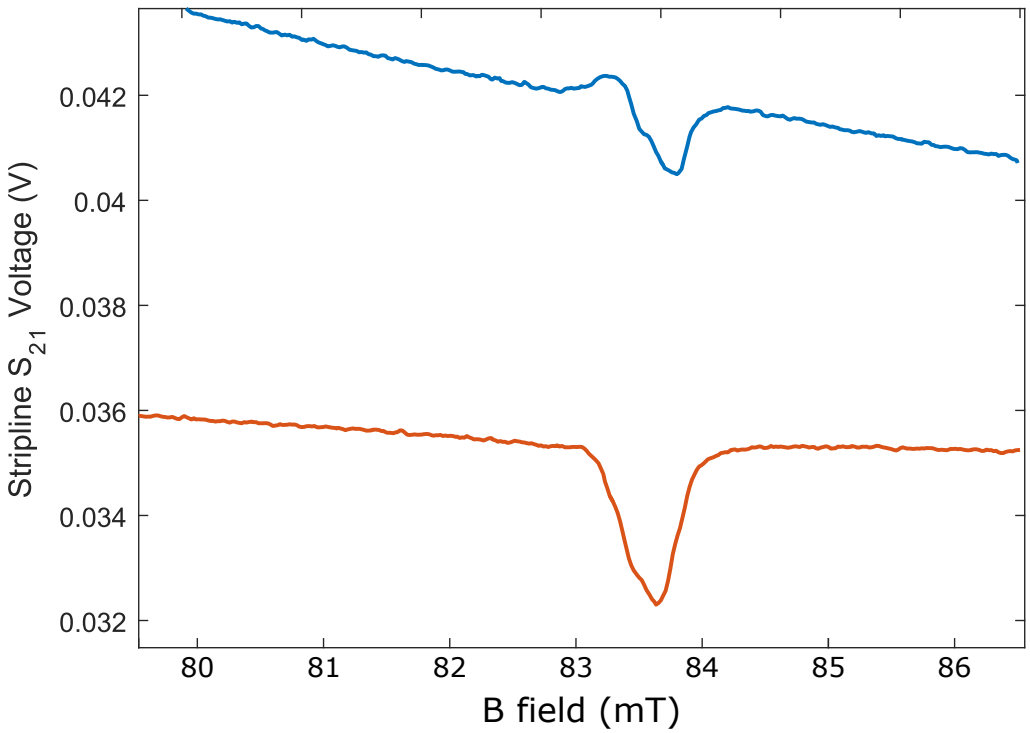


Figure 3.15: FMR signal of the YIG/Pt bilayer, measured via the changes in the throughput of the microwave stripline. The two traces represent two sweeps between which the polarization of the applied magnetic field has been reversed. The microwaves used were at 3.75 GHz, and were frequency modulated by ±1 MHz at a rate of 1 kHz. The field was swept by 25 μTs^{-1}, and the lock-in amplifier time constant was 3 s.

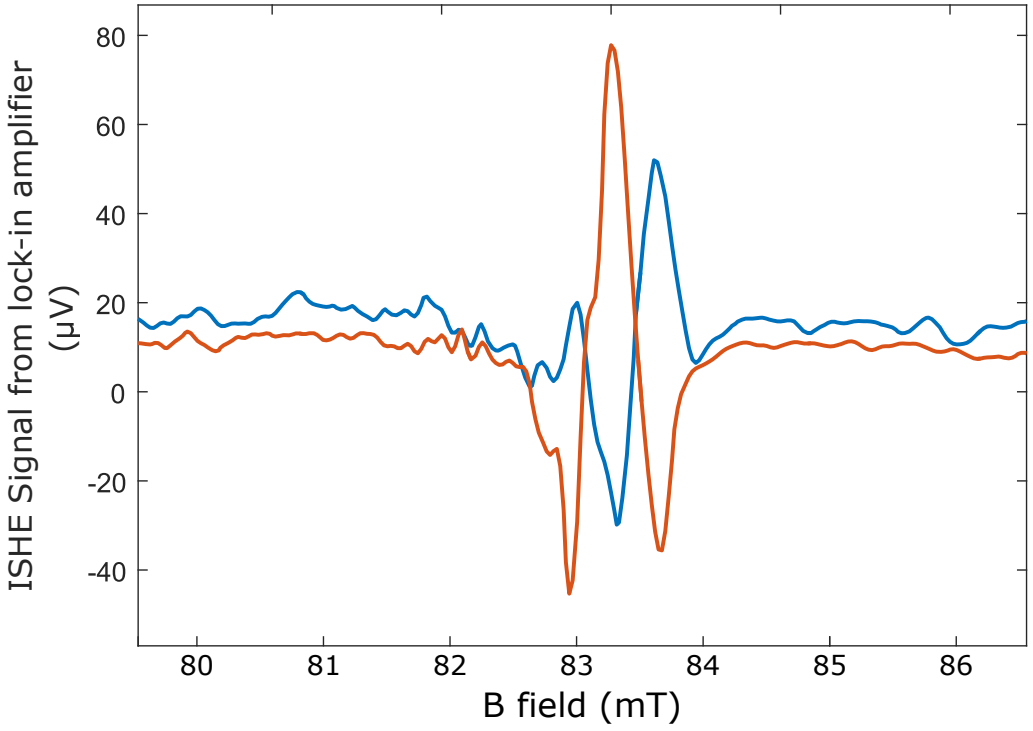


Figure 3.16: ISHE signal of the YIG/Pt bilayer, measured via a lock-in amplifier, with the same sweep parameters as used for the data displayed in Figure 3.15.

3.2.3 Ag/Pt and Cu/Pt

ESR and ISHE measurements were attempted on silver-platinum and copper-platinum metallic bilayers. The AgPt sample was grown on a glass substrate via resistive thermal evaporation, with metal thicknesses of $\approx 810\,\text{nm}$ of silver followed by $\approx 24\,\text{nm}$ platinum. These were the thicknesses that were calculated to be optimum in the model presented in §2.4.6. The CuPt sample was grown on a sapphire substrate by a collaborator in Kaiserslautern, using molecular beam epitaxy [49], with a copper thickness of 10 nm followed by an 8 nm layer of platinum.

As demonstrated in §3.2.1, it was not possible to detect ESR in the CuPt sample, even in the Bruker EMX spectrometer, however it was possible to detect a small AgPt signal. Unfortunately, in the author's experimental setup, it was not possible to detect an ESR signal or an ISHE signal for either sample, despite investigating a wide swathe of parameter space over 497 different data runs. This included experiments at temperatures down to 4 K.

This failure to detect a signal is attributed to one or more of three causes. The first is that of sample volume: the CuPt sample was significantly thinner than the AgPt sample. As the AgPt resonance that we detected was tiny, barely above the noise threshold of the spectrometer, it follows that if the CuPt had a similar size resonance, it may not have been possible to detect it due to the decreased volume of the sample.

There is nothing to suggest that the CuPt should have a similar size resonance to the AgPt, which leads to the second potential reason for lack of CuPt signal — the resonance linewidth. Some metallic samples are known to have very broad resonances [50]. If the modulation used during the measurement is too small with respect to the linewidth, then the lock-in method becomes ineffective. This is because the modulation is no longer able to move the sample on and off the resonance, so the amplitude of the modulated signal being passed to the lock-in amplifier is much smaller. This could also be the case for any potential CuPt resonance.

Finally, why was it not possible to detect the ESR signal in the custom experi-

mental setup for the AgPt film? It is believed that this is due to deficiencies in the apparatus in comparison to the EMX spectrometer. The Q of the EMX is ≈ 7000, whereas the Qs measured for the rhumbatron generally ranged from $200 - 400$, depending on the rhumbatron's contents. This means that the microwave power experienced by the sample may have been considerably less in the in-house experiments, and therefore insufficient to excite a resonance that was detectable via the lock-in amplifier, or via ISHE.

There is one further possibility for why it was not possible to make these measurements in CuPt or AgPt, but this explanation is saved until §3.3, for reasons that will become clear in that discussion.

3.2.4 Ni/Pt

The nickel/platinum bilayer used in this experiment was grown by resistive thermal evaporation onto glass. The nickel was 40 nm thick, topped with 10 nm of platinum, (thicknesses chosen after considering the model of §2.4.6). ESR and ISHE measurements for the NiPt film are shown in Figure 3.17. Successful measurements of the FMR were made in the rhumbatron using a field swept, field modulated arrangement, while the ISHE was measured using amplitude modulation for the same field sweep.

A fit of the ISHE data is shown in Figure 3.18, and has an equation of the form

$$V_{\text{ISHE}} = \left(\frac{16(B-a)bc}{\pi \left(4\left(B-a\right)^2 + b^2\right)^2} \right) + d + ex + \left(\frac{fg}{\pi \left(\left(B-a\right)^2 + f^2\right)} \right) \tag{3.4}$$

where $a = 0.3047$, $b = 0.1678$, $c = 0.003421$, $d = 0.9245$, $e = 0.1772$, $f = 0.01587$, and $g = 0.02957$. The fit comprises a symmetric, and an anti-symmetric component. The symmetric component (a Lorentzian curve, represented by the second large bracket) is generated by ISHE, whereas the anti-symmetric component (a Lorentzian derivative curve, represented by the first large bracket) is caused by the Anomalous

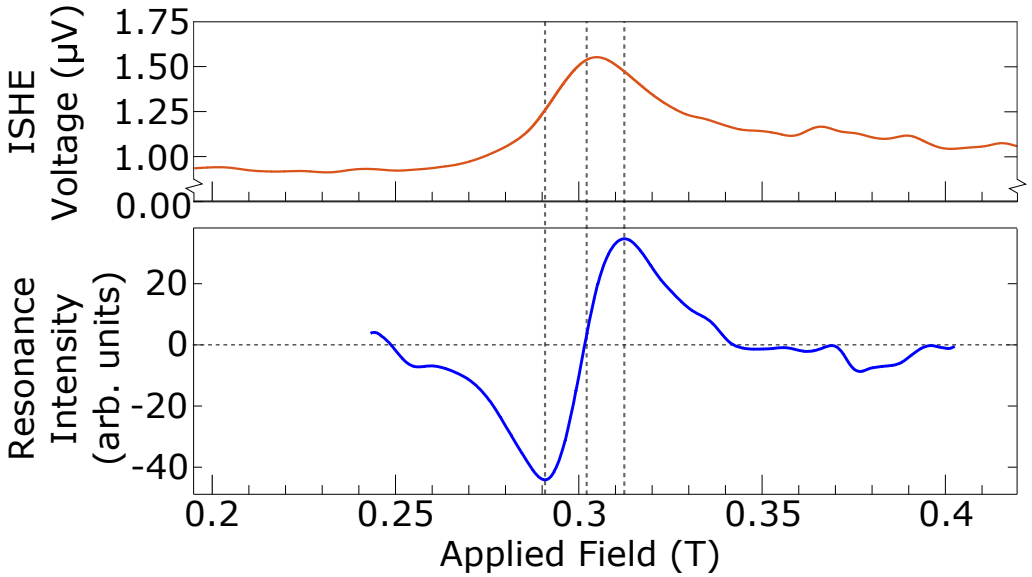


Figure 3.17: ISHE (top) and ESR traces (bottom) for the NiPt bilayer, measured in the rhumbatron. The microwave frequency was 10.380 GHz, the field sweep speed was 0.5 mTs^{-1}, and the lock-in amplifier time constant was 3 s. The AM modulation frequency used for the ISHE measurement was 1 kHz, whereas the $\boldsymbol{B}$ field modulation frequency used for the FMR measurement was 84 Hz.

Hall Effect (AHE) [51]. The Anomalous Hall Effect occurs due the interaction between the electric field component of the microwaves and the magnetic moment of the ferromagnet. This is shown in Figure 3.19. As the field sweeps to the other side of the resonance (not shown in the diagram), the phase of the $\boldsymbol{E}$ field with respect to $m(t)$ shifts by 180°, leading to a DC voltage in the opposite direction.

Even though the rhumbatron was designed to reduce the amount of $\boldsymbol{E}$ field located in the sample, sufficient field remains to generate an AHE signal. After removing the anti-symmetric component of the fit, a sizable symmetric component remains. The presence of this ISHE signal in NiPt at the FMR frequency is a clear example of metal-metal spin pumping, the significance of which will be discussed in §3.3.

The measurements on the NiPt system yielded another interesting result, which is presented below. ISHE-type voltage measurements across the sample were made as the applied field was swept from below to above zero field, and back. The results are presented in Figure 3.20. It can be seen that a hysteresis loop is present in the output voltage. This suggests that some component of the voltage output is

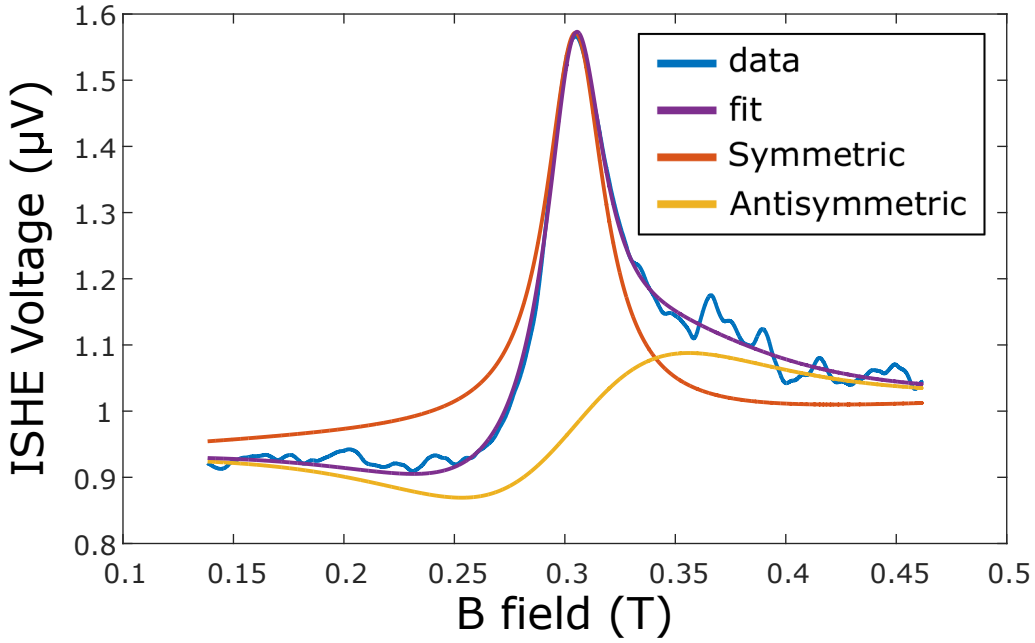


Figure 3.18: The symmetric and antisymmetric components of the curve fitted to the NiPt ISHE signal. The equation and parameters used are shown in Equation 3.4. The presence of an antisymmetric component is attributed to the anomalous Hall effect, whereas the symmetric component is generated by the inverse spin Hall effect.

dependent on the direction of the magnetization of the film, as there is a step change in output when the applied field becomes strong enough to flip the magnetization of the film.

One possible origin of this phenomenon is related to the Seebeck effect [10, 52], in which a thermal gradient leads to a flow of charge. As the sample is irradiated by microwaves, small amounts of non-resonant absorption may lead to an increase of the sample's temperature. If the rate of cooling between the platinum and the air is different to that of the nickel to the glass, then a thermal gradient may be established across the interface between the two layers, driving a charge current from one metal into the other. As one of the metals is a ferromagnet, it could be assumed that this charge current will be spin polarized, (recalling ferromagnetic spin injection from §1.2.4), and as such lead to an ISHE voltage once rectified in the platinum. When the sign of the magnetization changes, the polarization of the spin current changes, and thus the effect's contribution to the ISHE voltage also switches sign, leading to a step in the signal voltage, which can be seen in Figure 3.20.

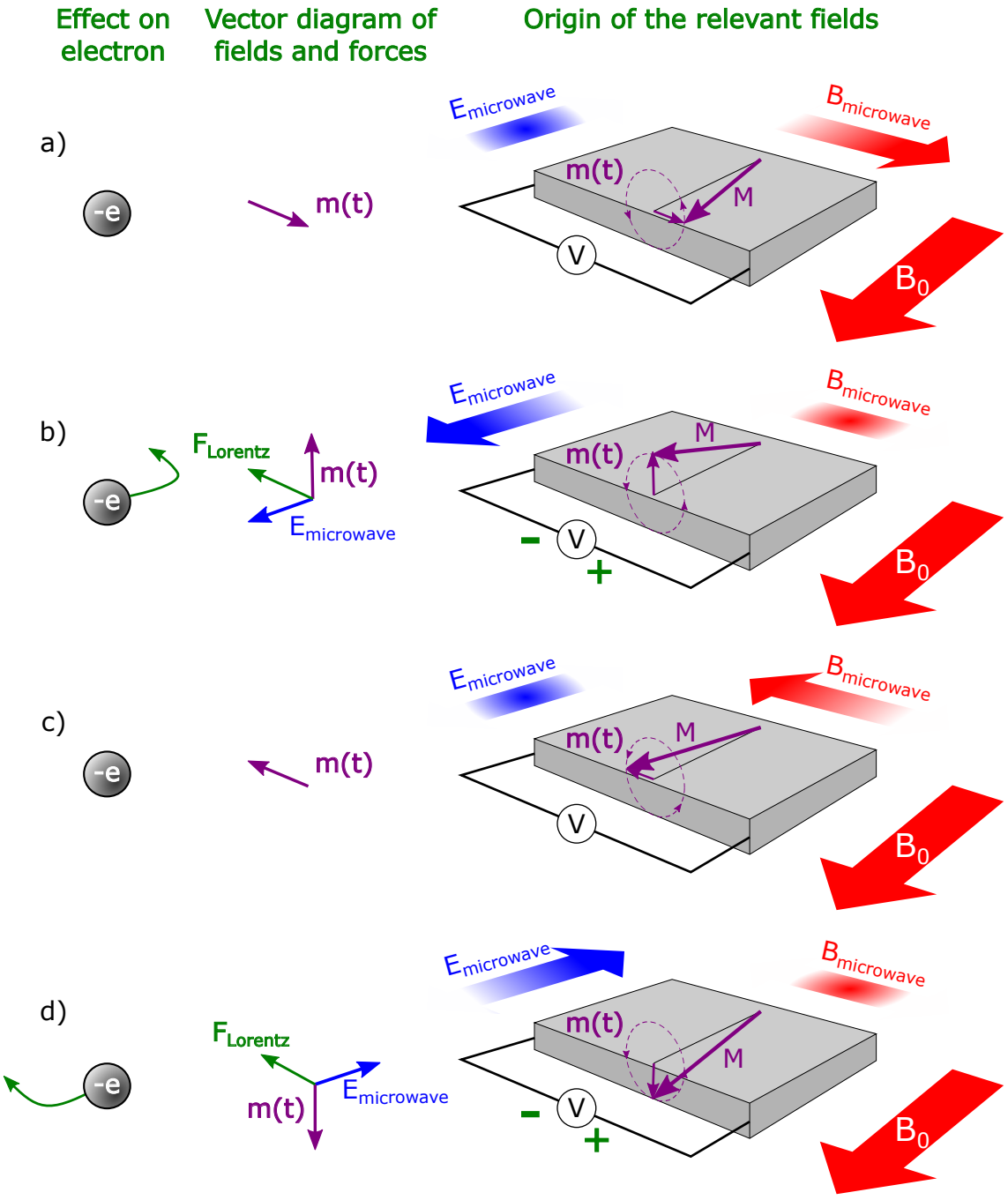


Figure 3.19: The Anomalous Hall Effect (AHE) when the applied field is just below $\boldsymbol{B}_{\text{FMR}}$. The microwave $\boldsymbol{E}$ field accelerates electrons, which experience a Lorentz force due to the out-of-plane component of the precessing magnetization $\boldsymbol{M}$. This can be seen in b) and d), and leads to a DC voltage appearing across the sample.

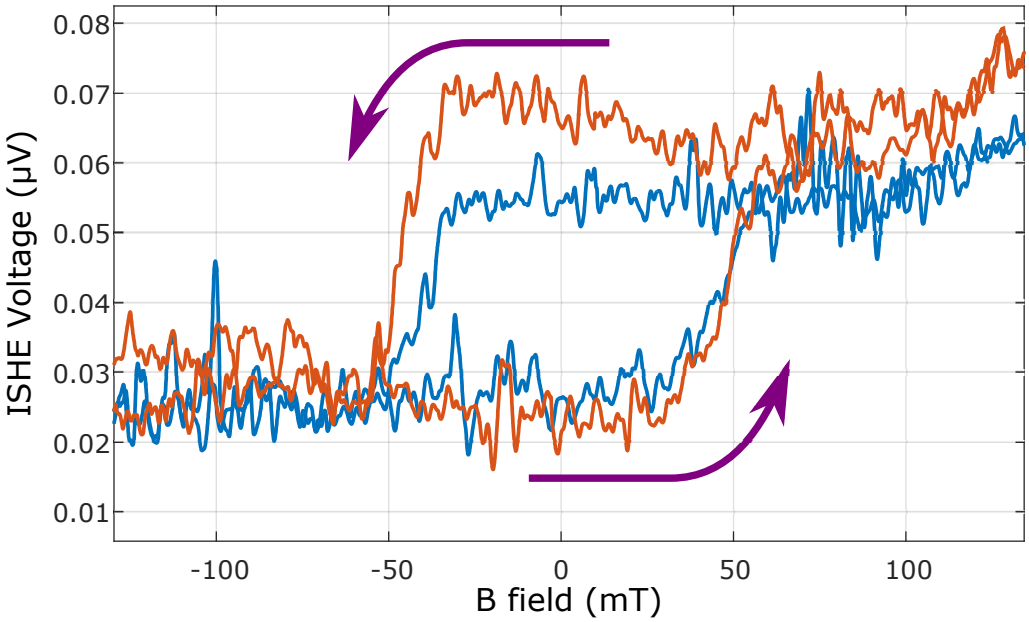


Figure 3.20: Hysteresis loop in the 'ISHE' signal of the NiPt film around zero field. The measurement was made in the rhumbatron using microwave radiation of 10.383 GHz. The two traces represent identical measurements, and show the repeatability of the result.

3.3 Discussion of the results, and conclusions about the Spin Battery

The two key results from the above measurements are: that it is possible to measure FMR and ISHE in the NiPt bilayer, and that it is also possible to detect ESR in the AgPt film, but only just. In this section, an explanation will be provided for why this was the case.

3.3.1 Why such a small signal?

In the measurements made in the EMX spectrometer, presented in Figure 3.12, the peak-to-peak size of the NiPt resonance was ≈ 730 times that of the AgPt resonance. The throw-away explanation of this (and the fact that the resonances are located at different g values), is that FMR was occurring in the NiPt, while ESR occurred in the AgPt, and these are just 'two different processes'.

As the difference between the two measurements is purely quantitative (the resonances are qualitatively the same), it suggests that the two experiments may not in

fact be so different. Indeed, the fundamental processes occurring in both systems are very similar: electrons are precessing under an applied field, while also being excited by an oscillating microwave field. The only difference between the two situations is the inclusion of (or more precisely, the dominance of) the exchange interaction in the ferromagnet. As such, despite the fact that FMR and ESR are usually treated using different models, it may be possible to find an explanation that encompasses both systems.

3.3.2 Three models of Ferromagnets and Ferromagnetic resonance

Before proceeding, it will be helpful to recall some of the models used to understand ferromagnets and ferromagnetic resonance. These include the Stoner criterion, the Landau-Lifshitz-Gilbert equation, and the magnon model.

Ferromagnets and the Stoner criterion

The conditions under which the exchange interaction can lead to itinerant ferromagnetism can be summed up by the Stoner criterion [11]. This can be effectively understood by again invoking the two spin-channel model of a metal. If the exchange energy gained by flipping one more spin to a specific alignment is greater than the kinetic energy cost of pushing the electron above the Fermi surface, then the flip occurs, and the magnetization of the metal increases. This process effectively repeats until the energy gain is NOT greater than the energy cost, and it is this equilibrium which is encapsulated in the Stoner criterion.

The effect of this interaction on the two spin-channel diagram is presented in Figure 3.21c. This looks very similar to the Pauli paramagnet diagram in Figure 2.2, which is reprinted in Figure 3.21b, for the purpose of direct comparison. The main difference is that in the paramagnetic case, the shift in the energy bands is $2\mu_B \boldsymbol{B}$, whereas in the ferromagnet, the band splitting is equal to the exchange quantum. This has the equivalent magnitude of a Zeeman splitting in a field on the

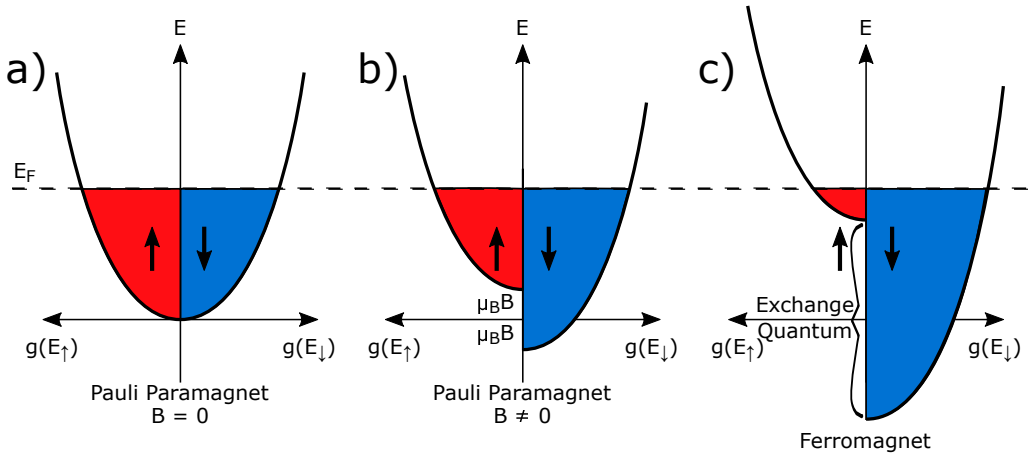


Figure 3.21: Idealised bandstructures of a) a Pauli paramagnet, b) a Pauli paramagnet in an applied field, and c) a ferromagnet. The difference between the Zeeman splitting in Figure 3.21b is on the order of hundreds of times smaller than the exchange splitting in Figure 3.21c.

order of a thousand Tesla [53].

The Landau-Lifshitz-Gilbert equation

The Landau-Lifshitz-Gilbert equation (LLG) works with the vector model of ferromagnets, and governs the evolution of a magnetization in a magnetic field. There are similarities between this treatment of a ferromagnet and the treatment used for single spin resonance in §2.2.1. In the ferromagnetic case, the spin is a magnetization, but the dynamics of its precession can be thought of in the same terms. The LLG is the most common description of FMR, as it can include a phenomenological damping term which incorporates spin-flip relaxation. This is generally a very effective model for most situations, however it is unhelpful when trying to predict the behaviour of individual spins under microwave excitation.

Neither of the two models of ferromagnetic behaviour discussed so far (the classical precessing vector model, or the two spin-channel model) are complete. The vector model does not describe what happens to individual spins when the magnet relaxes, and the two spin-channel model does not account for situations where the quantization axis is different to the magnetization axis, as in FMR. The operation of the Spin Battery in a ferromagnet lies somewhere between these two models, and as such, adaptations must be made to try and explain the behaviour that was observed.

The magnon model

This last model is looked to for insight rather than definitive answers, as it provides an interesting alternative view of ferromagnetic resonance. In §1.2.2, the concept of a magnon was discussed. There, a chain of ferromagnetic spins was imagined, and a single spin was flipped. This single spin-flip was able to delocalise and behave as an 'itinerant spin-flip'. Due to the co-operative nature of the system, all the spins in the chain entered a superposition state of being flipped and not flipped, and the probability of any given spin being found in the flipped state was distributed evenly across the chain. (For clarity, it is noted that if the flipped spin was measured to be on a specific site, the superposition would collapse, and all the other spins would be found in their non-flipped state. This would localise the spin-flip to a single site, incurring the full 'cost' of the exchange interaction, which would be 'paid for' by the act of making the measurement). In the classical model, this distributed spin-flip has the appearance of each of the spins being at a slight angle from straight up, and precessing with a fixed phase relation. If this phase difference between neighbouring spins is zero, then this is the magnonic picture of FMR.

3.3.3 The Spin Battery Model Redux

To incorporate the exchange interaction into the Spin Battery model, the two spin-channel model of microwave excitation must be modified. Similarly to §2.4, and Figure 3.21, a material in an applied magnetic field is considered, in this case a ferromagnet. The magnetization of the metal initially aligns with the applied field, and the two spin channels are split by the exchange interaction. There is a tiny amount of Zeeman splitting for each band, but due to its relative size, it is regarded as negligible. The question that must now be answered is what happens to the system under the application of an oscillating microwave field?

The naïve approach

Under the naïve spin-channel model, it should be possible for each microwave photon to flip a spin, moving towards the equalization of the populations of the two channels. In the limit of extreme pumping, what happens to the two spin channels? In the paramagnet, the populations become equalized, as the photon energy matches the Zeeman splitting. In the ferromagnetic case, the applied microwaves run at the FMR frequency, which is related to the applied field and the magnetization of the material. The photon energies however, are still a lot smaller than the exchange quantum, so what happens in the strong pumping limit? Does the pumping saturate once the band splitting reaches ω_{FMR}? Or does it keep going? If so, where does the energy come from?

It is at this point that it is necessary to break away from the established model in an attempt to solve this problem. In the above naïve approach, the exchange interaction has only been included to increase the band splitting. If the co-operative nature of the electrons is now incorporated into the model, some interesting results emerge.

A more advanced approach

In the same way that all of the spins in the ferromagnetic chain in the magnon model form a superposition of up and down states due to co-operative behaviour when supporting an itinerant spin-flip, the same argument could be made for the itinerant spins in the exchange split two spin-channel model. If instead of labelling each spin by its position (as was done for the 1D ferromagnet), each of the itinerant electrons is now labelled by its k-state, parallels between the two treatments can be drawn.

Flipping any given spin 'costs' an exchange quantum, as with the first step of the magnon example, and shifts that spin from one spin band to the other. This might cause it to end up a great height above the Fermi surface, or only just above the Fermi sea (as the k state remains the same). Any of the available

spins (spins with empty corresponding k states in the other channel) can flip in this way, each paying the same individual energy cost. By introducing the co-operative behaviour of the ferromagnet, it can then be argued that all of the available spins enter into a superposition of flipped and not flipped, with all the spins sharing the same flipped/not-flipped probabilities. By distributing the spin-flip across all available momentum states, the energy cost of flipping a single (but non-specific) spin is reduced to the order of the FMR quantum, just like it was in the ferromagnetic chain in §1.2.2.

Adding more photons to the system increases the probability of an electron in any given k-state being found in the more energetic 'flipped' state. This concept can be incorporated into the spin-channel diagram by introducing transparency or 'fuzziness' to represent the probability of any given state being filled. As all of the electrons that are able to flip now act as a single entity, the spin-channel diagram can be modified to include this with relative ease. This is shown in Figure 3.22.

In this diagram, the effects of applying microwaves at the FMR frequency to the ferromagnet can be seen. Each photon added to the system increases the probability of finding a spin in the excited state, while decreasing the probability of finding a spin in the lower energy state. It can also be seen that the microwaves are no longer restricted from interacting with only the electrons that are up to an FMR quantum below the Fermi surface, as any electrons that are within an exchange quantum of the Fermi surface are able to interact with the microwaves in some way.

This massive increase in the number of participating electrons is the reason behind the large discrepancy in resonance signals measured in the experiments. This increase in population enables the detection of the ESR/FMR signal with greater ease in the NiPt than in the AgPt, and also amplifies the strength of the Spin Battery effect leading to a measurable ISHE voltage in the NiPt bilayer.

It is worth pointing out that this 'fuzzy' model only works for situations where the deviation of $\boldsymbol{M}$ from $\boldsymbol{B}$ is small. This is an acceptable limitation, as experimentally, "the FMR excitation breaks down into spin-wave modes before the magnetization

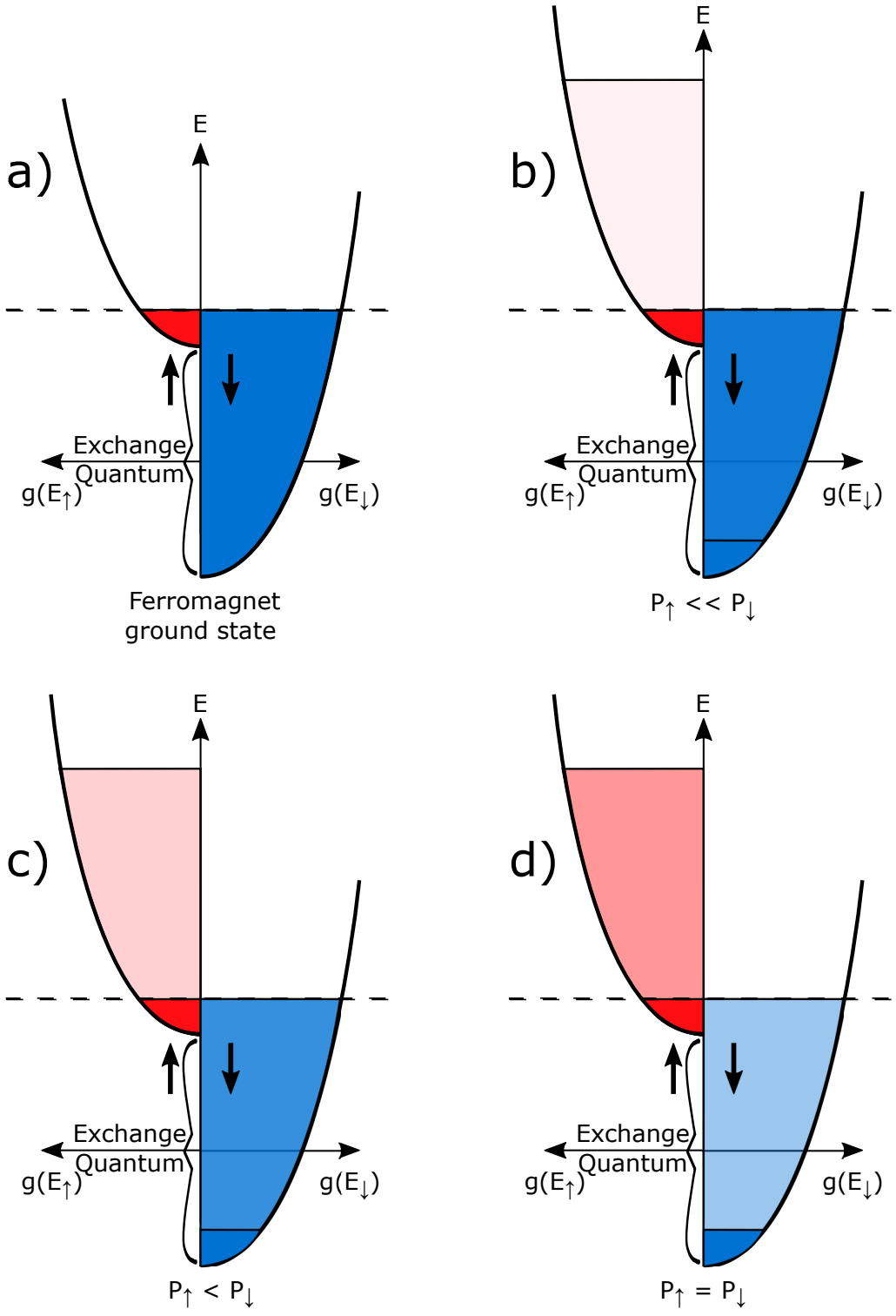


Figure 3.22: Diagram of the two-band model of a microwave irradiated ferromagnet, incorporating the quantum 'fuzziness' caused by co-operative superposition effects. a) The unexcited ferromagnetic ground state seen in Figure 3.21c. b-d) The appearance of the system as increasing amounts of microwave radiation is absorbed by the ferromagnet. The probability of finding a spin in any given state is depicted via the transparency of the two channels, where increased opacity represents increased probability of finding that state occupied.

vector can be rotated appreciably from its initial direction." [7]. This condition is unsurprising, as it is also one of the assumptions of the magnetostatic approximation used to describe low-energy magnons, which were used via analogy to form the basis of the model.

Other refinements to the model

Although the differing magnitudes of the NiPt and AgPt magnetic resonances has been explained, the fact that the ISHE signal of 5 μV for the AgPt bilayer predicted in §2.4.7 was not detected has yet to be discussed. Given that the Ni/Pt FMR signal was ≈ 730 times that of the AgPt ESR signal, and the NiPt ISHE signal was on the order of 0.5 μV, it could be reasonable to predict that the ISHE signal for the AgPt film was on the order of 1 nV. If this is true, this value is 1000 times smaller than the original model predicted, and leads to the question: What was wrong with the model, and how can it be improved?

The two main sources of error in the model are probably to do with the incorrect treatment of thermal considerations, and the treatment of the microwave excitations via the use of a single variable R.

Given that the energy scale associated with the Zeeman splitting in the AgPt experiment is on the order of 100 mK, and that the majority of the measurements were made at room temperature, it is reasonable to assume that the two-channel splitting in both the silver and the platinum were saturated by thermal noise. As the calculation of the excitation rate R used the 'undergraduate' density of state at the Fermi surface $g(E_\mathrm{F})$ rather than the effective density of state ρ^*, this suggests that the value of R might be incorrect.

A related problem with R is the fact that stimulated emission is not considered. In the current model, it is assumed that when a photon is absorbed by the system, it will lead to an electron excitation (indicated by the positive value of R), whereas in reality, when the system is saturated, it is just as likely to cause a stimulated emission. Given that the Zeeman splitting energy is so small with respect to the

thermal energy in the experiment, this is an important process that should be added to the refined model.

Finally, the value of R was calculated by considering how many spins needed to be flipped to maintain a large $\rho^* \Delta\bar{\mu}_{\uparrow\downarrow}$, and not by considering how many spins it was possible to flip using the apparatus of the experiment. In refining the model, it would be worth considering how much power could be applied to the system, and whether or not that might be a limitation on the spin-flip excitation rate.

3.3.4 Conclusions

In these experiments, an inverse spin Hall voltage in a nickel/platinum bilayer was successfully measured. This measurement was explained using the Spin Battery theory, once the appropriate modifications had been made to incorporate ferromagnetic materials. An ESR signal in a paramagnet-paramagnet bilayer of silver/platinum was detected, which was much smaller than the NiPt signal measured in the same way. This variation was attributed to the difference in the number of electrons interacting with the microwaves.

It was suggested that the inability to measure an ISHE signal in AgPt was due to the thermal saturation of the spin-flip transition, which has a Zeeman energy on the order of 100 mK. If the AgPt experiment was performed at mK temperatures, the unexcited system should begin closer to its ground state configuration, and should no longer be thermally saturated. This means that on application of microwaves, it may then be possible to create sufficient spin accumulation to generate a detectable ISHE voltage. This experiment is proposed as the 'next-step' of this work, as a successful measurement of this effect would be strong evidence to support the Spin Battery model.

Chapter 4

The AM/PM Converter

4.1 Introduction to Amplitude and Phase modulation, and the ζ notation

As outlined in §1.3, there are a wide variety of fascinating and variously useful magnonic devices that have thus far been developed. As the development of these magnonic devices is still in its relative infancy, almost no work has been done on methods of linking devices together. As these devices increase in efficiency, it will become desirable to start constructing multiple element magnonic circuits, and at this point, a problem arises: that the data encoding methods with which these devices operate are not always consistent, and a method is therefore needed for converting between the different encoding paradigms.

Conventional computers use binary logic to operate, which is effectively a scalar quantity — a number of electrons are either present, or not. The fundamental unit of magnon computing however, is the complex number, which represents the relative phase and amplitude of a magnon with respect to a continuous, unmodulated reference signal. This quantity is assigned the parameter ζ, such that $\zeta = Ae^{i\phi}$, where A is the relative amplitude and ϕ is the relative phase. The significance of this notation will become apparent over the course of this chapter. To maximise the ease with which magnonic computing elements can be integrated with conventional

CMOS electronics, it is sometimes desirable to continue to use binary logic as the basis for computations, which leads to the question of how to encode binary data in a magnonic system?

The two most common methods by which this achieved are with amplitude modulation (AM), or phase modulation (PM). (Frequency modulation is much less common). It is easy to visualise how data can be encoded in the AM case: magnons are either present, or absent. An alternative, generalised definition of amplitude modulation would be to have a magnon intensity threshold above which the system is declared to be a binary-1, and below which it is defined to be binary-0.

For the PM case, there is a little more flexibility. By comparing the phase of a data signal to the phase of the reference signal, the phase can either be the same, which might be called binary-0, or different — binary-1. The choice of the 'different' phase may be restricted by the functionality of a given device (e.g. the device in reference [54] only works with a 90° phase shift), but in general can be any phase, so long as it is possible to decode the signal afterwards.

The most obvious choice for the PM phase shift is 180°, as this allows two signals with opposite binary states to destructively interfere with maximum efficiency. This is evidently a useful feature as demonstrated in the case of the majority gate discussed in §1.3.1, which operates on destructive interference of phase modulated signals. If one considers the relative phase ϕ of the magnon signal to the reference signal, the binary-0 state can now be defined as having $\phi = 0°$, and the binary-1 state as having $\phi = 180°$.

When considering systems that contain magnonic elements that operate on both AM and PM encoding methods, it is useful use the ζ notation defined above so that it is possible to discuss binary data for the two encoding methods simultaneously. The PM binary-1 state of $\phi = 180°$ becomes $\zeta = -ve$, the PM binary-0 state $\phi = 0°$ becomes $\zeta = +ve$, the AM binary-0 state of 'no magnons' is represented as $\zeta = 0$, and the AM binary-1 state can be represented as $\zeta \neq 0$. These four states are the most important for the remainder of this chapter, however, the ζ notation will be

used more extensively towards the end of Chapter 5.

4.2 The AM/PM converter

Now that the notation for how binary data is encoded into magnon streams has been clarified, the problem of how to convert between the two encoding methods can be considered. A new, simple method based purely on destructive interference of two magnon signals is presented here, which bears a resemblance to the majority gate discussed in §1.3.1.

The basic structure of the AM/PM and PM/AM converters are shown in Figure 4.1. The form is simply that of two converging waveguides, one of which carries the original signal. The contents of the magnon stream arriving at the confluence from the second branch differs depending on which converter is under study.

To convert between an AM signal and a PM signal, as in Figure 4.1a, a continuous wave with $\zeta = -1$ is added to the AM signal of $\zeta = 0$ or 2. The continuous $\zeta = -1$ wave has half the amplitude and is 180° out of phase with the AM signal. This constructively and destructively interferes with the $\zeta = 0$ and 2 values respectively, and results in a PM signal with $\zeta = \pm 1$. To convert between a PM signal back to an AM signal as in Figure 4.1b, a continuous $\zeta = +1$ is similarly added to the $\zeta = \pm 1$ signal, resulting in an AM signal of $\zeta = 0$ or $+2$. If the amplitude of the AM or PM signal is significant for subsequent computational processes, the signal can be amplified or attenuated appropriately.

4.3 Experimental results for the AM/PM inter-converters

4.3.1 AM/PM signal generation and detection

To test the AM/PM converter, it is first necessary to have a source of AM or PM encoded data. An AM data stream can easily be produced in microwave circuitry

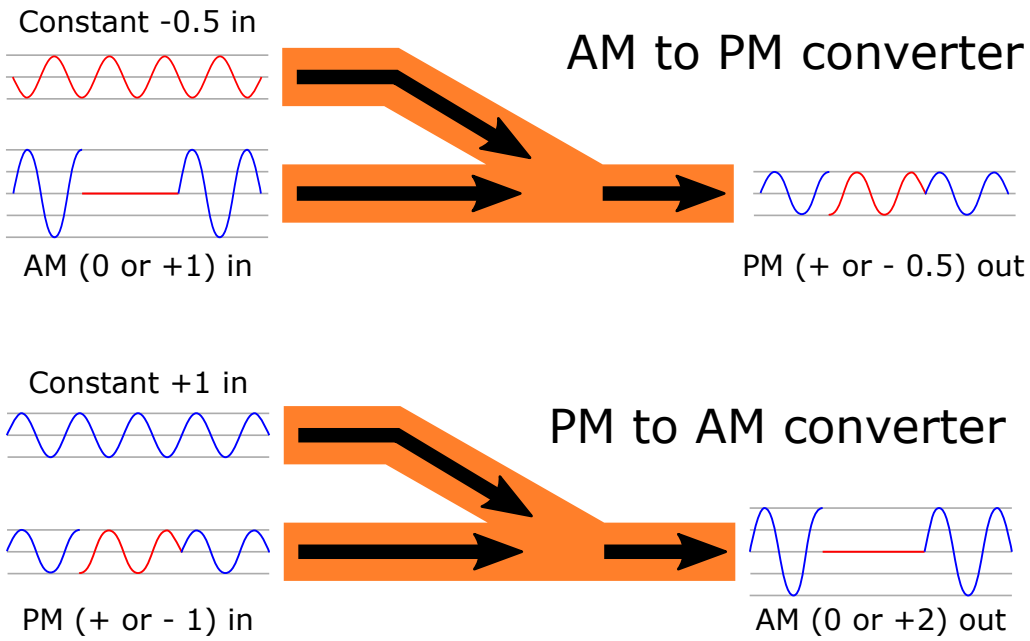


Figure 4.1: Diagrams of the newly proposed AM and PM inter-converters, with explanatory waveforms. Red and blue colouring indicates a phase difference of 180°. a) top: AM to PM converter, b) bottom: PM to AM converter.

using electronically driven microwave switches, and a pulse/signal generator. PM signals are more challenging, however it is possible to produce a data stream with fast switching 180° phase shifts using exactly the same method proposed for the magnonic AM/PM converters.

By assembling the microwave circuit depicted in Figure 4.2, it was possible to generate (and switch between) AM and PM encoded data streams. This was achieved by carefully modifying the length and attenuation of the switch bypass line such that the amplitudes and phases appropriately cancelled once recombination had occurred in the circuit.

The output signal of the AM/PM encoder can be read by multiplying the data stream by a fixed reference signal (the probe), and then observing that new signal on an oscilloscope. This is the 'heterodyne' method of signal decoding, and is one of the signal decoding methods investigated in §5.2.3.

Plots of the AM and PM input pulses are presented in Figures 4.4 and 4.6, the generation of which electrically demonstrated the viability of the AM/PM conversion method. Having generated these pulses electrically, it is possible to proceed to

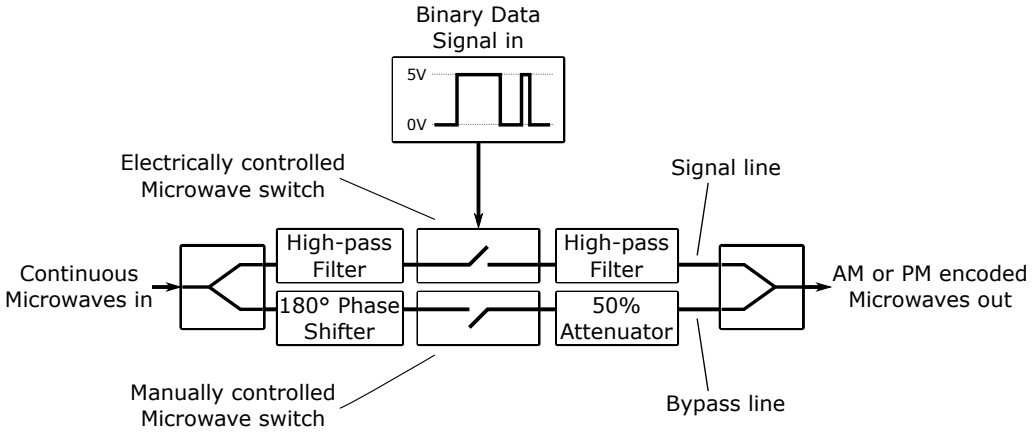


Figure 4.2: AM and PM microwave encoder circuit. Depending on the state of the manual switch, the microwaves leaving the device will be encoded with the binary data using either the AM (manual switch open) or PM (manual switch closed) paradigm. This device is a purely electrical implementation of the devices in Figure 4.1.

experiments in which signals are converted between the two encoding methods within a magnonic system.

4.3.2 AM/PM conversion in a YIG waveguide

Due to restrictions on materials (mainly YIG), experiments of the form depicted in Figure 4.1 were not achievable, however, it was possible to test the AM/PM converter by using a single strip waveguide in a three-antenna arrangement, as seen in Figure 4.3. Here, the data signal was launched from antenna B, while the continuous wave signal was launched from antenna A. The magnon signal detected at antenna C is the output which was analysed. The downside of this method is that the signal launched at B propagates in both directions along the YIG, which, if it were an element of a more complex circuit, could be a potential source of problems. As this experiment is a simple proof of concept however, this experimental arrangement will suffice.

The AM input signal for the AM/PM converter is shown in Figure 4.4. The phase of the probe signal with respect to the reference signal was varied until extremal output voltages were observed. This can be thought of as aligning the probe phase with either of the $\pm\zeta$ axis, and leads to output voltage values corresponding to

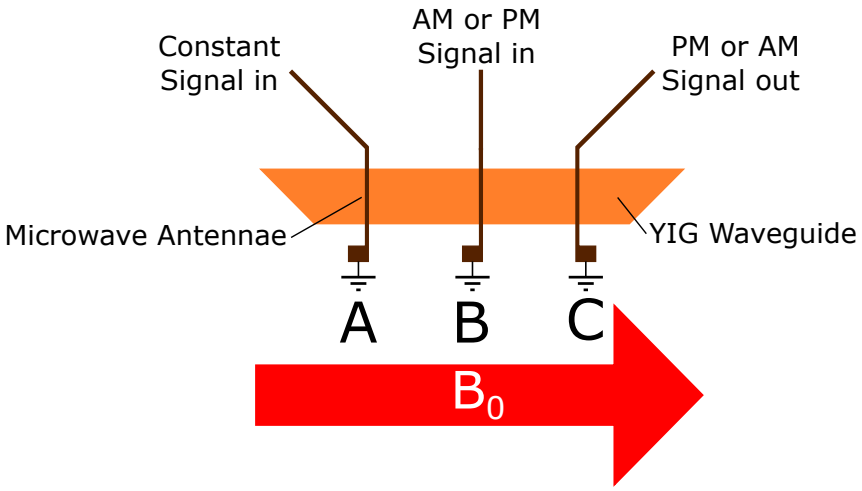


Figure 4.3: Diagram of the YIG waveguide used for the AM/PM interconversion experiments.

$\zeta = \pm 2$. As the data is AM encoded, the binary-0 state has a $\zeta = 0$, which has the same voltage in both traces. Figure 4.5 shows the original AM pulse, the continuous wave added ($\zeta = -1$ constantly), and the output PM signal ($\zeta = \pm 1$). This result shows that it is possible to convert AM magnonic signals to PM magnonic signals.

Figure 4.6 shows the input PM pulses for the PM/AM experiment. Again, the phase of the probe was tuned to maximize the voltage output of the first trace, and a second trace was plotted with the probe phase altered by 180°. As the PM encoding uses $\zeta = \pm 1$ in this case, it can be seen that a shift in probe phase of 180° inverts the binary-0 and binary-1 states, the equivalent of reading the NOT value of the signal. If the probe phase was somewhere between 0 and 180°, then the voltage would lie between the two extremal values seen in the plot.

Figure 4.7 shows the PM and continuous wave inputs and the output of the PM/AM converter. This plot demonstrates the device's successful functionality.

These plots together provide strong evidence of a successful implementation of the all magnon AM/PM interconverters proposed here. Below, some of the possible (less obvious) applications for the device are discussed.

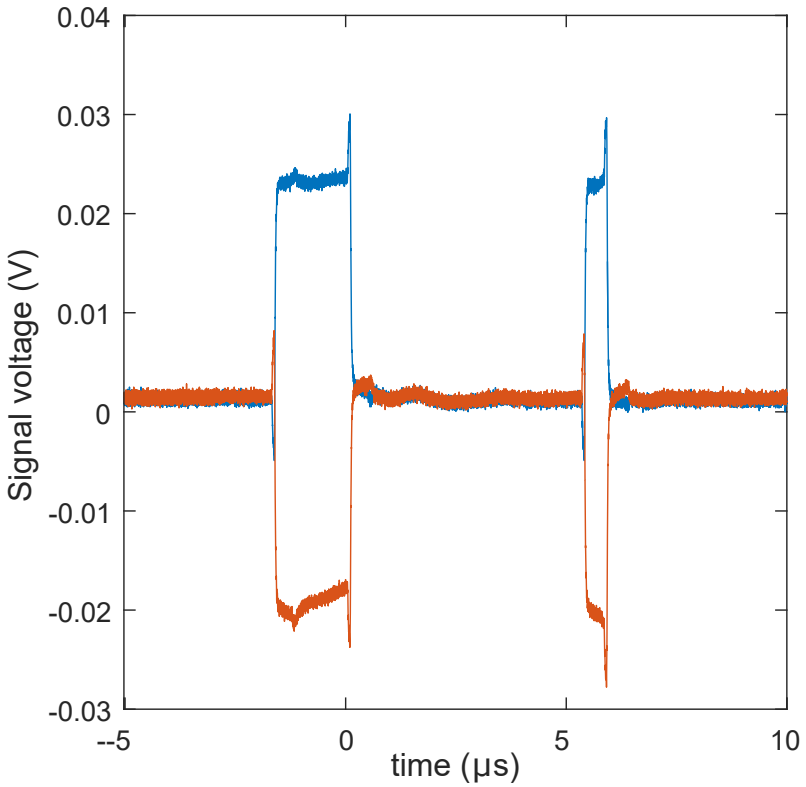


Figure 4.4: AM input signals, as measured with a heterodyne demodulator, with probe phases shifted by 180° between traces.

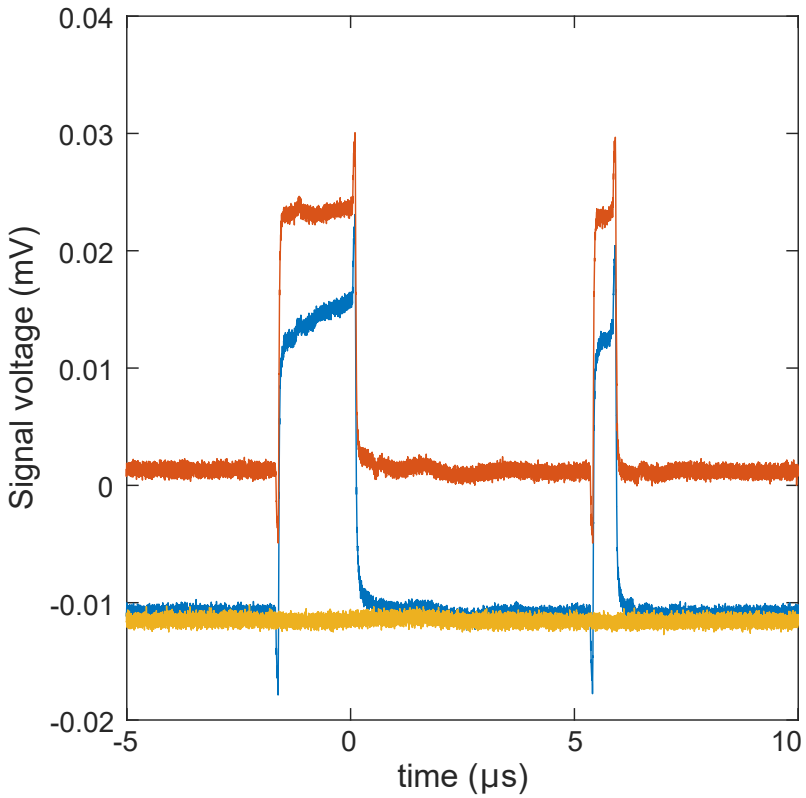


Figure 4.5: Demonstration of the AM to PM converter. The input AM signal is in red, the added 'continuous' signal is in yellow, and the output PM signal is in blue.

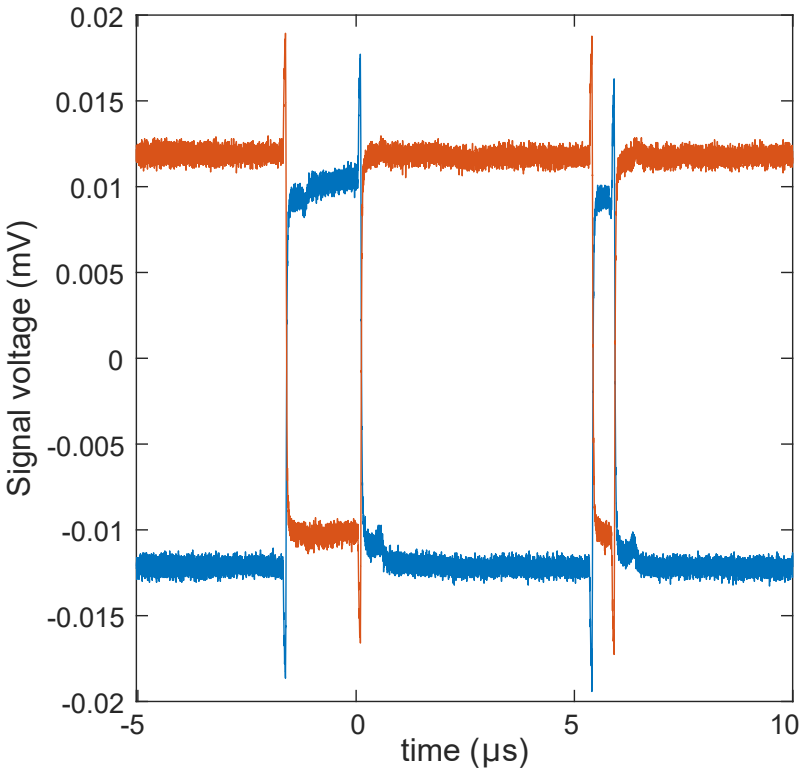


Figure 4.6: PM input signals, as measured with a heterodyne demodulator, with probe phases shifted by 180° between traces.

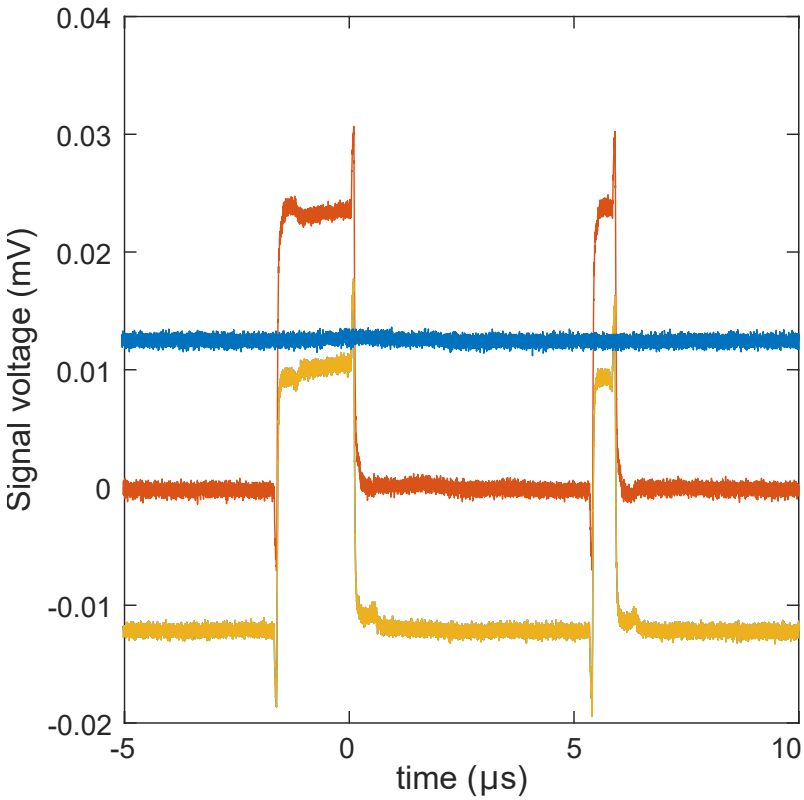


Figure 4.7: Demonstration of the PM to AM converter. The input PM signal is in yellow, the added 'continuous' signal is in blue, and the output AM signal is in red.

Devices	Input	Output
Majority Gate	PM	PM
Magnon Transistor	AM	AM
Magnon Amplifier	AM	AM
Magnon XOR Gate	AM ×2	AM
AM/PM converter	AM	PM
PM/AM converter	PM	AM
PM-output Amplifier	AM	PM

Table 4.1: Table of input and output encoding formats of existing (top section) and author-proposed (bottom section) magnonic devices.

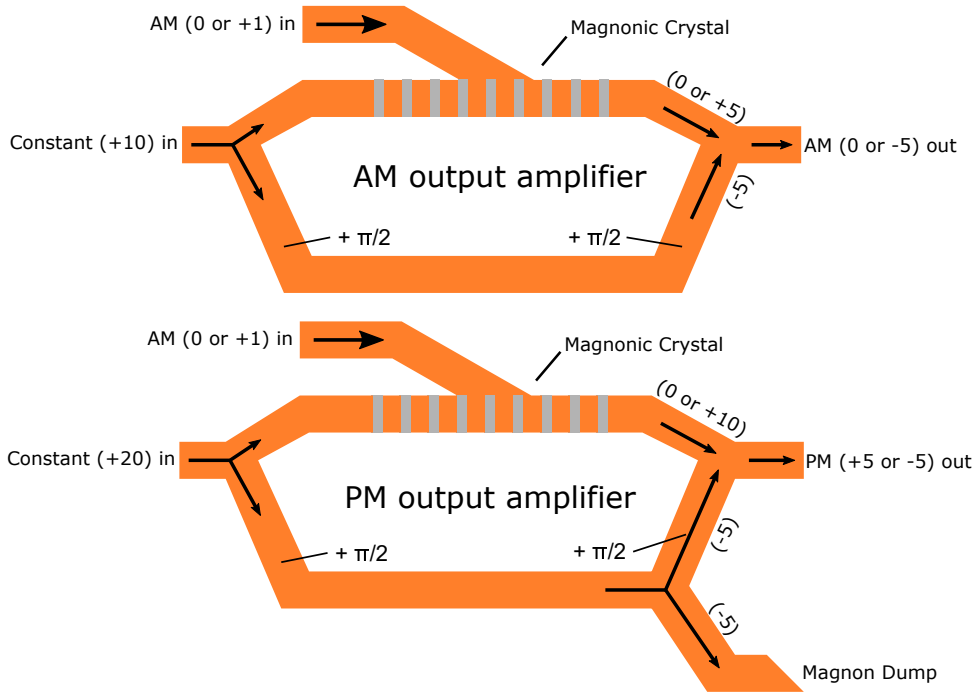


Figure 4.8: All-magnon amplifiers. a) Top: AM output amplifier [13], b) Bottom: New, modified amplifier that produces a PM output.

4.4 Potential application to other magnon devices

In Table 4.1, the input/output modulation methods for various established and proposed magnonic devices are outlined. One of the devices of interest here is the magnon amplifier proposed in reference [13], the workings of which were discussed in §1.3.1, and a diagram of which is reprinted in Figure 4.8a. It is now possible to follow through the workings of the device with the ζ notation in mind. As the amplifier currently works on AM encoding, all the signals are either $\zeta = 0$, $\zeta = 1$ or $\zeta =$'Large positive number'.

A modification to this arrangement which produces an amplified PM output is proposed, and presented in Figure 4.8b. Here, an additional fork is added to the lower branch, such that only half as much 'constant' signal returns to the recombination point. Now, when the gate is open, the top branch provides a $\zeta = +10$, while the bottom branch provides a $\zeta = -5$ giving an output of $\zeta = +5$, whereas, when the gate is closed, only the $\zeta = -5$ arrives at the output, and a PM signal has been produced. These numbers were calculated using a continuous input signal of $\zeta = +20$. This value was chosen to demonstrate the amplification potential, but in reality (so long as it is bigger than $\zeta = +4$) the amplitude is not overly critical.

This PM output amplifier has an additional foreseeable use, which is that it can be used to 'rectify' the AM signal produced by two input interference gates. For example, a PM XOR gate can be created by using the same architecture as the AM/PM converter, but using two data channels (of the same amplitude) with a 180° phase difference instead. This leads to a $\zeta = 0$ value for the 11 and 00 states, and $\zeta = \pm 2$ for 01 and 10. Using this as the input of the PM-output amplifier gives a PM signal out with the $\zeta = \pm 1$ binary states corresponding to that of an XOR gate, uncontaminated by $\zeta = 0$ states. By effectively discarding the phase information of the multi-valued input, the input has been rectified into a two-value output, which can then be processed by subsequent magnonic components.

4.5 Summary of AM/PM inter-converters

To summarise, a simple, new device that is able to convert between the two most common data encoding methods used in magnon computing today has been proposed. The principle of the device has been demonstrated electronically and magnonically, and some examples of how the device could be integrated with existing devices to provide new functionality (as well as new circuits) has been provided.

Chapter 5

Magnon Multiplexing

5.1 Introduction

As mentioned in §1.3, one of the promised advantages of magnon-based computing over conventional CMOS devices is the ability to utilize individual components to process information from several different data channels simultaneously. To fully exploit this, a method of combining, processing, then separating multiple magnonic data streams, without loss or corruption of any of the signals must first be developed.

Multiplexing is commonly encountered in the world of telecommunication [55], where multiple signals with differing carrier frequencies are transmitted down single waveguides, such as simple wires or optical fibres. The advantage here being that a single piece of hardware — the waveguide — can be used to propagate multiple digital signals simultaneously. Wave-based computing allows for the existence of logical devices based on the interference of waves of a single frequency. These devices, if fed with a multiplexed signal, provide the potential for a single device to perform the same computational process to multiple data streams concurrently. The final (and most exciting) feat offered by wave-based computing, can be found by combining multiplexing with wave-based devices, as in the majority gate (see §1.3.1).

As mentioned in §1.3.1, the majority gate is able to operate as either an AND or an OR gate depending on the binary state of the third input. Operating the gate in conjunction with a multiplexer would allow multiple frequencies of signal to be

processed at the same time, but also allow the third input to differ for the various frequency channels. This has the impressive result of performing *different* logical operators on different data streams simultaneously using a single device. This has the potential to greatly reduce the footprint of wave-based devices, and this ability also paves the way for wave-based Field Programmable Gate Arrays.

For the reasons outlined in §1.3, magnons are a good candidate for developing the wave-computing paradigm; however, their multiplexing potential has not yet been explored. In this chapter, the viability of multiplexing and demultiplexing multiple signals in a magnonic waveguide is investigated. Two different demodulating methods are considered, and attempts are made to characterise the results in terms of the number of data channels that can successfully propagate simultaneously, and the maximum rate at which information can be transmitted.

5.2 General experimental arrangement

In §4.1 the idea that data can be encoded in magnon streams via either amplitude modulation (AM) or phase modulation (PM) was introduced. The symbol ζ was also introduced as a convenient way of discussing binary data encoded using either of the two methods. In this section, the experimental arrangements used to generate, combine, and separate the data streams used for the multiplexer experiments is presented.

To investigate the extent to which it is possible to multiplex magnonic signals, a simple transmission line setup was constructed, and is shown in Figure 5.1. This comprises three key sections: signal generation, signal transmission, and signal detection. Each of these sections will be looked at in closer detail below. Transmission is discussed first, as it is the simplest element, and one that was not varied during the course of the experiment.

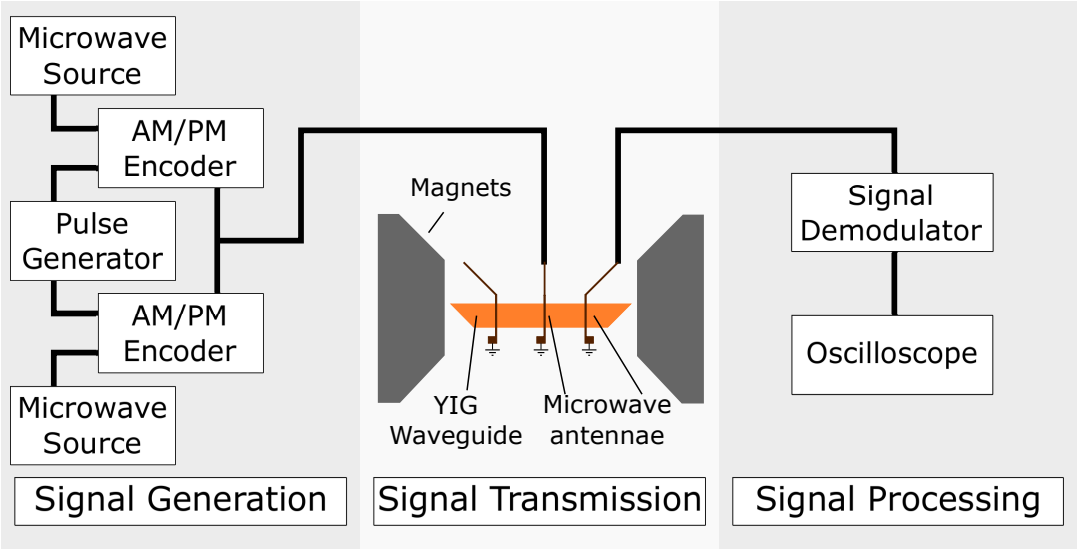


Figure 5.1: Schematic of the basic multiplexing experiment. Microwaves are encoded with AM or PM information, and then added together to create a multiplexed signal. A microwave antenna is used to transmit the information down the YIG waveguide, while the applied magnetic field ensures the magnons can propagate. The signal is detected by the second antenna, and can then be demodulated using either the interferometer or the heterodyne method.

5.2.1 Signal transmission

Electrical signals arriving at the device input were converted to magnonic signals in the waveguide via the use of a microwave antenna positioned close to the YIG waveguide, as described in §1.2.4. The magnons propagate down the waveguide a distance of 2 mm to a second antenna. This antenna, by a similar process, converts the magnon signal back into an electrical signal, ready for processing. Radio frequency direct coupling between the two antennae was recorded at a transmission level of −30 dB when no magnetic field was applied to the waveguide (and thus no magnons were flowing). This is a much lower transmission level than that of a typical magnon signal, which is usually of the order of −15 dB. These measurements were made using a network analyser.

5.2.2 Signal generation

Signals were generated for these experiments using three different microwave sources: HP-8671A, HP-8672A and a Hittite HMC T-2220. These continuous wave sources

were modulated using the same method as in §4.3, using microwave splitters and microwave switches (Mini circuits ZFRSC-42 and HP 33144A). The microwave switches were driven with an in-house made pulse generator, generating 5V pulses with durations of the order 250 ns. The microwave switches as part of the AM/PM encoder circuit seen in Figure 4.2 were then able to encode the magnons with either AM or PM information. Once the information had been encoded into each channel, the two frequency channels were joined with a splitter, before being passed to the transmission line.

For the sake of clarity, it is highlighted that, in this experiment, the signals have been multiplexed into a single data stream before being transmitted. This does not, however, reduce the validity of the study, as the multiplexed signal is still propagated within the magnon channel. It does, however, mean that other non-magnon related non-linear effects may appear. (See §5.3.7).

Methods of creating AM and PM encoded microwave signals have been previously explored in §4.3. The same method is used here, though it is highlighted that whenever any of the frequencies being used was modified, the PM encoder setup needed tweaking such that the phase and amplitude of the bypass signal was correct.

An alternative PM modulation method was available for use, which was a voltage-controlled variable phase shifter. This device is able to shift the phase of a microwave stream anywhere between 0 and 180°, dependent on the voltage applied to the control terminal. Although this provides more flexibility in terms of control over the output phase difference, the devices only work over a limited range of frequencies. As the PM paradigm only requires a 180° shift, the modulation device of §4.3 is sufficient, more reliable, and more versatile with respect to frequency range.

5.2.3 Signal detection and demodulation

Once the transmitted data stream has been converted from a magnonic signal back into an electrical signal, it is ready to be processed. Two methods of separating the data streams and extracting the original binary data were investigated: het-

erodyne downconversion, and interferometry. As the heterodyne downconversion experiments were much more successful than the interferometer based method, the heterodyne downconversion results will be presented and discussed first.

5.3 Heterodyne downconversion

5.3.1 Heterodyning theory

Heterodyne downconversion, or Heterodyning, is a signal processing technique first developed in 1901 by Reginald Fessenden. It is a process in which two signals are multiplied together, which results in two different signals with frequencies that are the sum and difference of the original two, as can be seen in Equation 5.1[56]

$$A\cos(\omega_1 t) \times B\cos(\omega_2 t + \phi) = \frac{1}{2}AB\left(\cos(\omega_1 t - \omega_2 t - \phi) + \cos(\omega_1 t + \omega_2 t + \phi)\right). \tag{5.1}$$

This is the same process by which the lock-in amplifier operates (See §3.1.3). It is commonly used as a method of measuring the frequency of signals that would otherwise be unmanageable, as when the two frequencies are similar, one of the output signals will have a low frequency which can be readily manipulated (and measured) by electronics, once the second, much higher frequency has been filtered out. (For the majority of the experiments below, an in-house-made 28.5 MHz low-pass filter was used).

When the two input frequencies are exactly the same, the output signals take the form:

$$A\cos(\omega t) \times B\cos(\omega t + \phi) = \frac{1}{2}AB\left(\cos(-\phi) + \cos(2\omega t + \phi)\right). \tag{5.2}$$

Once the higher frequency term has been filtered out by a low-pass filter, only a constant DC term with a ϕ dependence is left. If this ϕ is switched between the two values used in the phase modulation encoding (0° and 180°), then the output

is a DC signal that switches between $\pm\frac{1}{2}AB$ Volts, thus enabling the decoding of the PM signal. If instead it was B that was modulated between 0 and B (the AM encoding), then the output signal would toggle between a DC signal of 0 or $\frac{1}{2}AB$, again allowing for the extraction of the digital information. For the experiments below, this operation is performed by a mini circuits ZEM-4300 multiplier.

When a signal comprises multiple different frequencies — such as the case when several data channels are multiplexed together — a generalized form can be presented,

$$\begin{aligned} &\sum \left\{V_i \cos\left(\omega_i t + \phi_i\right)\right\} \times V_{\text{Probe}} \cos\left(\omega_{\text{Probe}} t\right) = \\ =&\sum \left\{ \frac{1}{2} V_i V_{\text{Probe}} \left(\cos\left(\left(\omega_i - \omega_{\text{Probe}}\right) t + \phi_i\right) + \cos\left(\left(\omega_i + \omega_{\text{Probe}}\right) t + \phi_i\right)\right)\right\}. \end{aligned} \tag{5.3}$$

Again, the DC signal corresponding to a frequency match can be seen, but so can contributions with potentially low frequencies coming from the other channels. The strength of the filtering and the closeness of these other channels is therefore a relevant consideration when contemplating the separation of data channels in the multiplexed signal.

The custom 28.5 MHzRC filter For the majority of the heterodyning experiments, a custom made low-pass filter was used to remove unwanted frequencies, the workings of which are outlined here. For a more detailed discussion of RC low-pass filters, see §3.1.3.

The cut-off frequency of the custom-made filter was chosen to be 28.5 MHz as it provides a balance between a short time constant (and thus rapid response time), and an appropriate frequency response. The filter consisted of an 8.2 Ω resistor, and a 680 pF capacitor in a voltage divider arrangement (with the capacitor going to ground). The equation governing the voltage throughput is therefore

$$V_{\text{out}} = V_{\text{in}} \frac{1}{1 + j\omega RC} = V_{\text{in}} \frac{1}{1 + j\frac{f}{28.5\,\text{MHz}}}.$$

The transmission spectrum of the filter is presented in Figures 5.2a and 5.2b,

where Figure 5.2a shows the transmission from $0 - 150\,\text{MHz}$, and 5.2b shows the transmission from $0 - 1.5\,\text{GHz}$. As the filter does not effectively filter out the higher frequencies, a commercial 550 MHz low-pass filter was added after the custom filter. The transmission spectrum for this arrangement can be seen in 5.2c. In all of these plots, some useful data points have been marked on the traces.

5.3.2 Existing signal processing techniques

Although heterodyning was first described over 100 years ago, it is still a key element of nearly all modern radios today [57]. Modern radios often use a specific type of heterodyning method known as the 'superheterodyne' principle (supersonic heterodyne). This technique uses an ω_{Probe} that is on the order of 500 kHz-10 MHz higher than the various radio carrier frequencies. After heterodyning, this leads to a signal in which the many modulated channels have frequencies clustered around the high kHz/low MHz range. (455 kHz, 10.7 MHz, and 38 MHz are commonly used as the intermediate frequency for AM radio, FM radio, and TV signals respectively [57]). At this frequency range, highly selective amplifiers or very narrow band-pass filters are available that can be used to remove nearly all of the undesired frequencies (These can be as narrow as 10 kHz for AM radio [58]). Once filtered, the remaining signal can then be demodulated (e.g. by a diode for an AM signal) to extract the information encoded on the carrier wave. By changing the value of ω_{Probe}, the user is able to 'tune' the radio to their desired station by shifting which channel's frequency coincides with the pass band of the filter or amplifier.

Modern radios tend to use either amplitude modulation or frequency modulation, whereas the experiments in this thesis are also interested in phase modulation. Superheterodyning does not immediately allow for the measurement of PM encoded information, unlike the case when the signal is heterodyned to DC, as in Equation 5.2. Even though heterodyning to DC and using low-pass filters may restrict the number of channels that can be transmitted (see §5.3.4), it provides an easy way of directly measuring the PM encoded information which is critical for magnon com-

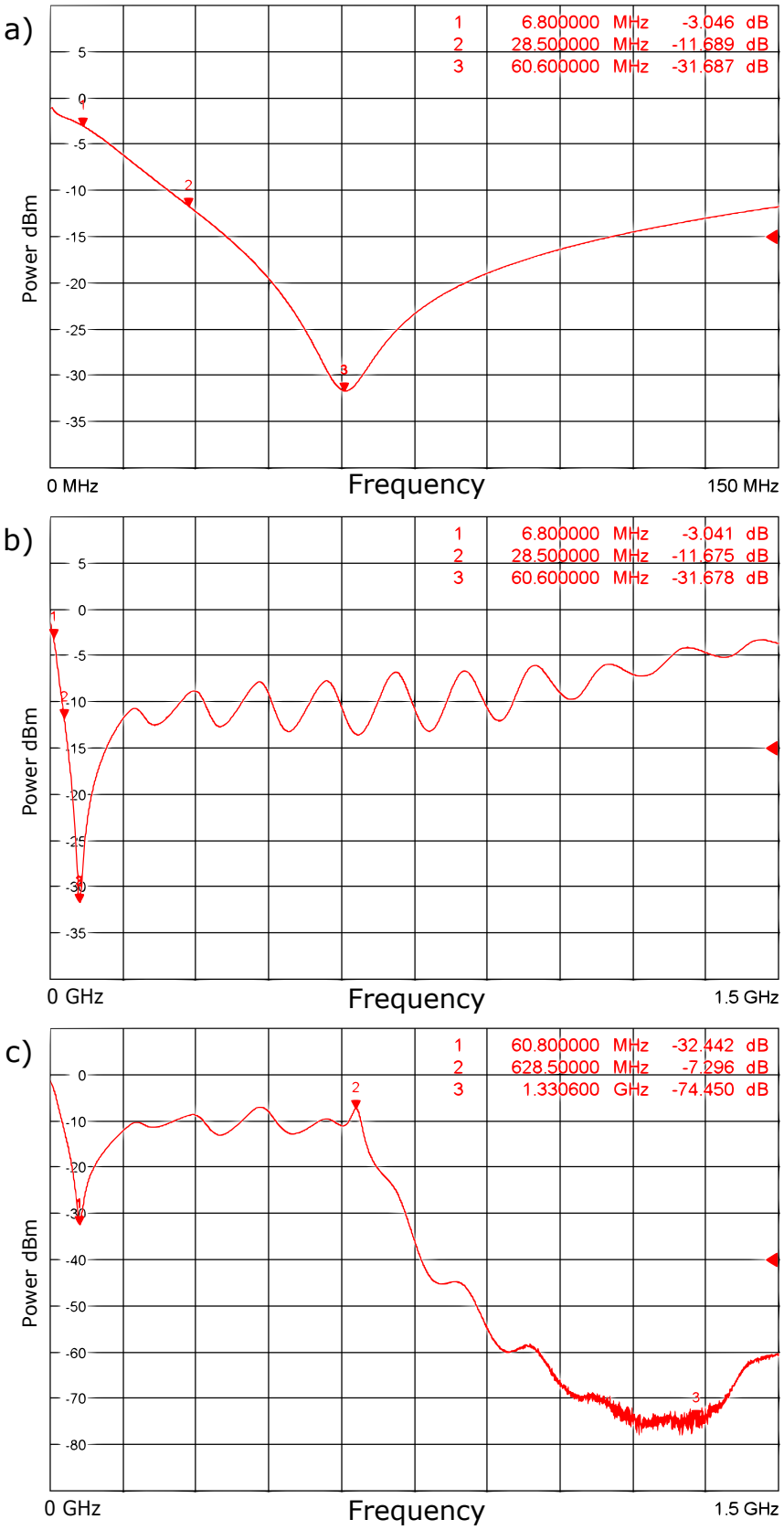


Figure 5.2: Low-pass filter transmission properties, measured on a network analyser: a) The custom 28.5 MHz filter over a short frequency range b) The custom 28.5 MHz filter over a wider frequency range c) Custom 28.5 MHz filter followed by a commercial 550 MHz low-pass filter over the wider frequency range.

puting. Along with the fact that heterodyning to DC uses less electronics, it is for this reason that DC was used as the intermediate frequency in the experiments.

The possibility of applying more advanced signal processing techniques to the experiment (such as superheterodyning) will be discussed in §6.2.2.

5.3.3 Heterodyning experimental results

Before the question of how many signals can be demultiplexed by the heterodyne demodulator can be answered, it must first be shown that the heterodyne demodulator functions as expected, and that it is physically possible to simultaneously transmit multiple magnon signals down a waveguide without excessive crosstalk. This was done by creating an input signal consisting of two multiplexed data channels, transmitting them through the magnonic waveguide, and then demultiplexing the output signal, as described below.

Input signals

The investigation began by observing the form of the original electrical data signal, created by sending two different pulse trains into two separate encoder circuits with two different frequencies. Encoders were calibrated for each new frequency used. The shape of the two pulses was measured by connecting the output of the signal generation circuits to a crystal detector, followed by an oscilloscope. The AM and PM output voltage measured in this way can be seen in Figure 5.3.

In the AM plot, the shape of the two pulses can be seen, though there is no indication of the frequency of either. In the PM plot, a constant voltage is seen for the majority of the trace, which is what might be expected, given that PM encoded data should have a constant amplitude. Some oscillations caused by switching spikes can also be seen on one of the pulses. These oscillations are attributed to the fact that one of the high-pass filters used may have had too low a cut-off frequency (thus permitting some transmission of the switching spike into the system), or, that the specific switch used happens to have a spike component close to 3.2 GHz, such that

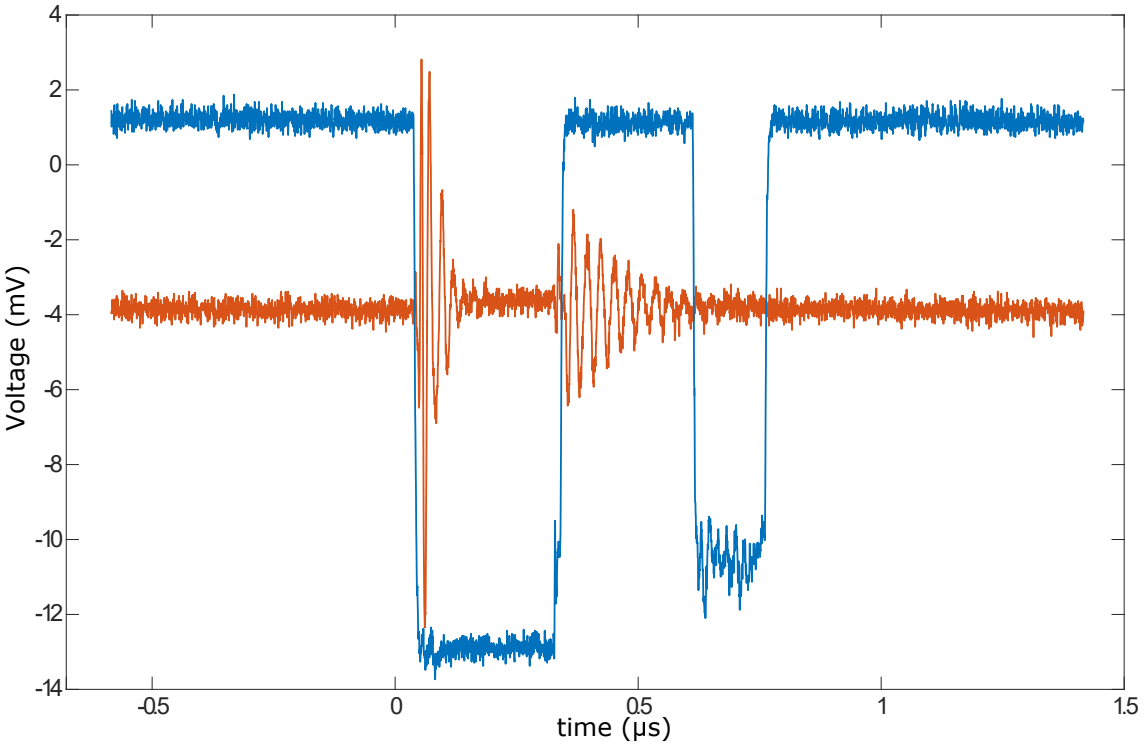


Figure 5.3: Input signal pulse shapes for the heterodyning experiments as measured by a crystal detector/diode. The AM signal is in blue, and the PM signal is in red.

the beat pattern is visible.

In §4.3 it was demonstrated that the heterodyne demodulator is capable of demodulating AM and PM signals encoded in a single frequency. Figures 4.4 and 4.6 provide examples of the sort of signal outputs that are desirable from a demultiplexed signal, when the probe is set to the appropriate frequency for each channel.

Heterodyning Proofs of concept

AM without magnons The efficacy of the heterodyne demodulator for a multiplexed signal is demonstrated for the purely electrical AM case in which the magnon stage has been bypassed. This is shown in Figure 5.4. For this experiment, the two frequency channels were operating at 3.15 and 3.25 GHz. Here it can be seen that when the probe frequency is set to match each of the signal frequencies, it is possible to extract the correct binary data for each channel.

There are a few features of this plot that are noteworthy. It is observed that the switching spike at the tail end of the first pulse contains frequency components

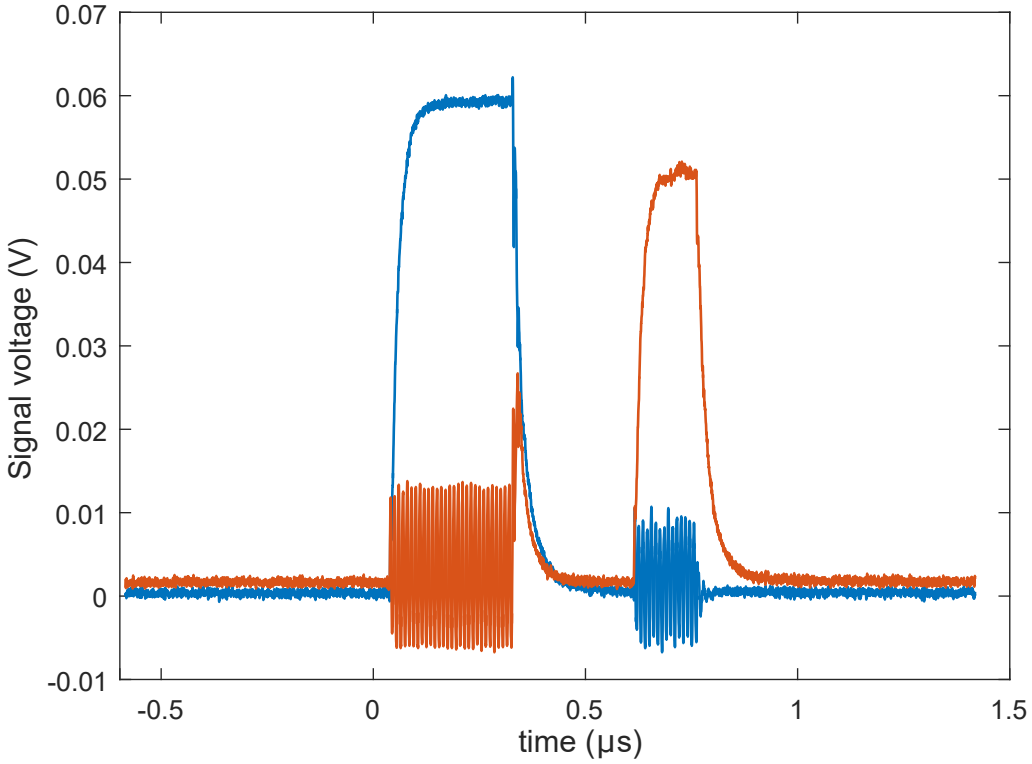


Figure 5.4: Heterodyne demodulation of AM electrical signals at 3.15 GHz and 3.25 GHz.

of both frequencies, as it appears in both traces, whereas the second pulse does not. This provides additional insight as to the potential origin of the non-constant voltage seen in Figure 5.3.

A 100 MHz signal that coincides with the position of the other pulse for each of the two frequency channels is also observed, and is caused by the beating between the probe at one frequency and the data stream of the other. The amplitude of this oscillation has been greatly diminished by the 28.5 MHz low-pass filter. This should enable the original, uncompromised data signals to be retrieved by introducing an appropriate cut-off voltage threshold in the processing circuitry. Filtering is discussed further in §5.3.4.

It is noted here that the baseline voltages for the two traces are also not exactly the same, and differ by 1.5 mV. This is not overly significant here; however, when magnons are introduced and the output voltages decrease in magnitude, this discrepancy becomes more noticeable.

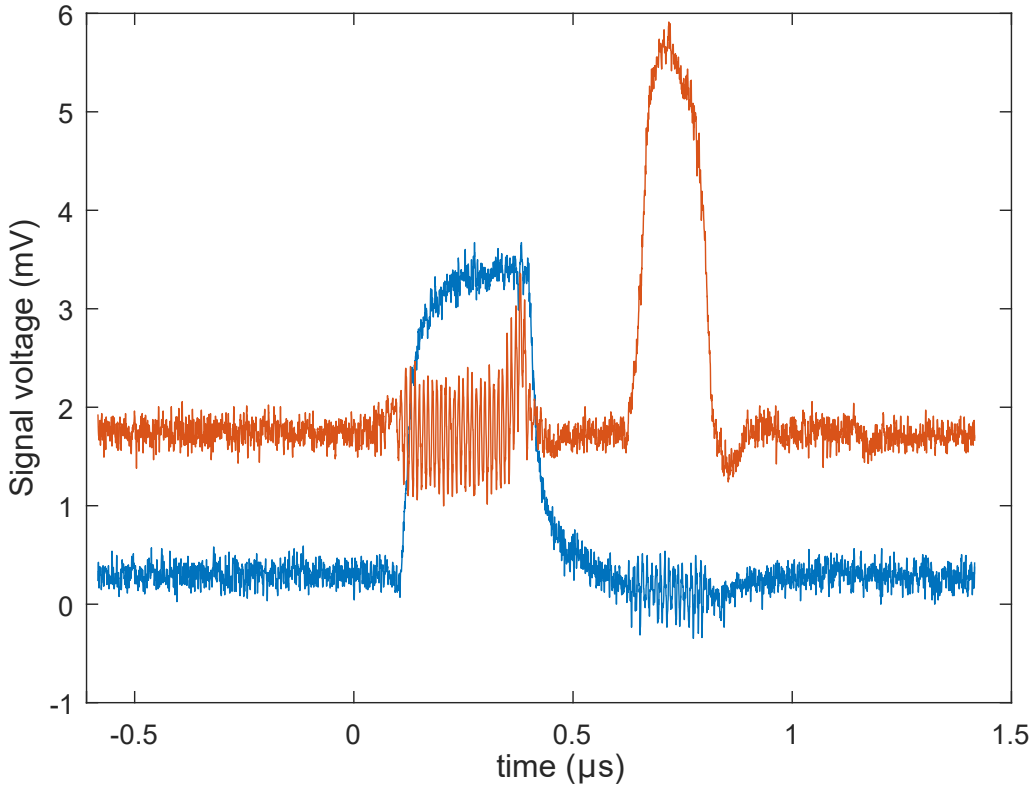


Figure 5.5: Heterodyne demodulation of AM magnon signals at 3.15 GHz and 3.25 GHz.

AM with magnons Having demonstrated the functionality of the AM Heterodyne demodulator for the electrical case, the effect of reintroducing the magnon transmission line into the experiment in its backward volume mode was investigated. The external $\boldsymbol{B}$ field was tuned to ensure that the amplitude of the transmitted signal for each of the frequency channels was similar. Figure 5.5 shows the same plot as in Figure 5.4 for the case when the magnon waveguide has been reintroduced.

There are many similarities between the two plots. The baseline voltages of the two frequencies differ by 1.5 mV, 100 MHz beat patterns can be seen in each trace at the location of the other pulse, and the first pulse switching spike is visible in both frequency channels. The main noticeable differences (apart from the attenuation of the signals) are the slight distortion of the second pulse, and the slight time delay between the with-magnon and without-magnon traces. The time delay is a natural consequence of adding a transmission line element into the experiment, as the magnons have a finite speed, whereas the pulse distortion is to do with the dispersion of the YIG waveguide. The effect of the dispersion on the available

waveguide bandwidth will be discussed further in §5.3.4.

These plots demonstrate that it is possible to multiplex AM signals within a magnonic waveguide, and extract them again using the heterodyning method.

PM Heterodyne with and without magnons The plots for two frequency channels, 3.15 and 3.25 GHz, are presented for the with-magnon and without magnon arrangements for the case of PM encoded signals, demodulated with the heterodyner. These can be seen in Figures 5.6 and 5.7. Both plots feature the same features as in the AM case above: the switching spike, the slightly distorted signal, and the same 100 MHz noise, though across the entire trace this time, as might be expected given that the signals are now continuous wave (in amplitude). It is noticeable however, that the amplitudes of the two pulses are different in the with-magnon case. This is an effect of the choice of the applied $\boldsymbol{B}$ field and the dispersion of the waveguide, and will be discussed further in §5.3.4. These plots do however demonstrate that multiplexing PM signals within the magnonic wave guide is possible when using the heterodyne method of extraction.

5.3.4 Bandwidth and Filtering

Having demonstrated the viability of using heterodyne downconversion as a method for demultiplexing two AM or PM encoded data streams that have been transmitted through a magnon waveguide without excessive cross-channel crosstalk, it is now desirable to investigate the maximum number of data channels that can propagate simultaneously.

Up to this point, the heterodyning experiments have all been performed using two frequency channels, separated by 100 MHz. A 28.5 MHz low-pass filter has also always been used. By investigating the effect of modifying the signal spacing and filter cut-off frequency, an estimate of the optimal configuration can be made.

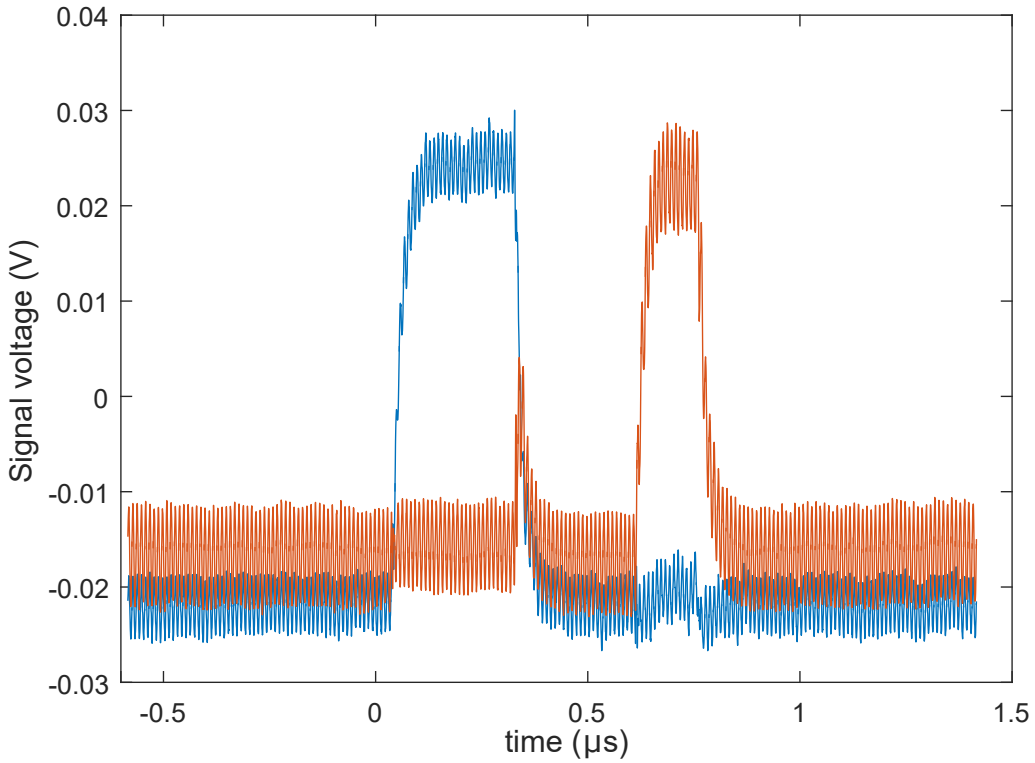


Figure 5.6: Heterodyne demodulation of PM electrical signals at 3.15 GHz and 3.25 GHz.

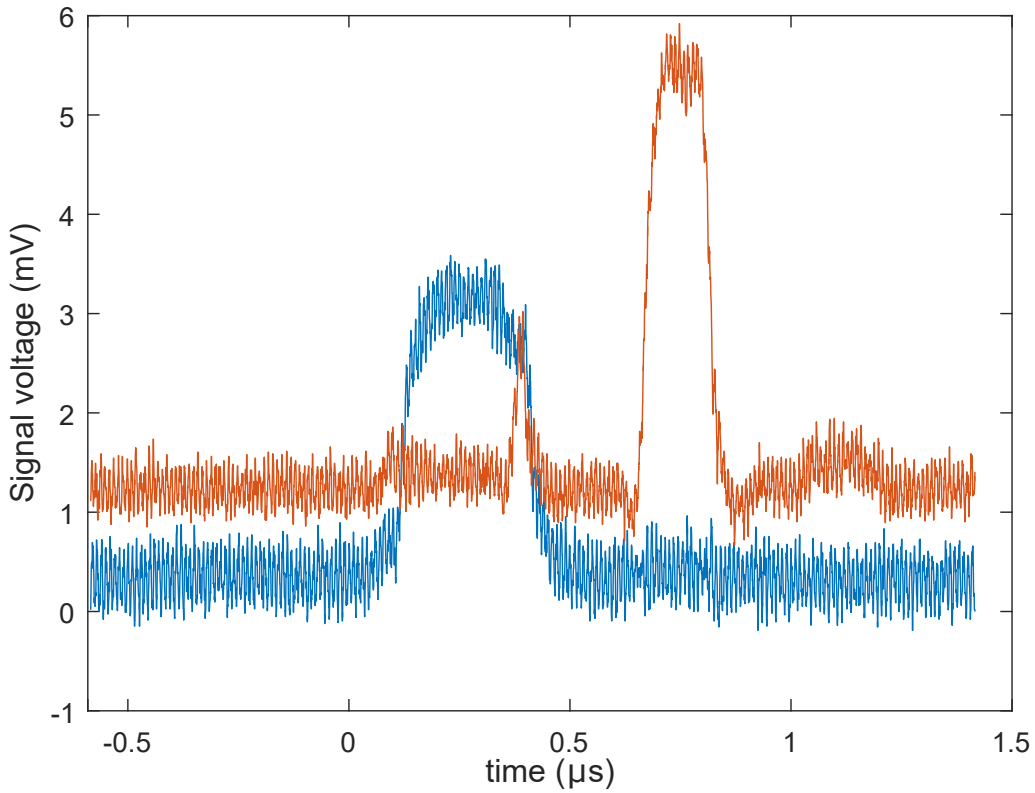


Figure 5.7: Heterodyne demodulation of PM magnon signals at 3.15 GHz and 3.25 GHz.

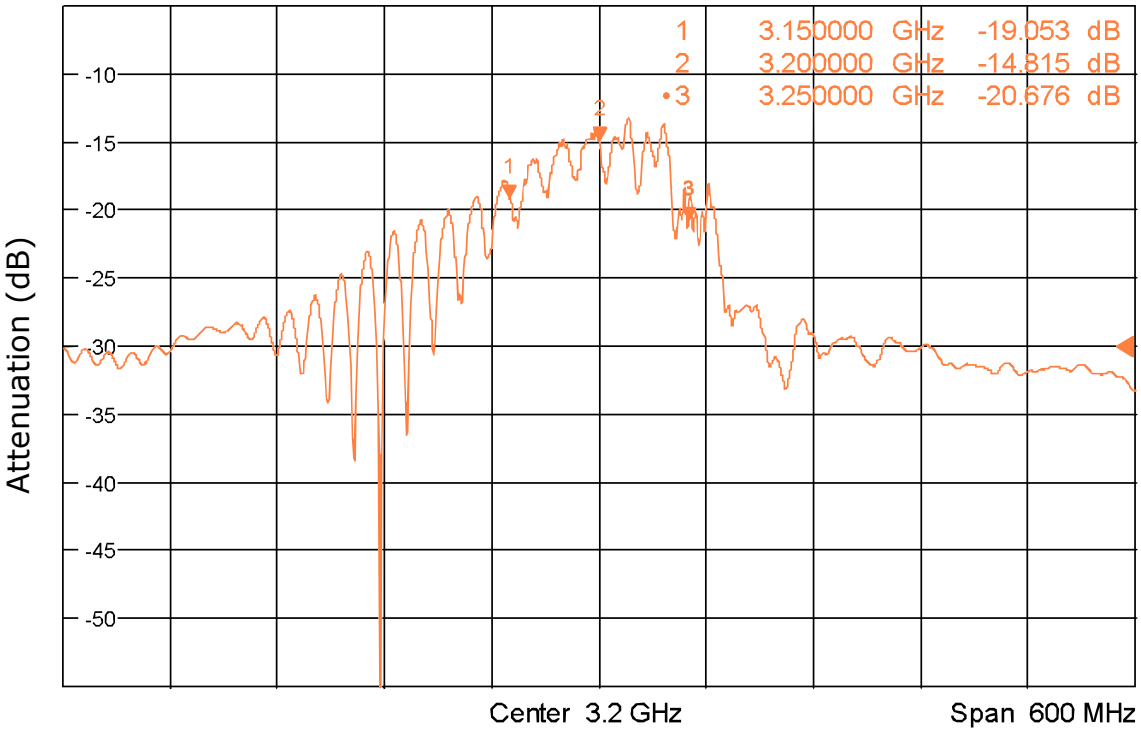


Figure 5.8: Transmission spectrum through the YIG waveguide in its backward-volume mode. As the group velocity of backward-volume magnons is negative, the higher the frequency, the lower the $\boldsymbol{k}$. The high frequency cut-off is therefore attributed to FMR magnons ($\boldsymbol{k} = 0$). The gradual decrease in signal strength with decreasing frequency is due to the antenna efficiency, which decreases with increased $\boldsymbol{k}$, as discussed in §1.2.4. The oscillations in the spectrum occur due to constructive and destructive interference between the transmitted magnons and the direct electromagnetic coupling between the launching and detecting antennae.

Bandwidth of the Waveguide

The first thing to look at when considering how many channels can be utilized, is the size of the available 'real estate' in the magnon waveguide. As mentioned in §1.2.4, the limiting factor in this system is the range of frequencies the antenna is able to excite, given the dispersion of the waveguide and the applied field. Luckily, this range can be easily measured using a network analyser to look at the signal loss across the waveguide over a broad range of frequencies with a fixed applied field. This can be seen in Figure 5.8.

For all the frequencies plotted, it can be seen that there is signal transmission with at least -30 to $-35\,\mathrm{dB}$ loss. This is the antenna-antenna direct coupling mentioned in §5.3.7. To overcome this unwanted background signal, the magnon signals must be significantly stronger than this. If a threshold of around $-20\,\mathrm{dB}$

is used, there is a range of about 100 MHz over which the magnon signal is strong enough to be useful.

As demonstrated in the proof-of-concept results, it is possible to multiplex two signals at the extremes of this frequency range. The question is now how many signals can fit in between? How close can two channels be before they are too close? And how is this affected by the strength of the low-pass filter?

How close can the channels be in frequency space?

To observe the effects on the integrity of the data streams when the frequency channels become 'too close' with respect to the frequency of the low-pass filter, output traces are recorded for a range of frequencies as the channel separation is set to 100, 50, 25, and 10 MHz. The filter is kept at 28.5 MHz for the duration of this experiment, giving insight into the cases where the separation is much greater than, greater than, equal to, or less than the filter's -3 dB point.

Figures 5.9 and 5.10 are 2D plots for the signal outputs for AM and PM encoded magnons with frequency channels separated by 100 MHz. These plots were created by recording voltage/time traces (as in Figure 5.5) using probe frequencies ranging from below to above the data channel frequencies, 3.15 and 3.25 GHz. Each horizontal black line represents such a trace, and the colour map represents the signal voltage. Comparing the lines corresponding to 3.15 and 3.25 GHz in Figure 5.9 to the traces in Figure 5.5 should assist the reader in interpreting these plots. These plots (along with Figures 5.13, 5.14, 5.15, and 5.16) are useful as they help visualise the width of each data channel in frequency space, and show the effects of bringing two channels 'too close together'.

For the AM plot, only the white regions are significant, as they represent times when an AM signal is detected. In this case, the pulses are clearly distinguishable, and the middle frequency of 3.20 GHz has very little signal. By looking at the periodicity of the light and dark banding for frequencies close to that of the two data channels, the frequency of the beating can be calculated. As expected, these

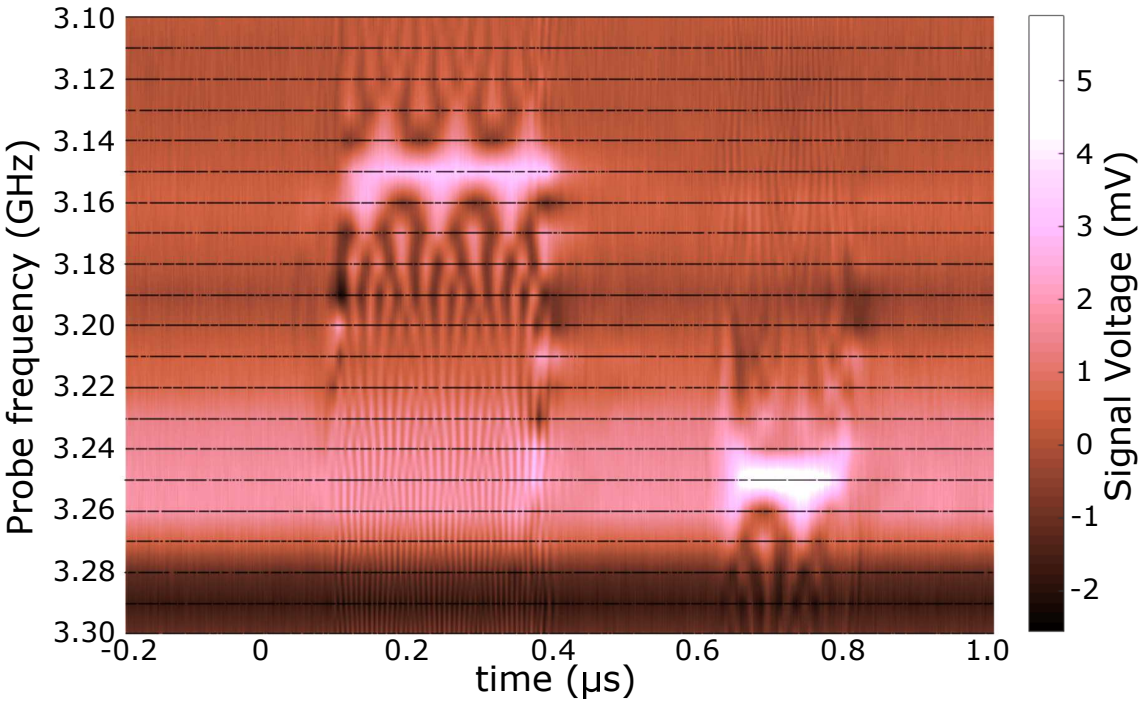


Figure 5.9: 2D plot of heterodyne demodulated AM magnon signals, 100 MHz apart, at 3.15 GHz and 3.25 GHz. Each horizontal line is a trace recorded using the probe frequency shown on the y axis. Signal voltage is indicated by the colour map.

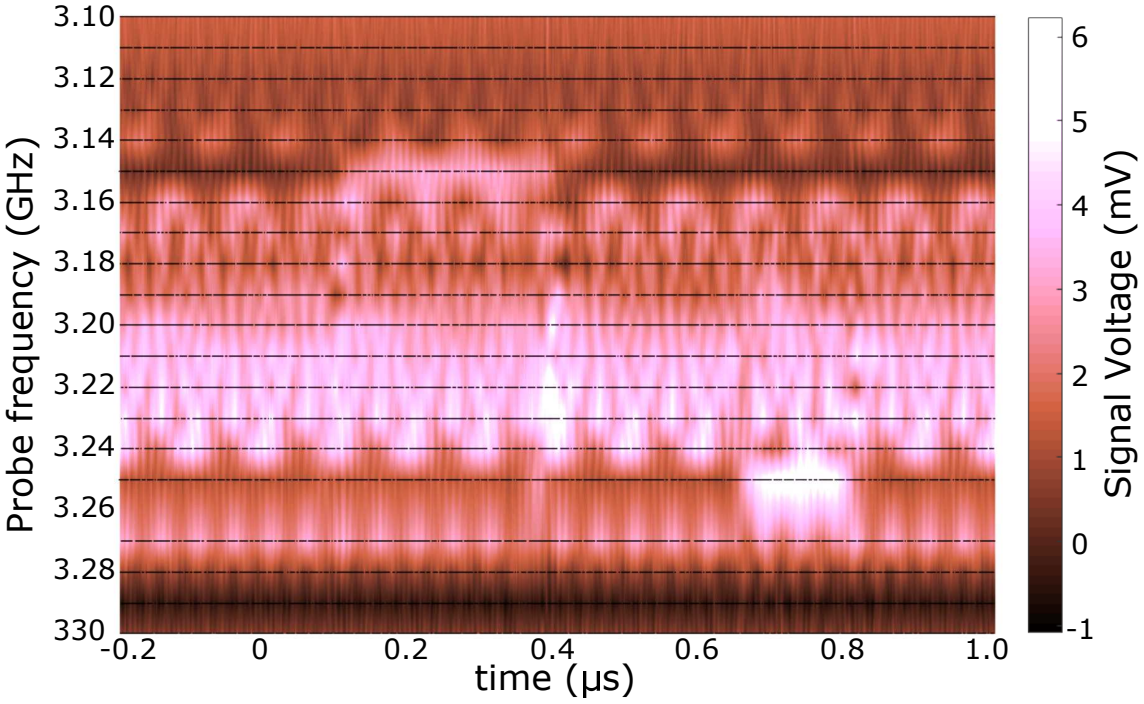


Figure 5.10: 2D plot of heterodyne demodulated PM magnon signals, 100 MHz apart, at 3.15 GHz and 3.25 GHz. Each horizontal line is a trace recorded using the probe frequency shown on the y axis. Signal voltage is indicated by the colour map.

frequencies are just the difference between the probe and signal frequencies and represents the main source of 'crosstalk' that needs to be combatted when fitting data channels close together. The amplitude of these oscillations (represented by the contrast between the peaks and troughs) can be seen to decrease the further the probe frequency is away from the channel, and this decay length (in frequency space) is directly related to the filter strength.

Important colours in the PM case are regions at the extremes of the colour scale, as they represent phases that are $\zeta = \pm 1$. When the probe frequency is set to one of the data channel frequencies, the locations of the pulses are clear, as the area changes from black/dark red to white/light red. For the intervening frequency of 3.20 GHz, the trace is almost entirely monochrome. This makes sense, as the lowest frequency component coming out of the heterodyner at this frequency should be around 50 MHz, which is attenuated by the 28.5 MHz filter, and therefore leads to a nearly constant output voltage close to 2.5 V.

Signal-to-crosstalk ratio The signal-to-crosstalk ratio is measured by observing the voltage change between the binary-0 and binary-1 states of the AM and PM signals, and dividing it by the magnitude of the crosstalk from the other channel. Voltage traces for signals at 3.15 GHz, where the second channel frequency is 10, 25, 50, and 100 MHz higher are plotted in Figures 5.11 and 5.12, for the AM and PM cases. The signal and crosstalk data is presented in Table 5.1. This data was collected by fitting a square wave, and a sinusoidal function to the traces in Figures 5.11 and 5.12, and using the fitting parameters (with their 95% confidence bounds) as the signal size and crosstalk amplitude. The error in the signal-to-crosstalk ratio was calculated by adding the fractional errors of the signal and the crosstalk in quadrature.

For the case of amplitude modulation, the cut-off signal-to-crosstalk ratio that could be made to work is one. This is because a voltage cut-off threshold just above the crosstalk level can be applied electronically to extract the data, so long as there is still signal above this level. For the phase modulated case, the cut-off ratio is two,

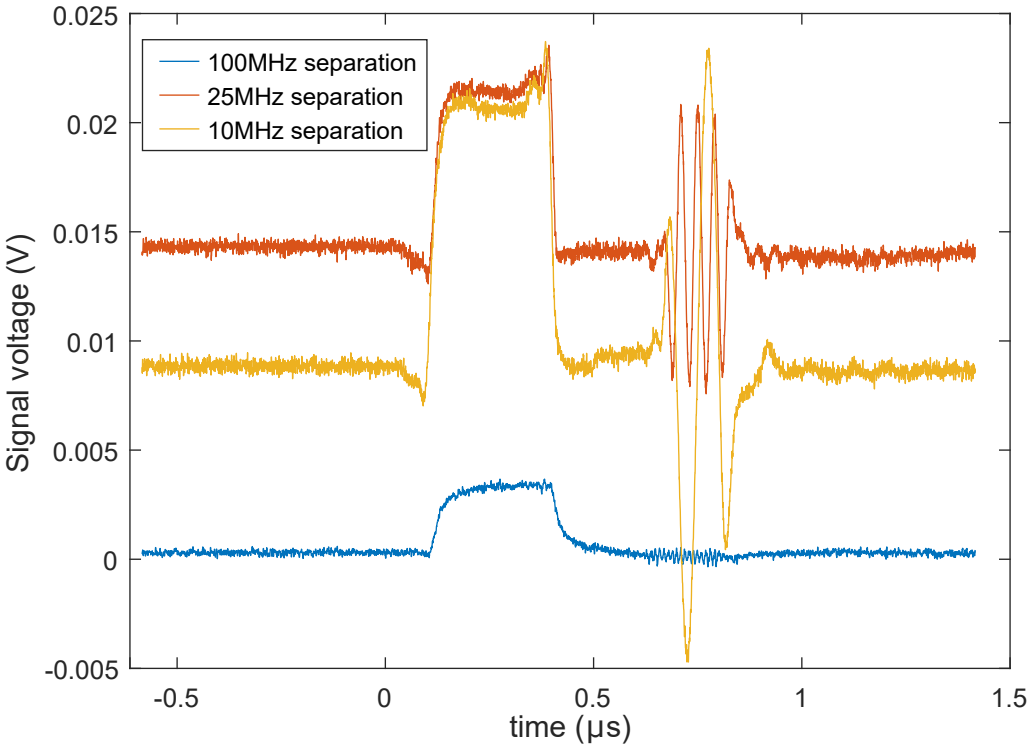


Figure 5.11: Heterodyne demodulation of AM pulses at 3.15 GHz, where a second signal exists at a frequency that is 10, 25, and 100 MHz above.

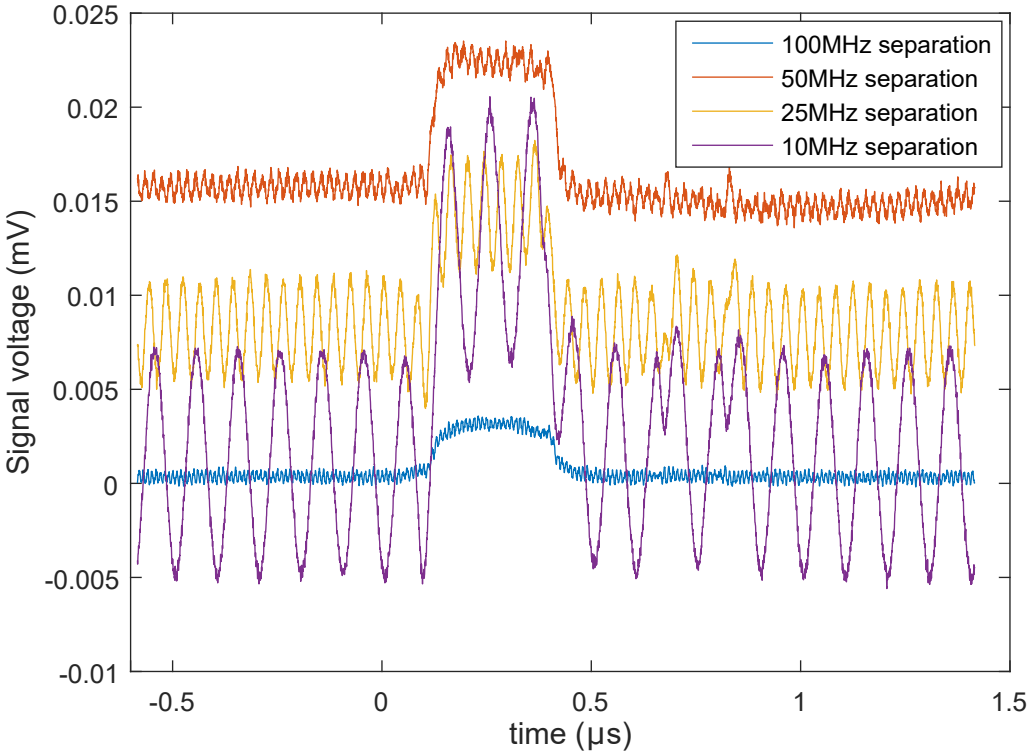


Figure 5.12: Heterodyne demodulation of PM pulses at 3.15 GHz, where a second signal exists at a frequency that is 10, 25, 50, and 100 MHz above.

AM/PM	Separation (MHz)	Signal size (mV)	Crosstalk size (mV)	Ratio
AM	100	2.840(12)	0.1824(103)	15.57(89)
AM	25	7.546(36)	5.567(97)	1.355(24)
AM	10	12.22(5)	13.66(5)	0.8946(49)
PM	100	2.684(14)	0.2797(80)	9.596(279)
PM	50	7.110(31)	0.5407(124)	13.15(65)
PM	25	6.535(117)	2.532(18)	2.581(49)
PM	10	11.62(27)	5.928(11)	1.960(45)

Table 5.1: Crosstalk ratios for two AM or PM encoded signals of a given frequency separation. 95% confidence bounds were extracted from the fitting parameters of a square wave or a sinusoidal function that was fit to the traces, and the ratio error was calculated by adding the fractional errors in quadrature. Just resolvable AM signals have a signal-to-crosstalk ratio of ≈ 1, whereas PM signals require a ratio of at least 2.

as the crosstalk exists on all parts of the signal. This means that when the crosstalk is two, the trough value of the negative crosstalk on the positive pulse has the same value as the peak value of the crosstalk on the rest of the signal, and are therefore inseparable. The data in Table 5.1 show that when the frequency separation is roughly the same as the filter strength, then the data is just resolvable.

Figures 5.13, 5.14, 5.15, and 5.16 have data of the same format as Figures 5.9 and 5.10, but for the cases of AM signals with 10 and 100 MHz separations. This allows for an alternative visualization of the data, and helps to show the effects of bringing signals 'too close together'. In Figures 5.14 and 5.16, there is clear evidence of crosstalk between the two data channels, as significant voltages are recorded in both channels when either of the data pulses are present. This crosstalk is not present in Figures 5.13 and 5.15, demonstrating that in this case, the channel spacing is sufficiently large with respect to the filter used.

Filters vs Signal spacing

Having established that the threshold for frequency spacing between channels is approximately set by the characteristic frequency of the low-pass filter used, the prospect of using a much stronger filter appears attractive, as it might then be possible to fit hundreds of data channels into the available bandwidth. Although

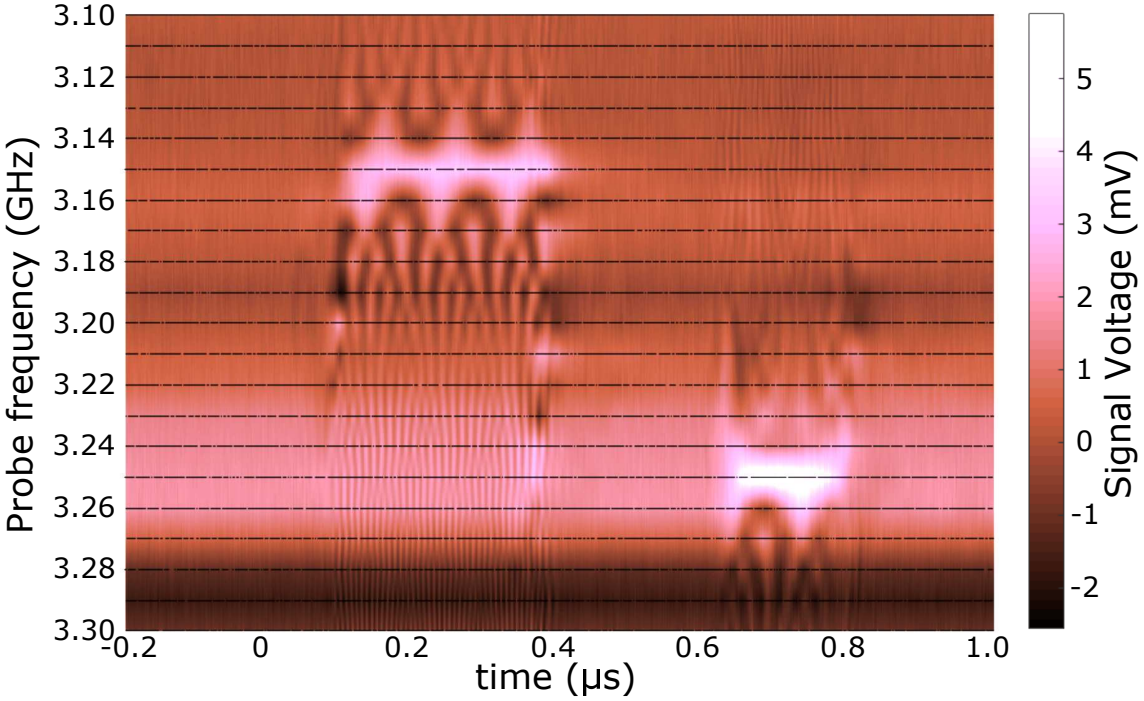


Figure 5.13: 2D plot of heterodyne demodulated AM magnon signals, 100 MHz apart, at 3.15 GHz and 3.25 GHz. Each horizontal line is a trace recorded using the probe frequency shown on the y axis. Signal voltage is indicated by the colour map. (This plot is a reprint of Figure 5.9, shown here to ease comparison with Figure 5.14).

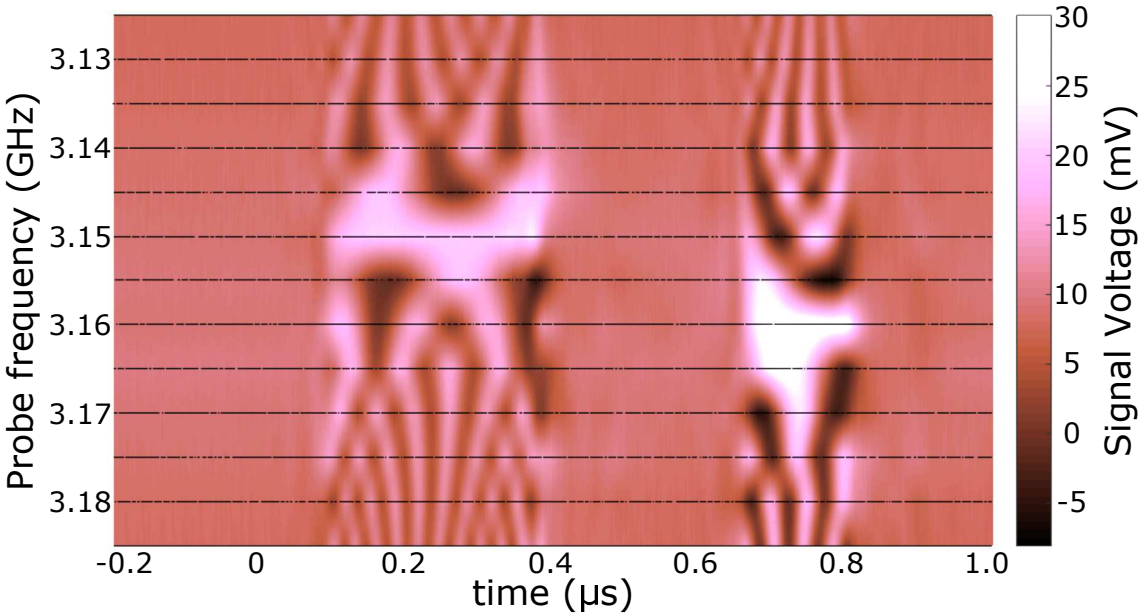


Figure 5.14: 2D plot of heterodyne demodulated AM magnon signals, 10 MHz apart, at 3.15 GHz and 3.16 GHz. Each horizontal line is a trace recorded using the probe frequency shown on the y axis. Signal voltage is indicated by the colour map.

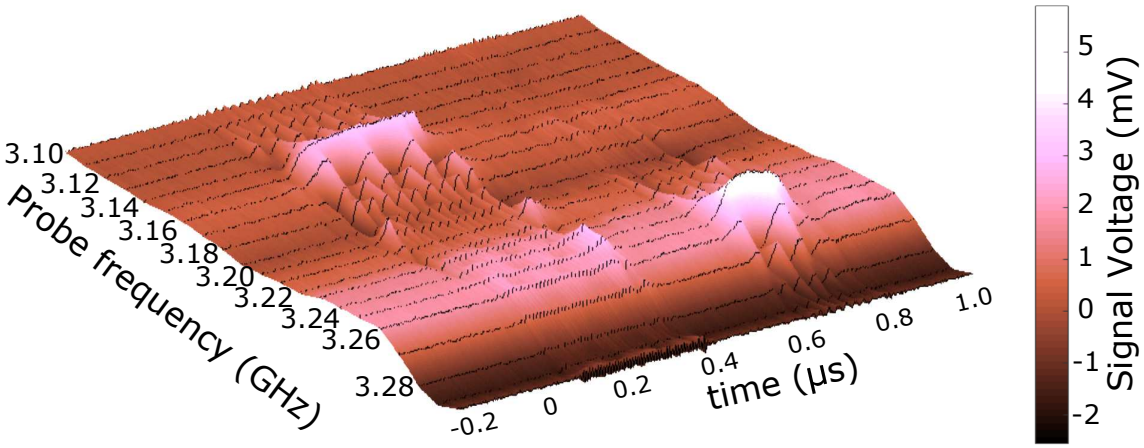


Figure 5.15: 3D plot of heterodyne demodulated AM magnon signals, 100 MHz apart, at 3.15 GHz and 3.25 GHz. Notice the almost constant value across the 3.20 GHz trace. This shows how appropriate filtering and channel spacing can be used to avoid channel crosstalk.

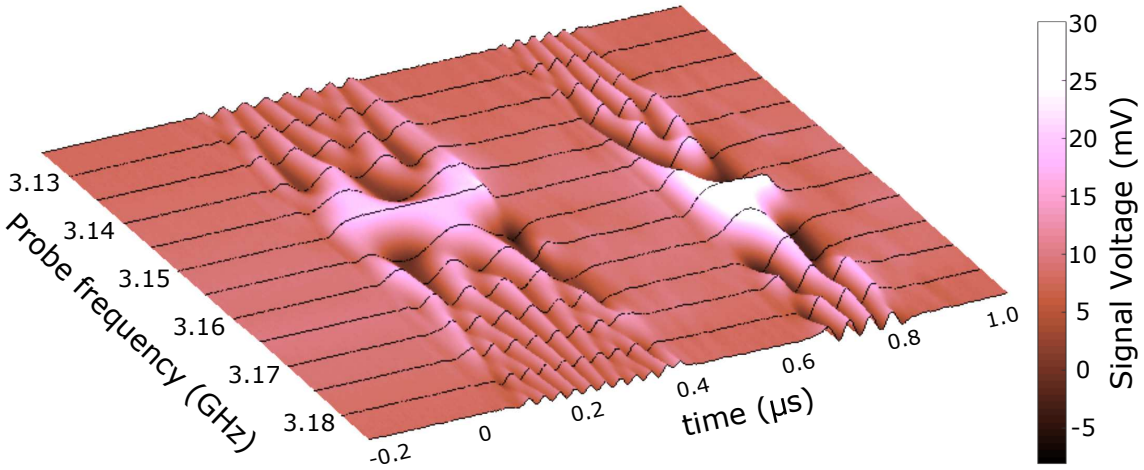


Figure 5.16: 3D plot of heterodyne demodulated AM magnon signals, 10 MHz apart, at 3.15 GHz and 3.16 GHz. Notice that both pulses appear in both the 3.15 GHz and 3.16 GHz channels to a certain degree. This highlights the problems with bringing two channels 'too close together'.

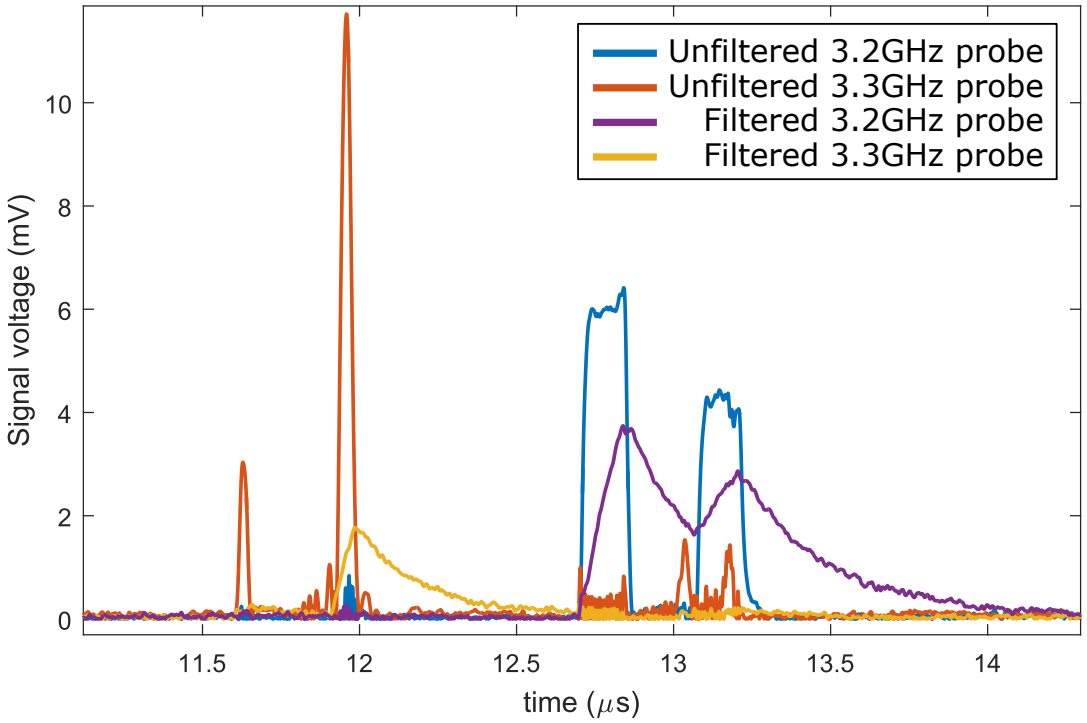


Figure 5.17: Effects of a 1 MHz low pass filter. The unfiltered traces of the heterodyned AM signals with a 100 MHz frequency spacing can be seen in red and blue. The effect of the 1 MHz filter on the signal can be seen in the yellow and purple traces. Due to the relatively long time constant of the filter's capacitor, the signals become distorted.

this seems an obvious avenue to pursue, unfortunately, doing so has a significant impact on the single channel bit-rate of each of the data channels.

The bit rate is the rate at which data can be transmitted through a system. The first part of this characteristic value is the number of channels available, whereas the second part is the pulse length of each individual data bit, which is directly related to the single channel bit-rate. In the above experiments, the shorter pulse was 150 ns long, which equates to a single channel bit rate of $6.7\,\mathrm{Mbs}^{-1}$ (or $0.83\,\mathrm{MBs}^{-1}$).

Figure 5.17 shows purely electrical heterodyned signals for 100 MHz separated AM pulse trains, which have subsequently either been filtered by a 1 MHz filter, or not. It is noted here that for this plot, a different pulse train to the experiments above was used.

The 1 MHz filtered traces exemplify the main problem with lower cut-off frequency filters: long time constants. If the workings of a simple low-pass filter are considered, the circuit's RC time constant τ_f represents the time taken to charge the

capacitor. If the voltage oscillates faster than this characteristic time, the capacitor does not have sufficient time to charge, blocking the signal.

For the 1 MHz filter, that time constant is around 160 ns, which is on the same order as the duration of the second set of pulses used. It can be clearly seen that this strong filtering leads to the traces never reaching the peak pulse voltage of any given pulse, and also taking a significant time to return to the zero value. For the case of the 28.5 MHz filter, the time constant is around 5.5 ns, which is fast enough that the peak voltage should be reached relatively quickly for the longer pulses, but may still struggle in the case of very short pulses.

In §5.3.4, it was shown that if the low-pass filter's cut-off frequency is equal to the channel spacing, then the data streams are just resolvable. This fact allows for calculations of the channel spacing and filter strength that optimise the bit-rate, which presented in Table 5.2. Assuming that the maximum bandwidth of the waveguide is 100 MHz, the maximum low-pass filter time constant is calculated from equating the filter frequency to that of the channel spacing. Since the capacitor charges exponentially, a pulse length is required that is a few multiples of τ_{f}, so that the pulse can complete its switching to a satisfactory level. As that multiple is a somewhat arbitrary choice, Table 5.2 includes pulse lengths that are 3, 4, and 5 times that of τ_{f}. The final bit-rate is then calculated by multiplying the number of bits of length t_{pulse} by the number of channels, and is presented in the final three columns.

Table 5.2: Theoretical maximum bit-rates of the magnon waveguide for heterodyne demodulated multiplexed signals. These rates depend on the frequency spacing of, and number of multiplexed channels used, as well as the individual pulse duration, and the constraints on the quality of the pulse shape (which is characterised by the time constant of the filter with respect to the pulse length). Optimal achievable bit rates are around $230\,\mathrm{Mbs}^{-1}$.

number of channels	frequency separation	time constant τ_f of filter	pulse lengths t_pulse given as multiples of τ_f			Bit-rate for n channels for given t_pulse		
			$t_\mathrm{pulse} = 3\tau_\mathrm{f}$	$t_\mathrm{pulse} = 4\tau_\mathrm{f}$	$t_\mathrm{pulse} = 5\tau_\mathrm{f}$	$t_\mathrm{pulse} = 3\tau_\mathrm{f}$	$t_\mathrm{pulse} = 4\tau_\mathrm{f}$	$t_\mathrm{pulse} = 5\tau_\mathrm{f}$
	MHz	ns	ns	ns	ns	Mbs^{-1}	Mbs^{-1}	Mbs^{-1}
2	100.00	1.59	4.77	6.37	7.96	418.88	314.16	251.33
3	50.00	3.18	9.55	12.73	15.92	314.16	235.62	188.50
4	33.33	4.77	14.32	19.10	23.87	279.25	209.44	167.55
5	25.00	6.37	19.10	25.46	31.83	261.80	196.35	157.08
6	20.00	7.96	23.87	31.83	39.79	251.33	188.50	150.80
7	16.67	9.55	28.65	38.20	47.75	244.35	183.26	146.61
8	14.29	11.14	33.42	44.56	55.70	239.36	179.52	143.62
9	12.50	12.73	38.20	50.93	63.66	235.62	176.71	141.37
10	11.11	14.32	42.97	57.30	71.62	232.71	174.53	139.63
11	10.00	15.92	47.75	63.66	79.58	230.38	172.79	138.23
12	9.09	17.51	52.52	70.03	87.54	228.48	171.36	137.09
13	8.33	19.10	57.30	76.39	95.49	226.89	170.17	136.14
14	7.69	20.69	62.07	82.76	103.45	225.55	169.16	135.33
15	7.14	22.28	66.85	89.13	111.41	224.40	168.30	134.64

It is noted that the maximum bit-rate is roughly consistent across the number of data channels used above n= 4. Higher bit rates are available for n=1,2 or 3, as the required filters become weak, and pulse lengths can become unrealistically short. The fastest electrical pulses that the author was able to produce had $t_{\text{pulse}} \approx 10\,\text{ns}$, whereas the switches used had a switching time on the order of 50 ns. This suggests that the highest theoretical bit-rates in the table are practically unobtainable, and that the maximum obtainable bit-rates are around the $230\,\text{Mbs}^{-1}$ mark.

The fact that the maximum bit-rate is weakly dependent on the number of data channels raises the question of whether it is worth the effort of multiplexing, rather than merely using one or two channels with a fast data rate. Multiplexing offers an opportunity to by-pass problems caused by slow switching times of the microwave switches or other components, and therefore does open the possibility of increasing the transmission and processing power of a magnonic circuit.

5.3.5 Interferometry method

An alternative method of signal demultiplexing was also investigated — the interferometer. Although less successful than the heterodyne demodulation method, the investigation into its functionality is presented here.

The electrical interferometer used as a signal detector is depicted in Figure 5.18. The basic operation is as follows:

General layout Two channels (the signal and the probe), are split using signal splitters. The signal is the output from the transmission line, whereas the probe is a continuous wave generated with an amplitude and frequency that can be controlled. One of the probe branches experiences a 180° phase shift with respect to the other probe branch. A signal branch is then joined with each of the probe branches in two further splitters (which function as combiners/adders when operated in reverse). This leaves two channels, which are now effectively ‘signal plus probe’ and ‘signal minus probe’.

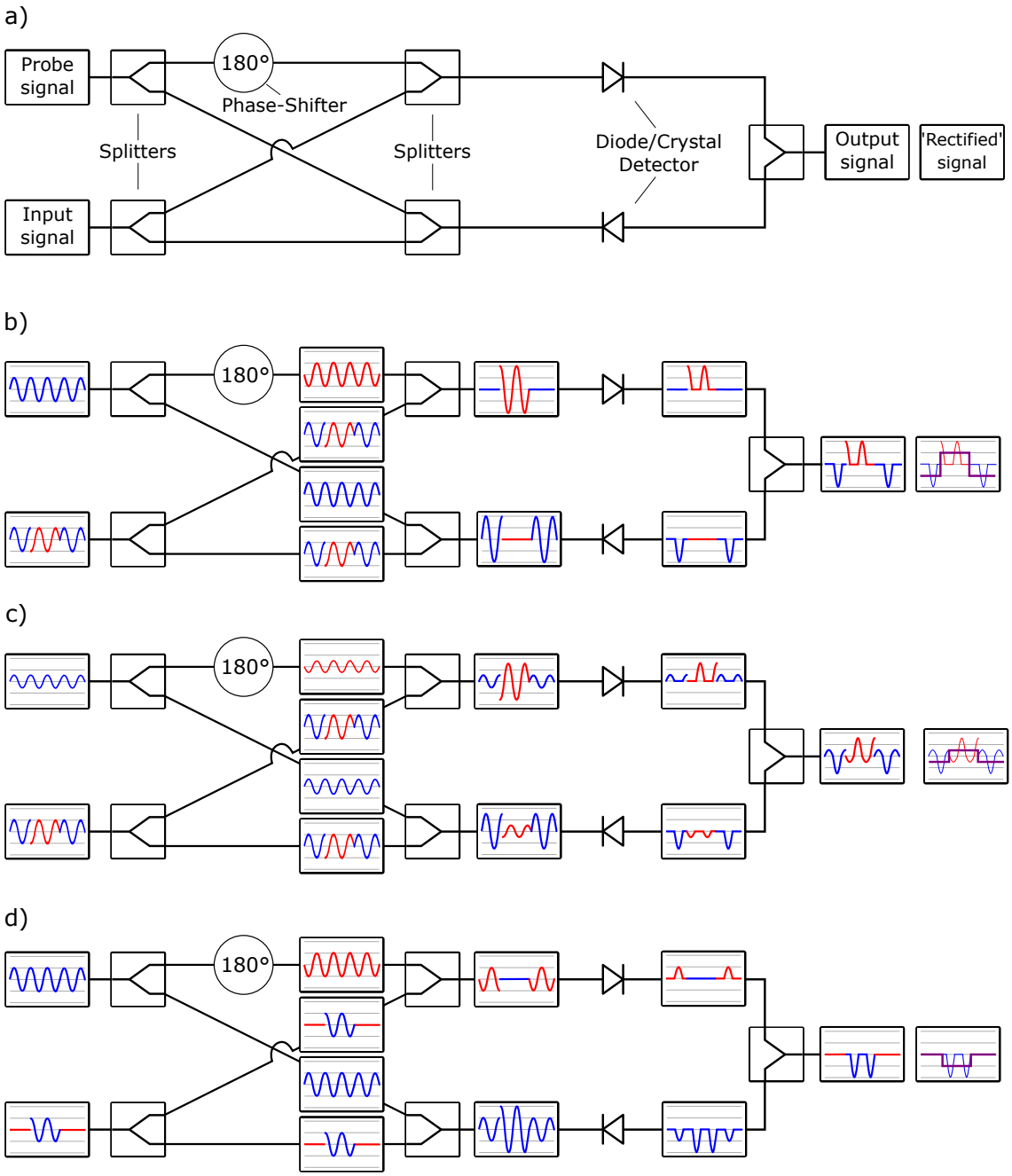


Figure 5.18: Diagrams of the Interferometer demodulator. a) A schematic of the constituent components of the interferometer. b) The propagation of a PM signal (with the same amplitude as the probe) through the interferometer. Red and blue waveforms indicate a phase shift of 180°. The final 'rectified signal' box has the detected output waveform in purple, which corresponds to the information encoded in the input signal. c) The propagation of a PM signal when the probe has a different amplitude to the signal. d) Propagation of an AM pulse through the interferometer.

Each of these channels is then passed through a diode/crystal detector, before being recombined in a final splitter. Crystal detectors take a high frequency signal and produce a DC signal with a voltage related to that of its input. The diodes inserted in the circuit are installed with opposing polarities, such that one produces a positive signal, and the other produces a negative signal. When the two channels are recombined, this has the same effect as measuring the amplitudes of the two channels and subtracting them. The output from the interferometer is then ready to be viewed on an oscilloscope.

Worked examples To gain a better understanding of the workings of the interferometer, the propagation of an AM pulse through the device is presented in Figure 5.18d, with the waveform depicted at each stage. In this case, for clarity, the amplitude of the probe input is the same as the amplitude of the signal input, and again, the colours red and blue have been used to indicate signals with phase differences of 180°.

Following the progression of the various waveforms through the device in Figure 5.18d, it is possible to deduce how the final purple 'rectified' signal was extracted. The origin of the rectification can either be thought of as coming from the crystal detectors themselves, or, if a diode is used, as in the diagram, this rectification comes from the fact that the oscilloscope is not fast enough to record GHz frequencies, and instead provides an averaged DC signal. Either way, this DC signal is the extracted binary data required.

Figure 5.18b shows the progression of a PM pulse through the interferometer. Once again it is possible to extract a rectified signal containing easily read binary data from the device. It is also noted here that the interferometer still functions even if the probe signal and the input signal have different amplitudes (in both the AM and PM cases). This is depicted for a PM signal in Figure 5.18c. It can be seen that the output signal is somewhat modified, and the rectification (via finding the average voltage value) provides a slightly smaller signal. It does, however, still theoretically work.

Amplifier caution An important element of both styles of interferometer is the amplitude of the signals in each channel. For the most part, there is symmetry in the components and wires through which both probe and signal microwaves propagate. The key exception to this is the 180° phase-shifter in one branch of the probe line. The additional loss incurred at this point must be compensated for later in the line, otherwise the two probe channels will not annihilate appropriately in the absence of a signal when recombined later, and lead to a DC offset. As the amount of loss acquired is dependent on the frequency of the probe, it means that the amplifier needs to be tuned for each new frequency under investigation.

Other frequencies Although it has been shown how the device is able to extract binary data from either an AM or a PM signal when the probe is set to the correct frequency, it is also worth considering what happens to other frequencies propagating through the interferometer.

When the input signal frequency and the probe frequency differ, a beating pattern will appear when the two channels are combined. Over the course of one 'beat', the relative phase of the signal with respect to the probe will perform a full 360° rotation. This would look very similar to a PM signal in which the signal frequency matched that of the probe, and also had an oscillating binary state. The only difference being that in this case, the oscillation is digital, whereas in the beating case, the oscillation is sinusoidal. This would then propagate through the device as in Figures 5.18b and c, resulting in a DC voltage which oscillates on the time scale of the beat.

As the beat frequency is given by the formula $f_{\text{beat}} = |f_{\text{Probe}} - f_{\text{signal}}|$, if the two signals are sufficiently different, then the beat frequency will be too fast to be fully registered by the oscilloscope, or will be a high enough frequency that it can be easily filtered. Similarly, if the duration of the beat is much longer than the duration of a bit, then it is again not an issue. These two considerations are relevant when considering the frequency spacing of multiplexed channels.

5.3.6 Interferometer Results

The interferometer was set up as in Figure 5.18. As the interferometer used the majority of the available signal splitters, it was not possible to assemble both the interferometer and the PM encoder circuits simultaneously. For this reason, the investigation into the interferometer demodulator was restricted to AM signals only, which is presented below.

Interferometry proof of concept

A signal comprising two pulses of 3.15 GHz and 3.25 GHz microwaves was used as the initial input signal to test the interferometer, without the inclusion of the magnon waveguide. The attenuation of each branch of the interferometer was adjusted such that the output signal was as constant as possible when the probe input was deactivated. This ensured that the interferometer functioned as designed. Two traces were recorded, with the probe frequency set to 3.15 GHz or 3.25 GHz, and are plotted in Figure 5.19. This plot shows that it is possible to distinguish between the two AM pulses for a purely electrical signal using the interferometer demodulator.

The magnon waveguide was then reintroduced to the circuit, between the 'Input signal' box and the first splitter in Figure 5.18. The bias field was adjusted to maximise the transmitted magnon signal. This was measured by unplugging one branch of the interferometer after the diode and deactivating the probe signal. This allowed for the detection of just the magnonic signal, while maintaining the level of attenuation caused by the circuit. This trace is shown in Figure 5.20. This figure also shows the two traces recorded when the interferometer was reassembled, and the probe frequency was set to 3.15 GHz and 3.25 GHz.

The quality of all three of these signals is poor. The original magnon signal which contains both frequencies, has a signal strength of around 0.5 mV, whereas the demodulated signals have a signal strength of around 1.5 mV. There is also significant DC offset between each of the measurements. Despite the fact these signals are very small and fairly noisy, they do however demonstrate that interferometry

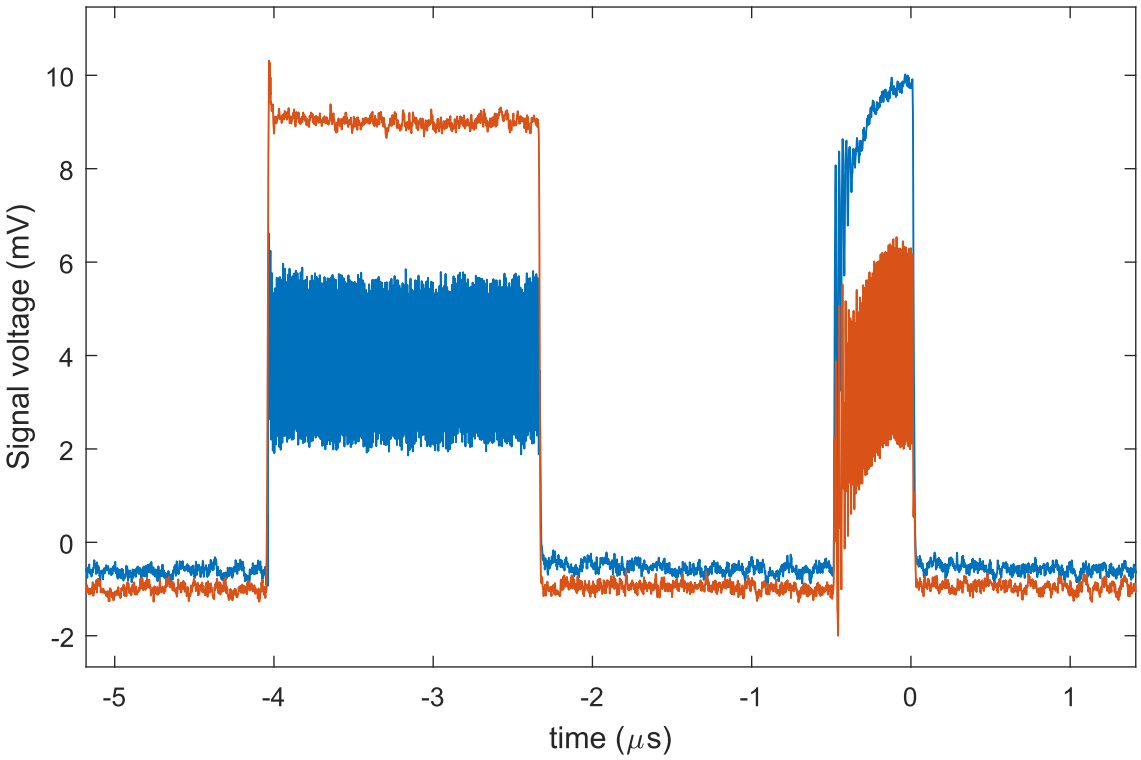


Figure 5.19: Interferometer demodulation of AM electrical signals at 3.15 GHz and 3.25 GHz.

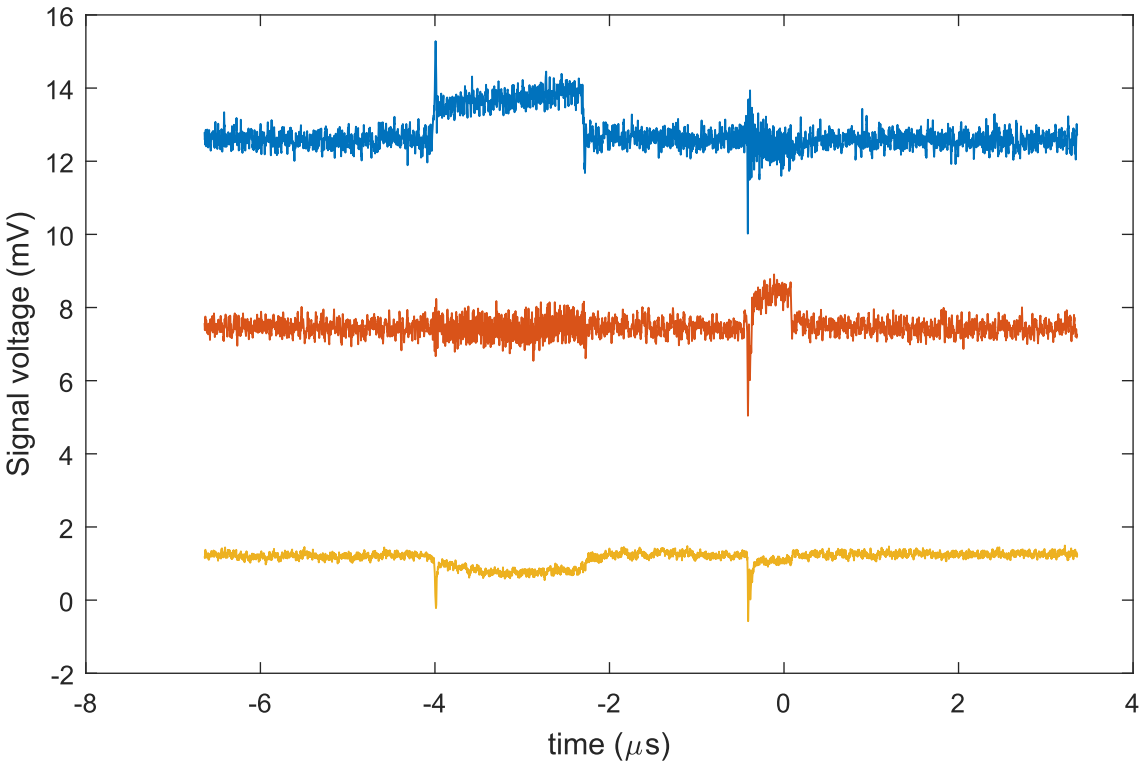


Figure 5.20: Interferometer demodulation of AM magnonic signals at 3.15 GHz and 3.25 GHz (Blue and Red respectively), and the unprocessed magnonic signal (yellow).

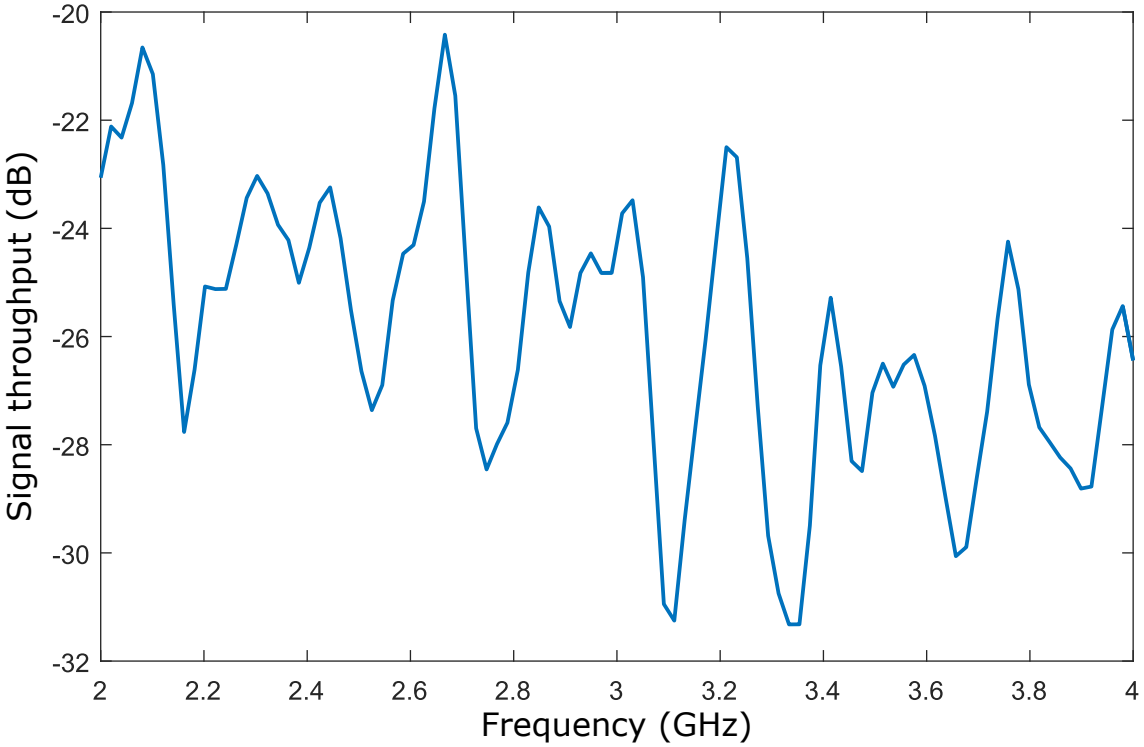


Figure 5.21: Transmission spectrum through a section of the Interferometer circuit consisting of three splitters and some cables.

based demodulation is possible.

The reasoning behind why the signals were so small was investigated, and it was determined that a significant contributing factor to the signal loss was the interferometer itself. Performing a transmission experiment on a section of the interferometer (from before the splitter used to combine the two input signals to just before the diode on one of the branches, which comprises three splitters and a few cables) on a network analyser, it was found that the interferometer attenuated the signal by around 26 dB. The transmission spectrum for this measurement is shown in Figure 5.21.

This loss is difficult to combat, as installing amplifiers into the circuit risks contaminating the signals, which already contain several frequency components (see §5.3.7). Using SMA tee pieces as an alternative to the splitters could also risk signals propagating into the wrong parts of the circuit. As the combined signal loss of the interferometer and the conversion to and from the magnonic waveguide totals around 40 dB, this suggests that the interferometer in its present form is not a viable

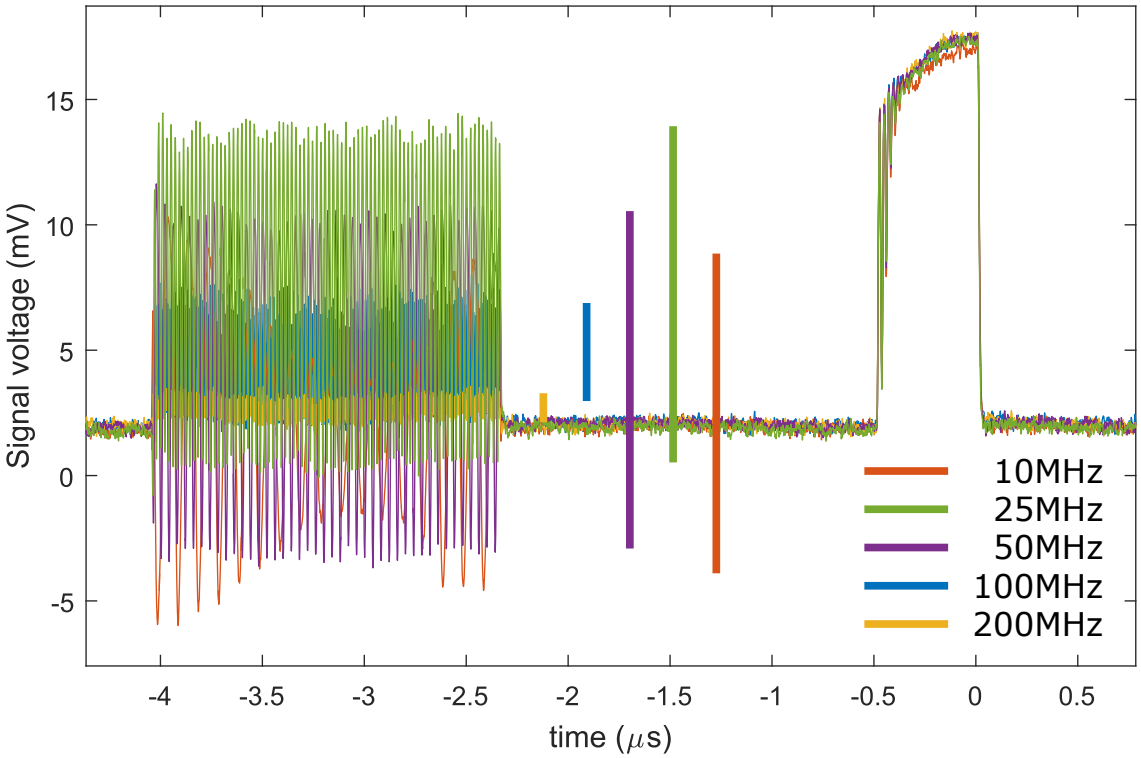


Figure 5.22: Interferometer demodulation of purely electrical AM pulses at 3.15 GHz, where a second signal exists at a frequency that is 10, 25, 50, 100, and 200 MHz above. Vertical lines have been added to the plot to indicate the amplitude of the beating pattern, which is otherwise difficult to see.

option for multiplexed magnon demodulation.

Effect of frequency spacing of electrical signals

Even though the interferometer was too lossy for practical purposes, the effect of probe-signal frequency spacing on signal crosstalk was investigated regardless. Figure 5.22 shows the demodulation of multiplexed signals that were not propagated through the magnon waveguide for a variety of frequency spacings. The lower of the two frequencies was always 3.15 GHz, while the other signal was set to a frequency that was 10, 25, 50, 100, and 200 MHz greater. The probe was set to 3.15 GHz for all of the traces, such that the residual signals at the location of the other pulse could be compared.

In the plot, it is possible to see the beating pattern predicted in §5.2.3 in all of the traces. As it is difficult to see all of the beats clearly, lines indicating the beating amplitudes have been added for each trace. It can be seen that the amplitude

of the beating decreases with frequency spacing, and becomes smaller than the demodulated signal when the spacing is 100 MHz. As the bandwidth of the magnon waveguide is around 100 MHz, this suggests that only two magnon channels could be processed using the interferometer at any given time without creating too much crosstalk in the rest of the signal.

5.3.7 Troubleshooting/Design considerations

While performing this investigation, several issues with the apparatus/setup were discovered. For the purpose of aiding anyone who attempts to replicate the work from this thesis, an account of some of the problems, and how they were accounted for or resolved is provided here.

Signal sidebands in the amplifier

The first effect observed was the non-linearity of the amplifiers used. When the amplifiers were positioned between the signal generation and signal transmission stage of the experiment, side-bands were observed in the output spectrum viewed on the spectrum analyser. It was realised that this was due to signal mixing within the amplifier, which was confirmed by arranging a setup of two microwave sources joining in a splitter, followed by an amplifier and a 60 dB attenuator before being measured in the spectrum analyser. The spectrum presented when a 3.0 GHz and a 3.05 GHz signal were amplified together is shown in Figure 5.23. Sidebands can be seen on either side of the two input signals, the first being only 10 dB weaker than the original signals. This measurement resulted in care being taken to amplify only single frequency data streams, so as to avoid contaminating adjacent frequency channels.

Direct coupling of the antennae

As mentioned in section §5.2.1, when two microwave antennas are positioned close to each other (such as with the magnonic waveguide setup), radiation emitted by

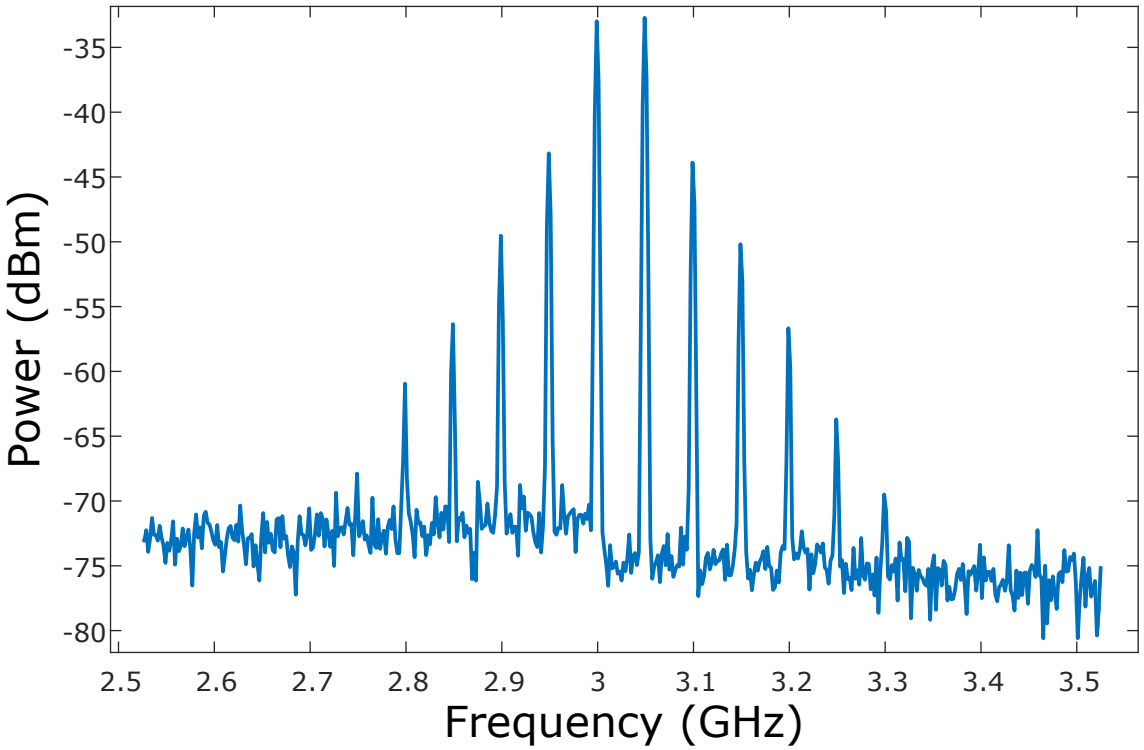


Figure 5.23: Demonstration of non-linearity in a power amplifier. Two input signals (3 GHz and 3.05 GHz) were added together, and then amplified by 40 dB, before being attenuated by 60 dB and measured on a spectrum analyser. Non-linearity in the amplifier led to the generation of sidebands, which can be seen here.

one antenna can be picked up by the other. This direct coupling is dependent on the separation of the antenna, and, for the frequencies used here, is fairly lossy. The loss at frequencies around 3.2 GHz with an antenna separation of 2 mm was measured to be −30 dB. Screening this direct coupling is nigh-on-impossible, and it is therefore important to correctly set the magnon bias field. Doing so will ensure that all frequencies of interest can be transmitted by the magnons in such a way that magnons rather than direct coupling dominates the signal. This can be calibrated using the spectrum analyser.

Switching spikes

Within the AM/PM modulating system, the digital data is encoded into the microwave signal through the use of microwave switches. If the microwave throughput of one of these switches is rectified with a crystal detector, and then viewed on an oscilloscope, voltage spikes at the beginning and end of each pulse are observed —

switching spikes. These can be dealt with with relative ease by installing high-pass filters before and after each switch. It is necessary to use two filters, as the voltage spike is emitted in both the forward and backwards direction, and may cause issues elsewhere in the system if not confined to the switch. In the experiments, 50, 250, 500 and 700 MHz filters were used, as they were to hand.

Frequency dependence of signal amplitudes — cables and components

When performing experiments where the amplitude of the microwave signal is significant (e.g. in the interferometer, where the amplitudes on each branch need to be able to cancel out), it is necessary to be aware of the possibility of unintentional amplitude variation. As mentioned in the interferometry section, one source of this can be from microwave components, such as the phase shifter or the amplifiers, when the microwave frequency is altered. A second potential source are the SMA cables themselves.

Depending on the quality of the cables, microwave signals can be attenuated to various degrees depending on frequency and length of the cable. This means that simply switching two cables may interfere with any previous calibrations. In the author's setup, the microwave source was approximately 5m away from the rest of the equipment, and the SMA cable used had an attenuation varying between $-13\,\mathrm{dB}$ at $5\,\mathrm{GHz}$, to $-25\,\mathrm{dB}$ at $15\,\mathrm{GHz}$, which was appropriately compensated for by an amplifier. This example highlights the fact that the power output from the microwave source cannot be assumed to be the power input to the experiment. To calibrate this, the least lossy cable possible was identified using the network analyser, and then used along with the spectrum analyser to measure the power inputs just before the experiment. The levels of the amplifiers were then adjusted appropriately to ensure the correct amplitudes were used.

Overpowering components

A final word of caution when pursuing maximum signal outputs is to avoid overpowering the components. Most components have a threshold above which they cease to work properly which is usually provided in their data sheets. It was noted that some of the components used misbehaved and produced erroneous results when this limit was approached but not crossed, with a specific example being the microwave splitters/adders leading to a DC offset in their output signals. The obvious solution here is to reduce the input power so as to avoid these peculiarities.

5.3.8 Non-linear crosstalk between magnon channels

Magnonic systems can be easily driven into the non-linear regime [26]. While this can sometimes be useful for accessing interesting physical phenomenon, it could also potentially lead to non-linear crosstalk between magnon signals in different frequency channels. The above experiments show little to no evidence that this actually occurs, which is surprising given the ease with which magnons can be driven non-linear. A possible explanation of why this might be the case is presented here.

Any interaction between the magnonic signals of different frequencies must be at least a three-magnon process, as at minimum, two magnons must come in (one of each frequency), and at least one magnon must come out. As with most interactions, energy and momentum must be conserved. This leads to (for a three-magnon interaction) a particle with a specific energy and momentum combination. Due to the dispersion relation of the YIG waveguides, and the applied magnetic field, it is unlikely that this magnon is one that can be supported by the waveguide.

Four-magnon processes, in which two magnons come in, and two different magnons come out, can lead to interactions in which the output magnons are supported by the waveguide. The process by which this occurs is discussed in reference [29]. The main idea here is that the two input dipolar magnons (which each have a small, positive $\boldsymbol{k}$) scatter into two counter-propagating exchange magnons (which each have a much much larger $\boldsymbol{k}$, one of which is now in the negative direction). Due to the

unusual shape of the dispersion curve, states exist in which energy and momentum are conserved for this type of interaction.

The question is now whether this interaction should have a detrimental effect on multiplexed signal intensities. Despite the fact that some of the input electrical signals were as strong as +20 dBm, the answer appears to be no. Although the exchange magnons are supported by the waveguide, they are not detectable by the microwave antennae used in the experiments. This means that any rogue signal created by these interactions will not be detected or appear in the signal output. The only effect of these types of interactions might be an additional damping factor on the magnon signals, which should not harm the integrity of the carried data.

Other non-linear processes that have not been considered might have occurred, however, the experimental setup was not sensitive enough to distinguish them from either the direct coupling between the antennae, or the main experimental signals. As non-linearities might have been expected in these experiments, a future possible project relating to this work could be to establish the presence and magnitude of any non-linearities with an alternative detection method, and then determine whether they are indeed negligible, as this work seems to suggest.

5.4 Quadrature phase-shift keying

Apart from increasing the number of frequency channels being transmitted down a waveguide, or increasing the bit rate of each channel, what other methods can be used to increase the overall data transmission rate? Are there any other domains into which more information can be squeezed?

Quadrature phase-shift keying (QPSK) is a method by which the amount of data transmitted at any given frequency can be doubled. This is achieved by noting that if the real and the imaginary parts of a microwave signal can be independently measured, then, by modulating those two components independently, it should be possible to effectively multiplex two data channels into a single frequency. Although this is already an established technique for microwave signal processing[58], this

section investigates whether it is also possible in magnonic systems.

5.4.1 How it works

As suggested by the name, QPSK uses phase modulated signals. Recalling equation 5.2 from the section on heterodyne signal detection (§5.2.3), it is noted that the DC output voltage from a heterodyned signal has a voltage that is related to $\cos(\phi)$, with ϕ being the difference between the phase of the data signal and the phase of the probe signal. This cosine represents the real part of the exponential used in §4.1 to define the complex value ζ. When $\phi = 90°$ or 270°, $\mathrm{Re}(\zeta) = \cos(\phi) = 0$, and all information about which of those two phase states the signal was in is lost. This feature turns out to be rather useful.

Before diving into details, it is necessary to introduce a few more angles. Up until now, the probe signal used for heterodyning has been set to be in phase with the reference signal used to encode the phase modulated signals. This does not necessarily need to be the case. The angle θ is now defined as the phase difference between the reference signal and the probe signal. This defines the 'measurement axis' onto which the ζ-states are projected when a heterodyne measurement is made. ψ is defined to be the phase difference between the reference signal and the data signal when the PM data was encoded. The data is still encoded with 180° between the two binary states, which are labelled ξ^+ and ξ^-, but now the two phases can deviate from the absolute values of 0° and 180° by ψ. These angles are shown in Figure 5.24 for convenience.

The trick with quadrature phase-shift keying is to encode two different data signals into a single frequency, but set $\psi = 0°$ for one data stream, and $\psi = 90°$ for the other. These are sometimes known as the 'in-phase' and 'quadrature' axes [59]. When the combined data stream is decoded using the probe signal, each channel can be independently extracted by setting θ to either 0° or 90°. This works as signals for which $\phi = |\psi - \theta| = 90°$ contribute nothing to the output voltage. This can be seen more clearly with a bit more algebra.

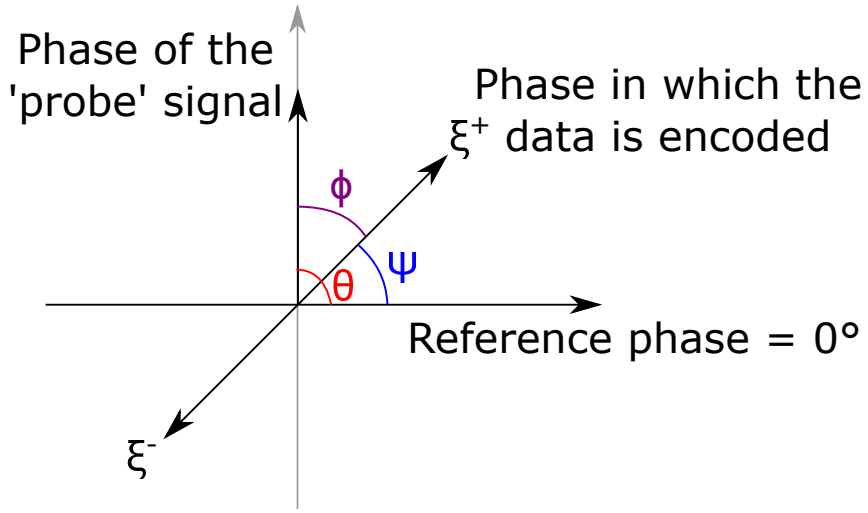


Figure 5.24: Definitions of angles used in the quadrature phase-shift keying discussion. The reference signal is always set to 0°. ψ is the phase at which a data signal is encoded, and $\xi^{\pm}$ represent the two PM encodes states of this data signal. θ is the phase difference between the probe signal and the reference. ϕ is the difference between the probe and the data signals, and is the phase difference that is 'measured' by the heterodyne demodulator.

Due to the principal of superposition, the two data streams do not interact with each other, but can be added together and subsequently described using a combined cosine function:

$$\cos(\omega t + 0° + \xi_1) + \cos(\omega t + 90° + \xi_2) = \sqrt{2}\cos(\omega t + (2n+1) \times 45°) \qquad (5.4)$$

where ξ_1 and ξ_2 represent the phase encoding of each data stream and are 0° or 180°, and n takes values from 0 to 3, corresponding to all of the possible combinations of $\xi_1^{\pm}$ and $\xi_2^{\pm}$. This can be plotted in a 'constellation plot' (Figure 5.25).

Aside: Constellation plots Constellation plots are a useful tool for visualising phase-shift keyed signals. The diagram displays the complex plane occupied by ζ, showing a signal's relative amplitude and phase with respect to the reference signal (which is why the reference is always at zero). Figure 5.25 shows the four values of ζ represented by $\sqrt{2}\exp(i \times (2n+1) \times 45°)$. The logic behind this representation can be understood by considering the vectors representing each of the four constituent states (that is, $\xi_1 = \pm 1$ aligned to the 'x-axis', and $\xi_2 = \pm 1$ aligned to the 'y-axis').

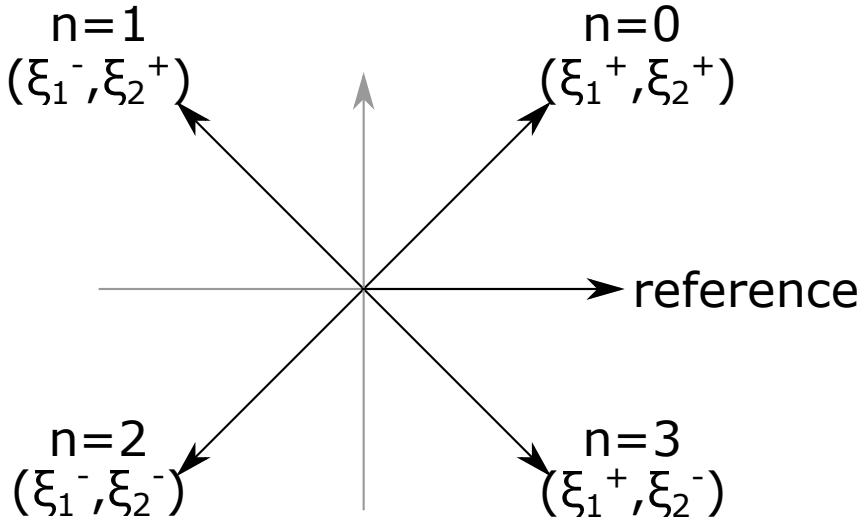


Figure 5.25: Constellation plot of the four QPSK states. The four corner states correspond to the phases of the combined waveform when each channel is in its plus or minus state, given that the first channel is encoded along the 'x-axis', and the second channel encoded along the 'y-axis'.

Adding $\zeta_1 = \exp(i \times 0° + 0°)$ to $\zeta_2 = \exp(i \times 90° + 0°)$ gives $\zeta = \sqrt{2}\exp(i \times 45°)$, which represents the (ξ_1^+, ξ_2^+) state on Figure 5.25, as expected. Constellation plots are used again later in Figures 5.27 and 5.28.

Using the new cosine from equation 5.4 as the input data signal for the heterodyning equation provides a new output of

$$\begin{aligned} &\cos(\omega t + (2n+1) \times 45°) \times \cos(\omega t + \theta) = \\ &\frac{1}{2}(\cos(2\omega t + (2n+1) \times 45° + \theta) + \cos((2n+1) \times 45° - \theta). \end{aligned} \tag{5.5}$$

Taking the non-time-varying component now provides a general output for a measured quadrature phase-shift keyed signal. The values of the DC output are shown for each n state, and for a selection of θ in table 5.3.

Looking at this table, two patterns can be seen to emerge, depending on whether θ is set to $n \times 90°$ or $n \times 90° + 45°$. In the former case, the outputs are $\pm\frac{\sqrt{2}}{2}$, with the plus or minus matching the ζ value for whichever ('x-axis' or 'y-axis') channel the probe is in phase with. This demonstrates that either of the two original signals

Table 5.3: Table of DC outputs expected from a QPSK measurement for a variety of probe phases (θ). The appropriate equation is: $V = \cos((2n+1) \times 45° - \theta)$

θ	$n=0$	$n=1$	$n=2$	$n=3$
0°	$+\frac{\sqrt{2}}{2}$	$-\frac{\sqrt{2}}{2}$	$-\frac{\sqrt{2}}{2}$	$+\frac{\sqrt{2}}{2}$
45°	1	0	-1	0
90°	$+\frac{\sqrt{2}}{2}$	$+\frac{\sqrt{2}}{2}$	$-\frac{\sqrt{2}}{2}$	$-\frac{\sqrt{2}}{2}$
135°	0	1	0	-1
180°	$-\frac{\sqrt{2}}{2}$	$+\frac{\sqrt{2}}{2}$	$+\frac{\sqrt{2}}{2}$	$-\frac{\sqrt{2}}{2}$

is retrievable, independently from the other. This is how QPSK is able to double the amount of data transmitted down a waveguide.

The output voltages in table 5.3 corresponding to the θ values of $n \times 90° + 45°$ take on the values of 0 or ± 1. This is interesting as it allows for the measurement of the results of certain logical operations as if they had been performed on the two data streams. For example, the output voltage will read '+1 V' when $\theta = 225°$ if and only if both streams are in their $\xi = 180°$, or binary-1 state. This is the expected behaviour of an AND gate. If $\theta = 135°$, the output voltage is zero if both the channels are in the same binary state. This is what might be expected from an XOR gate. Although this idea has not been developed here, this may be able to provide the basis of some unusual logic circuitry.

5.4.2 Experimental QPSK

An experiment was performed to determine whether it was possible to implement QPSK in a magnonic system. The initial signal was created using two PM encoding circuits (See §4.3.1) connected to a splitter, where one of the connections was a quarter of a wavelength longer that the other. This allowed for a combined signal to be created that contained components that were 90° out of phase with each other. This signal was propagated through the magnon waveguide as in previous experiments, and was detected using the heterodyne method.

The results of the experiment are presented in Figure 5.26. The original pulse trains for each channel are indicated at the top of the diagram, and it can be seen

that they are fairly well extracted (allowing for some switching spikes) in the two blue traces corresponding to $\theta = 0°$ and 90°. As predicted by table 5.3, it can be seen that when θ is varied by 180°, the sign of the signals in each of the traces is flipped. This is shown in the red plots for $\theta = 180°$ and 270°.

As the equipment used sometimes drifted in phase, to capture the traces when θ was at each value of interest, it was necessary to shift the frequency of the probe by 1 Hz such that the phase varied over time. Carefully freezing and saving the traces on the oscilloscope allowed for the data to be taken. This was a sub-optimal data collection method, and has caused some of the traces in the results to have small kinks where there should not be any (for example in the plots corresponding to $\theta = \pm 90°$). Thankfully this has not prevented the experiment from successfully demonstrating QPSK in a magnonic system.

The plots corresponding to $n \times 90° + 45°$ are shown in purple, in the appropriate corners. Here the different values the voltage takes for each of the two-bit states can be seen. Using appropriate diodes, or rectifiers, these signals can be processed to extract AND or XOR (and their negatives) logical calculations.

5.4.3 Higher order phase-shift keying

The above experiments demonstrate that QPSK can be implemented by superposing two PM encoded signals with a relative phase shift between them, and that it is indeed possible to double the number of bits transmitted down a magnon waveguide using QPSK. Is it desirable to know whether this method can be used to further increase the data transmission rate.

In electronic communications, 8-PSK [60], or 16-QAM (Quadrature amplitude modulation) [58] are sometimes used. These work by choosing 8 or 16 states in a constellation in ζ-space, and assigning them a 3 or 4-bit binary number, much the same way that the numbers $n = 0$ to 3 were used in Figure 5.25. For 8-PSK, evenly space states on a circle of unit radius are often used, whereas for 16-QAM, a 4×4 grid of states is common (As the states in the 4×4 grid do not have a constant

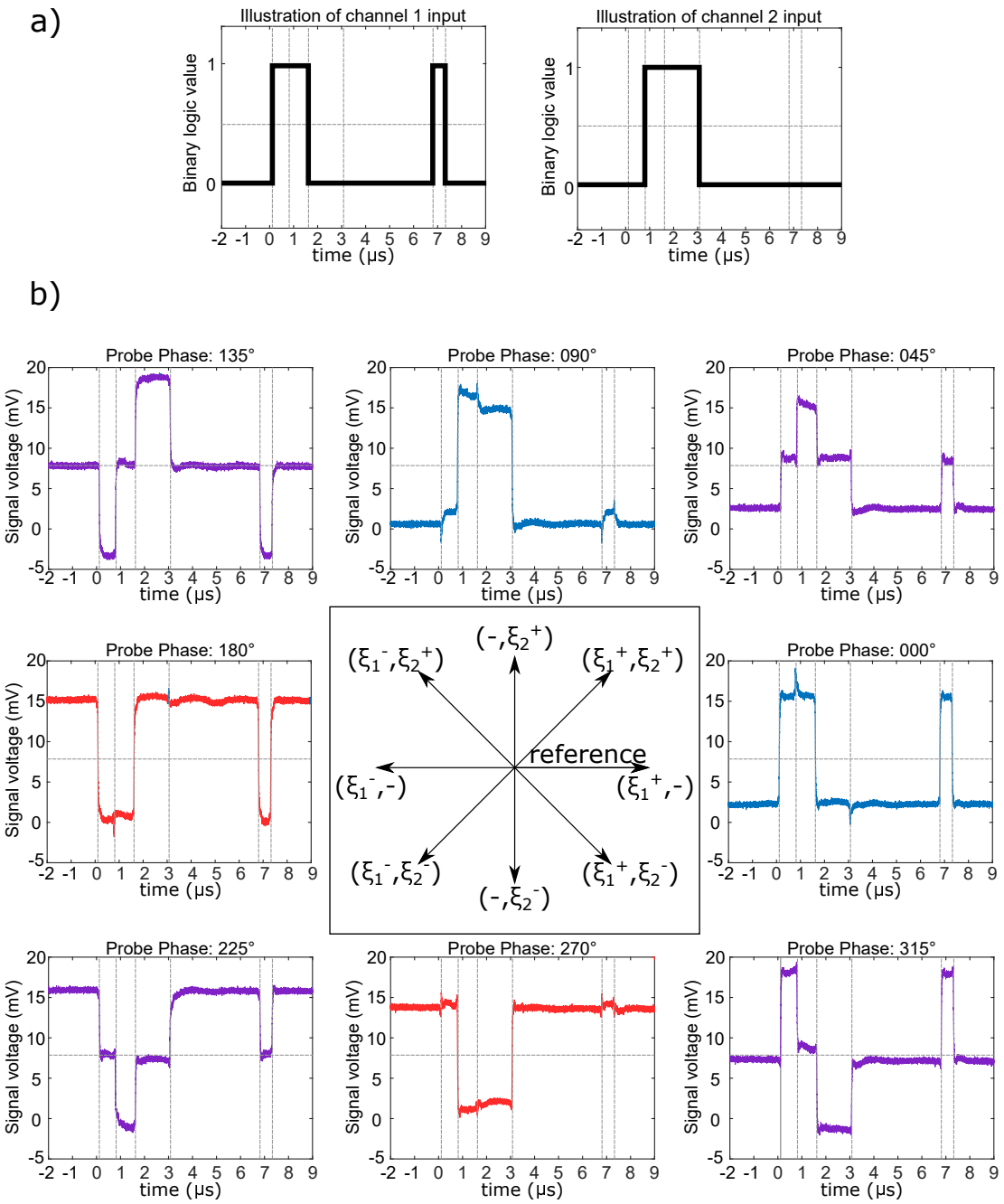


Figure 5.26: Experimental results of the magnon QPSK experiment. a) Illustrations of the binary data inputs for channels 1 and 2. b) The eight plots around the perimeter show the DC output voltage of the heterodyne demodulator as the phase of the probe (θ) was varied. Their location with respect to the reference line corresponds to the value of θ. The phase diagram in the centre shows the states of the combined system with respect to θ. The pulse trains encoded into channel one and channel two can be seen in the two blue plots at $\theta = 0°$ and $\theta = 90°$, which demonstrates that it is possible to extract them from the combined signal.

amplitude, the technique is known as 16-QAM rather than 16-PSK). Although this does increase the number of bits carried by a single frequency channel, there are two important problems that need to be considered.

The first problem that needs to be considered is how the states are measured. For QPSK, only a single heterodyne detector was needed to extract any given channel. For higher order PSK or QAM, a second heterodyne detector set 90° out of phase with respect to the first is needed, as by making two measurements it is possible to determine both the phase and the amplitude of the signal (and thus, which of the 8 or 16 states the system is in). Although this increases the complexity of the decoding setup, the fact that adding a second detector allows for the read-out of the full, complex value of ζ suggests that this is a worthy sacrifice for the potential increase in information carried.

It is noted here that access to the full, complex value of ζ could also be beneficial to other magnonic experiments (PSK or otherwise). The use of two heterodyne detectors for this purpose should therefore be considered as an important experimental technique that is available when designing future experiments.

The second problem with higher order PSK that needs to be considered is how these states are produced. The QPSK experiment was performed using two superposed waves with a 90° phase shift between them. This works as $\sin\theta$ and $\cos\theta$ form an orthogonal basis in phase space. If new bits are introduced, there are no other unique 'directions' that can be used, so it is impossible to construct a perfect 8-PSK constellation (or 16-PSK) in which all the states have the same amplitude using the superposition method. Instead, the constellations for the 8-PSK states or 16-QAM states must be generated in some other way, and *then* have their binary number assigned. The numbers are usually mapped in a specific way, and are called the 'Gray codes' of each state[58].

Although assigning Gray codes to 8-PSK or 16-QAM states does work as a method for boosting the amount of data carried in a single channel (which is usually the aim in fibre-optic communications), the fact that the states cannot be directly

generated by superposition means that interference-based magnonic logic gates will no longer operate as expected. This turns out to be the crux of the problem with the majority gate, which is discussed below. Given that using higher order PSK or QAM than just QPSK appears to detrimentally affect the potential functionality of magnonic devices, it is not investigated further here.

Some thoughts about the majority gate

As mentioned in §1.3.1, the majority gate currently has one major drawback, which is that the output contains both phase and amplitude information. This is relevant here, as what the majority gate has effectively done, is attempt to produce an 8-PSK data signal... just without any phases. The end result is a straight line along $\theta = 0$, with radial voltage values of -3, -1, $+1$ and $+3$. The ± 1 states are degenerate, and each contain two 3-bit states. This is shown in Figure 5.27a.

Figure 5.27 displays constellation plots (discussed briefly in §5.4.1) for three interfering waves. This is again a plot in the complex plane of ζ, where the values of ζ obtained by adding three waves (and thus complex vectors) are depicted as red, blue, or purple circles, labelled with their corresponding 3-digit binary states. Red indicates a majority of '1', blue indicates a majority of '0', and purple represents a degenerate state of no specific majority. The three black arrows represent the phase offsets (ψ) for the three different input channels, showing the axes onto which each of the three data signals were encoded. White circles represent nodes in the three-vector sum, which are drawn to assist the reader understand the patterns. Combining these concepts, it can be seen why the (110) state in Figure 5.27c can be reached by taking one step to the right (following black arrow 1), then one step up and to the left (following black arrow 2), followed by a final step up and to the right (following black arrow 3 in the wrong direction, on account of it being in the '0' state).

It is desirable to show whether it is possible to modify the majority gate (by changing each channel's ψ or amplitude) in such a way that its functionality can be

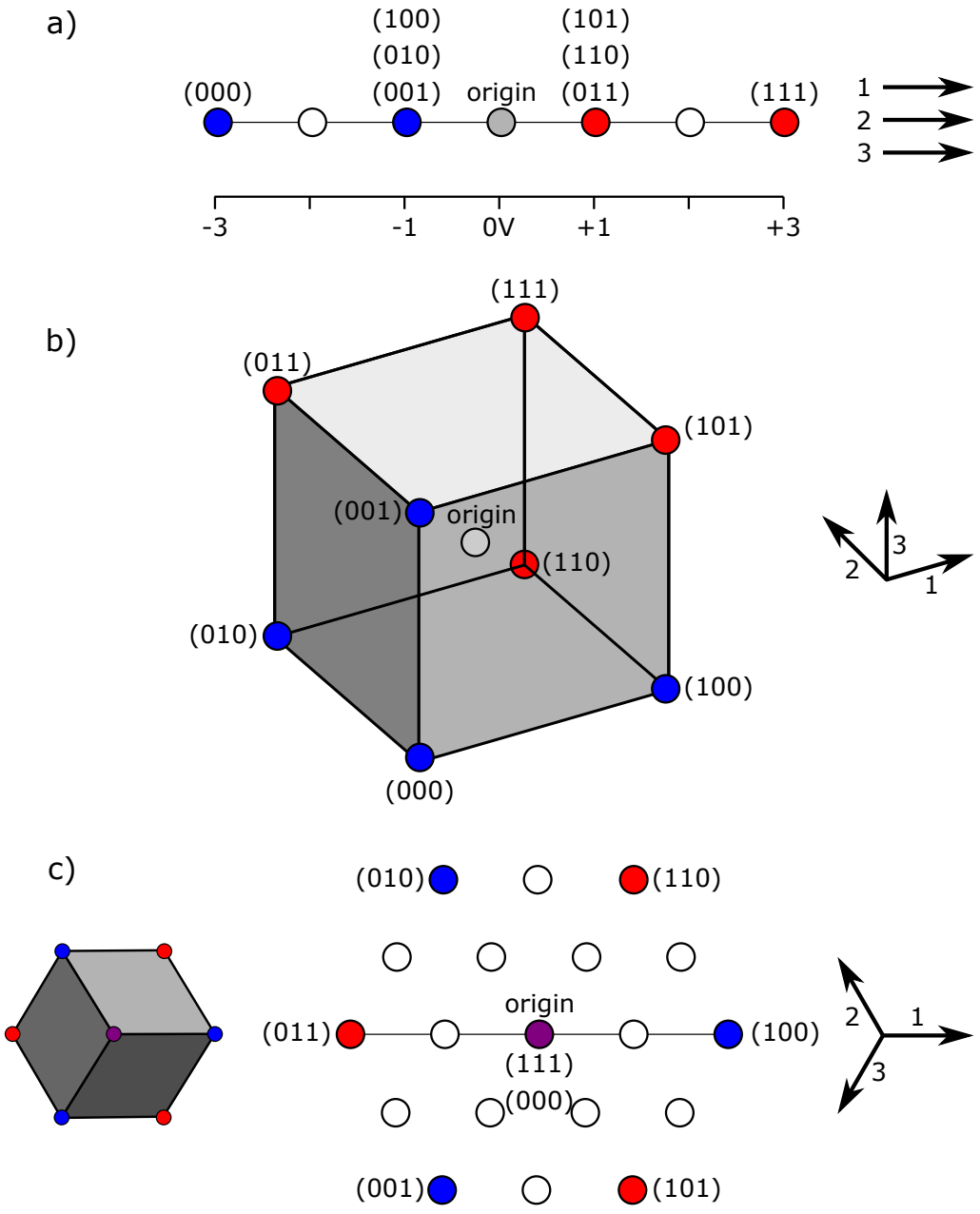


Figure 5.27: Constellation plots (in the complex ζ plane) for three interfering waves. The encoding axis for each channel is indicated by the three black arrows. a) The case when all channels are in phase, as with the initial definition of the majority gate. The outputs lie on the 'x-axis', and have the voltages $\pm 1\,\mathrm{V}$ and $\pm 3\,\mathrm{V}$. b) A conceptual 'state-cube' for the eight possible binary states if orthogonal bases were used. c) The isometric projection of the state-cube, where $\psi = \pm 120°$ between each of the three channels. The constellation plot shows the location of each of the 8 states, including the degeneracy at the origin. The 6 outer states all have the same amplitude, meaning this arrangement could be used to gate a transistor and perform as an 'equality' gate. The cube to the left shows how the state-cube must be tumbled to achieve this projection. The shades of the panels are consistent with Figure 5.27b to assist the reader.

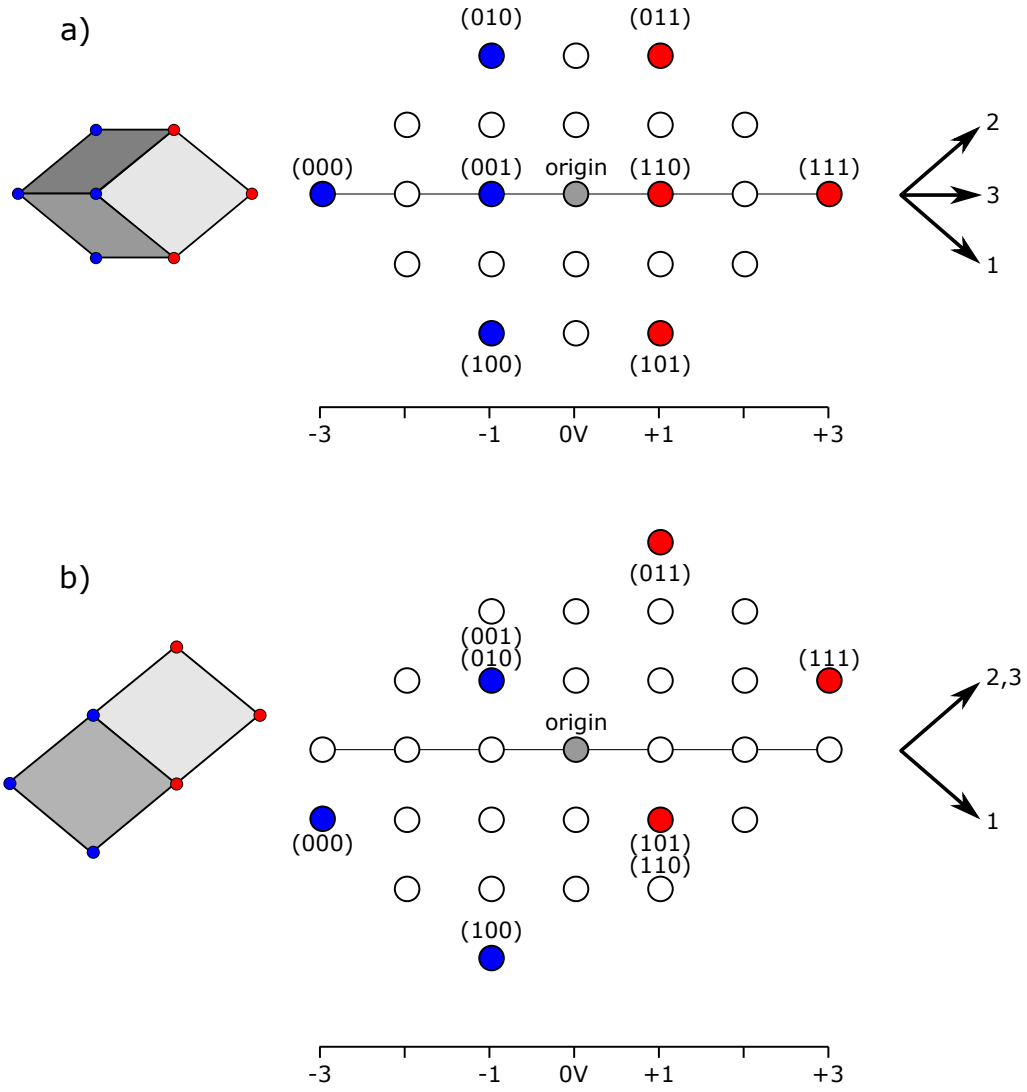


Figure 5.28: Further constellation plots for three interfering waves. a) An alternative rotation of the state-cube results in a constellation which has similar characteristics to the original linear plot in Figure 5.27a, in that a heterodyne measurement along $\theta = 0$ will provide outputs of $\pm 1\,\mathrm{V}$ and $\pm 3\,\mathrm{V}$ with the $\pm$ matching the sign of the majority. This formation may have additional functionality as none of the states are degenerate (and thus can be individually identified). b) a final alternative orientation of the state-cube. This shows a case where two sets of states with matching majority-types have been made degenerate. This is the maximum number possible without resorting to the linear mapping.

enhanced. As three bits are now being used, the 8 possible states are conceptually mapped onto the vertices of a (3D) cube (Figure 5.27b). It is noted here that each of the vertices are equidistant from the middle of the cube (the origin), which would be equivalent to all of the states having the same amplitude. Unfortunately, phase has no 3D analogue that can be used, so the vertices of the cube must be projected onto the 2D plane.

The most obvious projection is to begin isometrically, where the three axes (now correlating to the ψ for each of the three channels, where ψ is the phase between each input signal and the reference when the signals are encoded) are separated by 120°. This produces the constellation plot shown in Figure 5.27c. This is an interesting plot, as the 8 possible states are distributed on 7 points, with the central point being occupied by both 000 and 111. This may actually be a useful implementation, as this signal could be used to drive an AM-input transistor to perform an 'equality' function.

This does not help with finding the majority as it is not possible to separate the two types of states (majority-1 and majority-0) by a straight line. If the imaginary cube is now tumbled and stretched, are there any other arrangements of the three axes where it is possible to separate the two majority types? Some of the alternative possibilities are presented in Figure 5.28. It is observed here that these constellations only allow for the measurement of the majority as they are moving back towards the initial linear arrangement of the axes, which means that they are not helpful for solving the original problem.

If the symmetry of the state-cube is considered, it becomes obvious that there is no angle from which it can be viewed (and therefore projected) that allows for the two different majority states to be separable, while also having a single consistent amplitude. This may have been obvious from the statement that there are only two orthogonal directions on a 2D plane, but the geometric concept was presented anyway, as it enabled the discovery of the potentially useful 'equality' gate.

5.4.4 Phase-shift keying conclusions

To summarise the key points of this section: quadrature phase-shift keying can be used using the superposition method of state creation to double the amount of data that can be transmitted in a magnonic signal. Higher order phase-shift keying may be possible and useful for data transmission, but as it cannot be implemented with the superposition method, its uses within magnon computing may be limited. A link between 8-PSK and the majority gate was observed, and it was demonstrated that there is no way of modifying the phases or amplitudes of the majority gate inputs such that the output is a consistent amplitude, which means that a different 'clipper' style solution will likely be required to solve the majority gate problem. It was, however, shown that by using different phases for the three majority gate inputs, it is possible to create an 'equality' gate, which may have practical applications.

5.5 Conclusions on magnon multiplexing

In this chapter, methods for multiplexing and demultiplexing magnonic signals were investigated. It was found that both interferometry and heterodyning can be used to extract data from a multiplexed signal to varying degrees of success.

Interferometry can be used to decode amplitude modulated signals, however, due to the limitations of the construction of the interferometer (namely loss within the splitter elements), this method is not very efficient. It was also found that the channel frequency spacing for the interferometer could not be less than 50 MHz without losing the ability to distinguish between adjacent channels. These factors combined lead to the conclusion that interferometry is not a practical demultiplexing method.

Heterodyning can be used to decode amplitude or phase modulated signals. This method appears to be much more versatile than the interferometry method, which is why it was the primary detection method used in Chapter 4. It was found that the acceptable channel frequency spacing for heterodyne demodulated signals was

related to the time constant of the low-pass filter used in the demodulator, which was in turn related to the duration of any given bit pulse. Using longer pulses allows for lower frequency filters to be used, which would in turn enable more signals to be multiplexed simultaneously.

An additional method of improving the amount of data transmitted in a magnonic signal was also investigated: quadrature phase-shift keying. It was found that two data channels can be encoded into a single frequency channel, transmitted down the magnon waveguide, and then separated, by PM encoding the two signals 90° out of phase. It was noted that this method also gives rise to the possibility of interesting two-bit logical operations. By extending the ideas looked at here, the prospect of higher order phase-shift keying was considered. Although it appears that it is unlikely that higher order phase-shift keying will be of much use for increasing the amount of data that can be processed simultaneously in a magnon computer, the link between octal phase-shift keying and the majority gate problem was realised.

Solutions to the majority gate output problem were considered, and it was determined that the problem is not solvable by mere interference alone. It was, however, noted that by varying the phases of the three majority gate input signals by multiples of 120°, it was possible to create new unusual logic gates, such as the 'equality' gate.

Chapter 6

Conclusions and Outlook

The key results of this thesis are summarized within this chapter, and some suggestions are made of possible follow-up experiments that may be interesting to pursue. The relevance of the work is also discussed in the context of the future directions of magnonics and spintronics in general.

6.1 Overhauser Spin Battery

In Chapters 2 and 3 it was shown how microwave spin pumping in metallic systems can be understood in terms of spin potentials. By viewing the system through the lens of magnetic resonance phenomena, it was possible to identify the spin accumulation generated during the Overhauser Effect as a potential source of spin-motive force. It was shown that by shorting out the spin accumulation with an adjacent rapidly relaxing material, it was possible to create spin gradients, which in turn lead to the generation of pure spin currents, which were detectable with the inverse spin Hall effect.

Ferromagnetic/paramagnetic bilayers were experimentally shown to produce the Overhauser Spin Battery effect, which supports the theory presented in Chapter 2. The well-known two spin channel model was augmented to include precessing ferromagnets, and was then used to explain the apparent lack of signal in the paramagnet/paramagnet experiments. Any voltage generated by the paramag-

net/paramagnet bilayer was too small to be detected utilizing the apparatus used. It would be interesting to repeat the experiment at mK temperatures, as the Zeeman split energy levels are less likely to be pre-saturated by thermal excitations in this temperature regime. Detection of an ISHE signal in this scenario would be strong evidence in support of the Overhauser Spin Battery model.

Another investigation that could follow up the experiments presented here would be to look at the relaxation times of various metals, and determining whether this is indeed the key underlying parameter which controls the Spin Battery efficiency. This could be done either experimentally, or via a more thorough review of already published literature.

If these subsequent investigations help to verify the theory presented in this thesis, it would suggest that the Overhauser Spin Battery is a viable method for generating pure spin currents, without the need for permanent ferromagnetic elements. The absence of these permanent ferromagnetic elements would be beneficial when attempting to miniaturize Spin Battery based devices, as ferromagnetic elements can sometimes be challenging to produce. Their absence would make any such devices easier to manufacture, and also make them less volatile to the influence of external magnetic fields.

One drawback of the Overhauser Spin Battery is that it still requires microwaves to produce the spin accumulation that drives the spin current. Microwave generation can require large amounts of power, and since it is likely that only a small fraction of that power will be used by the device, this is potentially a significant source of losses. Given that one of the primary motivations for investigating spin-based devices is the desire to reduce power consumption, this is a key problem that would need addressing before efficient devices that utilize the Overhauser Spin Battery effect can be developed.

Although the practical deployment of the Overhauser Spin Battery is still a long way off, the theory and supporting evidence presented in this thesis provide a novel approach to the problem of pure spin current generation, and may still be the genesis

of a new class of purely paramagnetic spintronic devices.

6.2 Magnon Computing

6.2.1 AM/PM Converters

In Chapter 4, a new device was described that was able to convert between AM and PM encoded magnon signals — the AM/PM converter — and was experimentally verified. This device allows magnon computing elements that have already been created but have different encoding paradigms to be integrated with each other. An important example of this is the AM driven all-magnon transistor, which also forms the basis of the AM magnon amplifier. The AM magnon amplifier was modified to produce a PM output, and it was noted that this PM amplifier could also operate as an AM rectifier.

As a new tool available to the Magnon Computing community, the AM/PM converter has a lot of potential for follow on work. As demonstrated in §5.4.3, by viewing current Magnon Computing problems with the new AM/PM converter and the ζ notation in mind, new devices such as the 'equality' gate can be found. Exploring the potential applications of the AM/PM converter is expected to be fruitful. Although the AM/PM converter is a simple device, there are, however, a few details that must be considered before it can be fully utilized in magnonic circuits.

Each AM/PM converter requires the joining of two magnon waveguides, one of which must contain an unmodulated signal of a known amplitude and phase. This unmodulated signal could be provided in two ways — it can either be generated near the junction of the converter for each converter in the circuit, or it can be generated at one location on the circuit board and carried to where it needs to be by a waveguide. Both of these methods have their own problems. Using a single magnon source requires careful transportation of the pure-tone signal across the circuit board in multiple branching waveguides. This approach would require

significant portions of the circuit board to be set aside purely for this purpose, and therefore might hamper miniaturization efforts. Alternatively, generating a new signal for each converter would require the presence of a magnon source whenever a signal is converted from AM to PM or back. Depending on the method by which this was achieved, this could be costly in terms of power consumption, however, if an efficient magnon generation technique was used, it is likely that generating a new signal for each converter would be the best approach.

When magnon streams meet at a confluence of waveguides, the combined pulses may not propagate as expected [61]. It would be worth simulating the precise design of the AM/PM converter (specifically the angle at which the two channels join) to determine how much back-flow occurs into each input channel, as well as to determine the relative amplitude of the unmodulated signal input with respect to the modulated data stream that is required for the converter to operate as intended.

Despite the potential limitations on the efficiency of a device containing AM/PM converters, the increase in flexibility of the types of components that can be used in a magnonic circuit makes AM/PM converters a useful new circuit element. If the converters happen to be the least efficient element of a circuit, it may be necessary to design circuits that attempt to keep their number to a minimum by having separate AM and PM sections of the chip. Even if this is the case, AM/PM converters are a significant new component that helps to resolve the issue of how to link the output of one magnonic device with the input of the next, and will therefore play an important role in the development large magnonic circuits in the future.

6.2.2 Multiplexing

In Chapter 5, the prospect of magnon multiplexing was explored. It was discovered that using interferometry to separate the magnon streams was ineffective. It was also established that it is possible to multiplex both AM and PM signals and decode them again using the heterodyne technique. It was noted that there is a strong relationship between the duration of any given data pulse, the cut-off frequency of

the low-pass filter used after the heterodyner, and the channel frequency separation that can be used. It was estimated that the upper limit of the data transmission rate would be around $230\,\mathrm{Mbs}^{-1}$. It was also noted that, although using more channels necessitates a lower bit rate, these channels can potentially be processed simultaneously using a smaller number of components. Pursuing this multichannel processing would be an interesting next step for this experiment.

Chapter 5 also briefly discussed some existing signal processing techniques (§5.3.2) such as superheterodyning, which was not used in the experiments due to the apparent lack of an easy way of extracting the phase information from the signal. Given the above conclusion that using DC as the intermediate frequency followed by a low-pass filter severely restricts the bit rate of the system, it is worth reconsidering the use of superheterodyning.

If the PM encoded GHz magnonic signals were superheterodyne downconverted to 1 MHz, and then filtered by a very narrow band-pass filter, it should be possible to extract a single frequency channel, oscillating at 1 MHz. This signal still contains the original phase information, however it is not currently accessible. If this signal is now heterodyned with a 1 MHz reference signal, this should result in a DC signal in which the original phase information can be measured as before. Effectively, this process has shifted the filtering process from slow-response, wide, low-pass filters, to fast-response, narrow, band-pass filters. This should allow for the use of stronger filters and thus enable more channels to be transmitted closer together simultaneously. Investigating whether this is possible would be an obvious next step for this experiment, as it may lead to a higher limit of the data transmission rate.

Although this now appears to be in the realm of 'engineering problems' (the solutions to which have already been thoroughly investigated for radio signal processing [57]), finding a way to successfully (and quickly) demultiplex signals that are only on the order of 10's-100's of kHz apart may allow for a more thorough investigation into the non-linear crosstalk between magnon channels that was so suspiciously absent from the measurements made in this thesis.

Quadrature phase-shift keying was also explored as an idea to increase the data transmitted down a waveguide and was successfully shown to work using heterodyne demodulation. QPSK works as the two channels are encoded into orthogonal phases, which are independently accessible by the heterodyne demodulator. The prospect of adding more channels to a single frequency was investigated by studying octal phase-shift keying, as well as three-wave interference. A link was observed between three-channel interference and the majority gate, which led to the discovery that there are no arrangements of the relative phases of the three input channels which produces an output in which the 0 and 1 majority states are distinguishable, and all have a constant amplitude. This is important, as it means that to solve the problem of AM/PM mixing in the output of the majority gate, some sort of selective attenuation device is likely to be needed.

The fact that it is possible to use the heterodyne demodulator to extract not only the binary information from either channel in the QPSK signal, but also the output of certain logical operations on the two channels without losing any of the original information is an interesting observation. The potential of this feature should be explored, as it could function as an additional element in a new logical processing system.

In this thesis, it was shown that both signal multiplexing and QPSK can be applied to magnonic systems. These techniques themselves are not new (having been previously used in radio systems), and as such, it would be of interest to investigate if and how the response of magnonic systems differs from the already well characterised radio behaviour. If it is assumed that by applying more advanced techniques it will become possible to successfully multiplex up to a few thousand channels (which could then be simultaneously processed), then this is an important avenue of research to explore, as this could save a large amount of space on any future magnonic microchips and greatly assist in miniaturization efforts.

The investigations into QPSK (and subsequently the majority gate), demonstrated the power of moving from the concepts of binary, scalar computing, to the

more flexible, complex-vector based (ζ) paradigm. Although this thesis primarily used 180° phase shifts to encode digital PM data, it is suggested that it would be worthwhile to explore more fully the methods by which data is encoded into magnons (including the consideration of analogue data), as the ability to integrate digital and analogue processing is one of the promising aspects of magnonic computing that should be developed in the future.

6.2.3 General outlook

In §1.3, Magnon Computing was introduced as a new paradigm which promises faster, smaller, and more efficient computers than those that exist today. Although fulfilling this promise is not in the immediate future, it is still worth considering how the new devices proposed in this thesis fit into this 'bigger picture' of magnon computing.

The key length scale for magnon computers is the wavelength of the magnons being used. This is important as it governs the size of certain components of a magnonic circuit, such as the microwave antennae used for excitation or detection, or magnonic crystal elements. Given that magnonic crystals may have sizes on the order of 10 times that of the magnon wavelength, it is desirable to reduce the magnon wavelength to the smallest size possible to maximise the number of components that can fit on a chip. Due to the magnon dispersion relation, after a certain point, decreasing the wavelength will start to significantly increase the magnon frequency, eventually into the THz regime. Exciting these magnons can be challenging as it becomes increasingly difficult to produce antennae with widths that match the wavelength of the magnons.

In 2016, Yu *et al.*[62] demonstrated that by introducing nano-magnets underneath a microwave antenna, it is possible to produce and detect magnons with wavelengths of 88 nm. This is an example of how a chip-based technology can be used to generate short wavelength magnons which could be used in magnonic circuits. Further development of this technique (or others) is still required before nm

scale magnonics can be readily accessed.

Magnons with nm wavelengths are dominated by the exchange interaction [62]. They have much larger group velocities, and are therefore able to transport information at a faster rate. The atomic scale is the true limit of the magnon wavelength, however these magnons will be much more energetic, and may be challenging to efficiently excite. Gaining access to nm scale magnons will be beneficial not just for miniaturization as discussed above, but also for the increase is potential clock speeds.

Clock speeds describe the frequency at which any given transistor on a microchip is able change its state. A transistor on a 3 GHz processor can change its state 3 billion times per second. This could also be viewed as a measure of the 'duration' of a bit — how long the system needs to remain at a certain voltage before its value is acknowledged and processed. As magnonics is a wave-based technology where information is encoded in either phase or amplitude, the maximum potential clock speed could be estimated to be on the order of the frequency of the magnon. This is justifiable as having bits that are at least 1-3 full waveforms long would allow a frequency, amplitude, and phase to be determined, and should be long enough to allow for the bit to be registered. If nm scale magnons with frequencies in the low THz are accessible, then the potential clock speeds obtainable are also in the THz regime, which is around 1000 times faster than current silicon-based computer processors.

The magnonic aspects of both AM/PM conversion and multiplexing are straightforward — they both rely on the superposition of spin-waves. This phenomenon should not be affected by the size of the waveguides, or the frequency of the magnons, and as such should be immediately scalable down to the nm scale or up to the THz regime. The limiting factor of these devices is instead how the magnons are produced and detected, and how the data is handled by the driving electronics. Once more advanced interface techniques are developed, the new devices discussed in this thesis should be ready for use in magnonic circuits without further modification.

A lot of work is required before Magnon Computing can become a mainstream technology, though the ideas and results presented here constitute another small step in the right direction. A greater understanding of how pure spin currents are generated in metallic systems will be useful for the development of integrated Spintronic devices, while the ability to convert between amplitude and phase modulated magnon signals will be a boon for the development of Magnonic circuitry, and another useful tool in the magnonician's toolbox.

Bibliography

1. Waldrop, M. M. More Than Moore. *Nature* **530,** 144–147 (2016).

2. Zhirnov, V. V., Cavin, R. K., Hutchby, J. A. & Bourianoff, G. I. *Limits to binary logic switch scaling - A gedanken model* in *Proceedings of the IEEE* **91** (2003), 1934–1939.

3. Johnson, M. & Silsbee, R. H. Interfacial charge-spin coupling: Injection and detection of spin magnetization in metals. *Physical Review Letters* **55,** 1790–1793 (1985).

4. Baibich, M. N. *et al.* Giant magnetoresistance of (001)Fe/(001)Cr magnetic superlattices. *Physical Review Letters* **61,** 2472–2475 (1988).

5. Binasch, G., Grünberg, P., Saurenbach, F. & Zinn, W. Enhanced magnetoresistance in layered magnetic structures with antiferromagnetic interlayer exchange. *Physical Review B* **39,** 4828–4830 (1989).

6. Gregg, J. F. Spintronics: A growing science. *Nature Materials* **6,** 798–799 (2007).

7. Kittel, C. *Introduction to Solid State Physics* (Wiley, 2004).

8. Reznik, D. *et al.* Direct observation of optical magnons in $YBa_2Cu_3O_{6.2}$. *Phys. Rev. B* **53,** R14741–R14744 (June 1996).

9. Gurevich, A. G. *Magnetization Oscillations and Waves* **1,** 74–75 (1987).

10. Ashcroft, N. W. & Mermin, N. D. *Solid state physics* (Saunders College, 1976).

11. Simon, S. H. *The Oxford Solid State Basics* (OUP Oxford, 2013).

12. Serga, A. A., Chumak, A. V. & Hillebrands, B. YIG magnonics. *Journal of Physics D: Applied Physics* **43** (2010).

13. Chumak, A. V., Serga, A. A. & Hillebrands, B. Magnonic crystals for data processing. *Journal of Physics D: Applied Physics* **50.** arXiv: 1702.06701 (2017).

14. Brataas, A., Kent, A. D. & Ohno, H. Current-induced torques in magnetic materials. *Nature Materials* **11,** 372–381 (2012).

15. Fung, T. C. *Phonon Magnonics* DPhil. Thesis (University of Oxford, 2015).

16. Hirsch, J. E. Spin Hall Effect. *Physical Review Letters* **83,** 1834–1837 (1999).

17. Hahn, C. *et al.* Comparative measurements of inverse spin Hall effects and magnetoresistance in YIG/Pt and YIG/Ta. *Physical Review B - Condensed Matter and Materials Physics* **87.** arXiv: 1302.4416 (2013).

18. Saitoh, E., Ueda, M., Miyajima, H. & Tatara, G. Conversion of spin current into charge current at room temperature: Inverse spin-Hall effect. *Applied Physics Letters* **88,** 182509 (2006).

19. Kalinikos, B. Excitation of propagating spin waves in ferromagnetic films. *IEE Proceedings H Microwaves, Optics and Antennas* **127,** 4–10 (1980).

20. Schneider, T., Serga, A. A., Neumann, T., Hillebrands, B. & Kostylev, M. P. Phase reciprocity of spin-wave excitation by a microstrip antenna. *Physical Review B - Condensed Matter and Materials Physics* **77.** arXiv: 0804.1090 (2008).

21. Brächer, T. *Parallel parametric amplification of spinwaves in micro-structures* PhD thesis (Universität Kaiserslautern, 2015).

22. Tserkovnyak, Y., Brataas, A. & Bauer, G. E. W. Enhanced Gilbert Damping in Thin Ferromagnetic films. *Physical Review Letters* **88,** 117601 (2002).

23. Brataas, A. *et al.* Spin Pumping and Spin Transfer. *Physics,* 1–30 (2011).

24. Bloch, F. Zur Theorie des Ferromagnetismus. *Zeitschrift für Physik* **61,** 206–219 (Mar. 1930).

25. Griffiths, J. H. E. Anomalous High-frequency Resistance of Ferromagnetic Metals. *Nature* **158,** 670–671 (1946).

26. Chumak, A. V., Vasyuchka, V. I., Serga, A. A. & Hillebrands, B. Magnon spintronics. *Nature Physics* **11,** 453 (June 2015).

27. Klingler, S. *et al.* Design of a spin-wave majority gate employing mode selection. *Applied Physics Letters* **105,** 152410 (2014).

28. Chumak, A. V. *et al.* All-linear time reversal by a dynamic artificial crystal. *Nature Communications* **1** (2010).

29. Chumak, A. V., Serga, A. A. & Hillebrands, B. Magnon transistor for all-magnon data processing. *Nature Communications* **5** (2014).

30. Slichter, C. P. *Principles of Magnetic Resonance* (Springer Berlin Heidelberg, 1996).

31. Gregg, J. F. *et al.* A Microscopic Explanation of Microwave Spin Pumping. arXiv: `1711.06048` (Nov. 2017).

32. Overhauser, A. W. Polarization of nuclei in metals. *Physical Review* **92,** 411–415 (1953).

33. *The NIST reference on Constants, Units, and Uncertainty* `https://physics.nist.gov/cuu/index.html`.

34. Gasiorowicz, S. *Quantum physics* (Wiley, 2003).

35. Foot, C. J. *Atomic Physics (Oxford Master Series in Atomic, Optical and Laser Physics)* 1st ed. (Oxford University Press, USA, Feb. 2005).

36. Blundell, S. & Blundell, K. *Concepts in Thermal Physics* (OUP Oxford, 2010).

37. Bass, J. & Pratt Jr., W. P. Spin-diffusion lengths in metals and alloys, and spin-flipping at metal/metal interfaces: an experimentalist's critical review. *Journal of Physics: Condensed Matter* **19,** 183201 (2007).

38. Wang, H. L. *et al.* Scaling of Spin Hall Angle in 3d, 4d, and 5d Metals from $Y_3Fe_5O_{12}$ Metal Spin Pumping. *Phys. Rev. Lett.* 197201.

39. Hoffmann, A. Spin hall effects in metals. *IEEE Transactions on Magnetics* **49,** 5172–5193 (2013).

40. Serway, R. & Gordon, J. *Principles of Physics Principles of Physics* **v. 2** (Saunders College Pub., 1998).

41. Lauer, V., Jungfleisch, M. B., Neb, R., Chumak, A. V. & Hillebrands, B. *Improvement of the yttrium iron garnet/platinum interface for spin pumping-based applications* in *International Conference on Oxide Materials for Electronic Engineering - Fabrication, Properties and Applications, OMEE 2014 - Book of Conference Proceedings* (2014), 109–110. arXiv: 1302.6697.

42. Ellett, A. & Zabel, R. M. The pirani gauge for the measurement of small changes of pressure. *Physical Review* **37,** 1102–1111 (1931).

43. Penning, F. M. Ein neues manometer für niedrige gasdrucke, insbesondere zwischen l0-3 und 10-5 mm. *Physica* **4,** 71–75 (1937).

44. Behrisch, R. & Eckstein, W. *Sputtering by Particle Bombardment: Experiments and Computer Calculations from Threshold to MeV Energies* (Springer Berlin Heidelberg, 2007).

45. Sauerbrey, G. Verwendung von Schwingquarzen zur Wägung dünner Schichten und zur Mikrowägung. *Zeitschrift für Physik* **155,** 206–222 (1959).

46. Haynes, W. M. *CRC Handbook of Chemistry and Physics, 97th Edition* (CRC Press, 2016).

47. Shone, M. The technology of YIG film growth. *Circuits, Systems and Signal Processing* **4,** 89–103 (1985).

48. Castel, V., Vlietstra, N., Van Wees, B. J. & Youssef, J. B. Frequency and power dependence of spin-current emission by spin pumping in a thin-film YIG/Pt system. *Physical Review B - Condensed Matter and Materials Physics* **86.** arXiv: arXiv:1206.6671v2 (2012).

49. Cho, A. Y. & Arthur, J. R. Molecular beam epitaxy. *Progress in Solid State Chemistry* **10,** 157–191 (1975).

50. Winter, J. *Magnetic resonance in metals* (Clarendon Press, 1971).

51. Ando, K. *et al. Inverse spin-Hall effect induced by spin pumping in metallic system* in *Journal of Applied Physics* **109** (2011).

52. Seebeck, T. in *Abhandlungen der Königlichen Akademie der Wissenschaften zu Berlin* 265–373 (1825).

53. Hubbard, J. Exchange splitting in ferromagnetic nickel. *Proceedings of the Physical Society* **84,** 455–464 (1964).

54. Brächer, T. *et al.* Phase-to-intensity conversion of magnonic spin currents and application to the design of a majority gate. *Scientific Reports* **6** (2016).

55. Bates, R. J. & Bates, M. *Principles of Voice and Data Communications* (McGraw-Hill Irwin, 2007).

56. Horowitz, P. & Winfield, H. The Art of Electronics. *American Journal of Physics,* 1131 (1990).

57. Lathi, B. & Ding, Z. *Modern Digital and Analog Communication Systems* (Oxford University Press, 2010).

58. Haykin, S. *Communication systems* (Wiley, 2001).

59. Laplante, P. A. *Comprehensive Dictionary of Electrical Engineering* (CRC Press, 1998).

60. Rhodes, S., Fang, R. & Chang, P. Coded Octal phase shift keying in TDMA satellite communications. *COMSAT Technical Review* **13,** 221–258 (1983).

61. Klingler, S. *et al.* Spin-wave logic devices based on isotropic forward volume magnetostatic waves. *Applied Physics Letters* **106.** arXiv: `arXiv:1503.04101v1` (2015).

62. Yu, H. *et al.* Approaching soft X-ray wavelengths in nanomagnet-based microwave technology. *Nature Communications* **7.** arXiv: `arXiv:1011.1669v3` (2016).